arXiv:2012.00578v2 [hep-ex] 26 Aug 2021

EUROPEAN ORGANISATION FOR NUCLEAR RESEARCH (CERN)

Eur. Phys. J. C 81 (2021) 578
DOI: DOI:10.1140/epjc/s10052-021-09233-2

CERN-EP-2020-199
26th November 2021

Muon reconstruction and identification efficiency in ATLAS using the full Run 2 pp collision data set at $\sqrt{s}$ = 13 TeV

The ATLAS Collaboration

This article documents the muon reconstruction and identification efficiency obtained by the ATLAS experiment for 139 fb^{-1} of pp collision data at $\sqrt{s}$ = 13 TeV collected between 2015 and 2018 during Run 2 of the LHC. The increased instantaneous luminosity delivered by the LHC over this period required a reoptimisation of the criteria for the identification of prompt muons. Improved and newly developed algorithms were deployed to preserve high muon identification efficiency with a low misidentification rate and good momentum resolution. The availability of large samples of $Z \to \mu\mu$ and $J/\psi \to \mu\mu$ decays, and the minimisation of systematic uncertainties, allows the efficiencies of criteria for muon identification, primary vertex association, and isolation to be measured with an accuracy at the per-mille level in the bulk of the phase space, and up to the percent level in complex kinematic configurations. Excellent performance is achieved over a range of transverse momenta from 3 GeV to several hundred GeV, and across the full muon detector acceptance of $|\eta| < 2.7$.

© 2021 CERN for the benefit of the ATLAS Collaboration.
Reproduction of this article or parts of it is allowed as specified in the CC-BY-4.0 license.

1 Introduction

In the years from 2015 to 2018, Run 2 of the Large Hadron Collider (LHC) at CERN provided an unprecedented number of pp collision events at a centre-of-mass energy of 13 TeV. The identification and accurate measurement of processes with muons in the final state is one of the main features of the ATLAS experiment [1] at the LHC, and a key element for a successful physics programme. For example, Standard Model (SM) predictions can be tested by studying the leptonic decays of the W or Z/γ^* vector bosons, heavy-flavour hadrons undergoing weak decays into leptons can be identified with high signal-to-background ratio, and beyond-the-SM (BSM) resonances may be found in leptonic decay channels. Highlight analyses where optimal muon identification performance has been fundamental are, for example, the measurement of Higgs boson properties [2], the precise determination of SM parameters in the quark-mixing sector [3], and searches for BSM physics in extreme regions of phase space [4, 5]. Analyses targeting these and similar processes profit from the structure of the ATLAS muon reconstruction and identification systems [6], which combine information from several subdetectors to reach almost 100% reconstruction and identification efficiency over a wide range of transverse momenta (p_{T}), with background contamination at the per-mille level and good momentum resolution, even in challenging data-taking conditions characterised by a large number of interactions per LHC bunch crossing.

Compared to a previous publication [7], which reported on the muon identification performance on early $\sqrt{s}$ = 13 TeV data, this article describes refined and newly developed techniques that improved muon identification performance over a wide region in phase space, and reduced the uncertainties related to the data-driven efficiency measurements by roughly a factor of five. Specific care is dedicated to the improvement of muon identification algorithms and of the efficiency measurement in extreme regions of the phase space, such as p_{T} of a few GeV or a few TeV, the forward region of the detector where instrumentation coverage is poorer, or an environment polluted by a large number of pp interactions. Muon reconstruction and identification efficiencies in the bulk of the phase space are measured using the tag-and-probe method, applied to $Z \to \mu\mu$ data collected during the full Run 2. The available data set is about 40 times larger than that used in the previous publication, and revised algorithms for the efficiency extraction and for the modelling of background contamination are adopted. A similar approach is used for the measurements of vertex association and isolation selection efficiencies, while the measurements of muon reconstruction and identification efficiency at low p_{T} or in forward regions of the detector rely on the tag-and-probe method applied to a $J/\psi \to \mu\mu$ data set, and on a double-ratio method applied to the $Z \to \mu\mu$ data set, respectively.

This article is structured as follows. Section 2 briefly describes the experimental apparatus, Section 3 provides details of the analysed data set and simulated samples, Section 4 summarises the muon candidate reconstruction process, and Section 5 describes the algorithms developed for optimal muon identification. Section 6 and Section 7 are the core of the article: the former describes the measurements of muon identification, vertex association and isolation selection efficiencies using several data-driven techniques, while the latter details the results obtained. Conclusions are given in Section 8.

2 ATLAS detector

The ATLAS detector [1] at the LHC covers nearly the entire solid angle around the collision point.[1] ATLAS consists of an inner tracking detector surrounded by a thin superconducting solenoid, electromagnetic and hadronic calorimeters, and a muon spectrometer incorporating three large superconducting toroidal magnets.

The inner-detector system (ID) is immersed in a 2 T axial magnetic field which bends charged particles in the r–ϕ plane and provides tracking capabilities in the range $|\eta| < 2.5$. The high-granularity silicon pixel detector covers the vertex region and typically provides four position measurements (hits) per track, the first hit normally being in the insertable B-layer installed before Run 2 [8, 9]. It is followed by the silicon microstrip tracker (SCT), which usually provides eight measurements per track. These silicon detectors are complemented by the transition radiation tracker (TRT), which enables radially extended track reconstruction up to $|\eta| = 2.0$.

The calorimeter system covers the pseudorapidity range $|\eta| < 4.9$. Within the region $|\eta| < 3.2$, electromagnetic calorimetry is provided by barrel and endcap high-granularity lead/liquid-argon (LAr) calorimeters, with an additional thin LAr presampler covering $|\eta| < 1.8$ to correct for energy loss in material in front of the calorimeters. Hadronic calorimetry is provided by the steel/scintillator-tile calorimeter, segmented into three barrel structures within $|\eta| < 1.7$, and two copper/LAr hadronic endcap calorimeters. The solid angle coverage is completed with forward copper/LAr and tungsten/LAr calorimeter modules optimised for electromagnetic and hadronic measurements, respectively.

The muon spectrometer [6] (MS) comprises separate trigger and high-precision tracking chambers measuring the deflection of muons in the r–z plane due to a magnetic field generated by the superconducting air-core toroids. The field integral of the toroids ranges between 2.0 and 6.0 T m across most of the detector. A set of precision chambers covers the region $|\eta| < 2.7$ with three stations of monitored drift tube (MDT) chambers. The innermost MDT station is replaced with cathode-strip chambers (CSCs) in the $|\eta| > 2.0$ region, where the background is higher. Each MDT chamber provides six to eight η measurements along the muon track, while the CSCs provide four simultaneous measurements of η and ϕ. The nominal single-hit resolution of the MDTs and CSCs is about 80 µm and 60 µm, respectively, in the bending plane. The chambers are precisely aligned with a system based on optical sensors [6] designed to obtain a 10% transverse momentum resolution for 1 TeV muons. The muon trigger system covers the range $|\eta| < 2.4$ with resistive-plate chambers (RPCs, three doublet stations for $|\eta| < 1.05$) in the barrel, and thin-gap chambers (TGCs, one triplet station followed by two doublets for $1.0 < |\eta| < 2.4$) in the endcap regions. The RPCs and TGCs also provide tracking information complementary to the precision chambers, in particular improving the determination of the track coordinate in the non-bending direction, referred to as the second coordinate. The typical spatial resolution for the position measurements in the RPCs and TGCs is 5–10 mm in both the bending plane and in the non-bending direction.

Interesting events are selected by the first-level trigger system implemented in custom hardware, followed by selections made by algorithms implemented in software in the high-level trigger [10]. The first-level

[1] ATLAS uses a right-handed coordinate system with its origin at the nominal interaction point (IP) in the centre of the detector and the z-axis along the beam pipe. The x-axis points from the IP to the centre of the LHC ring, and the y-axis points upwards. Cylindrical coordinates (r, ϕ) are used in the transverse plane, ϕ being the azimuthal angle around the z-axis. The pseudorapidity is defined in terms of the polar angle θ as $\eta = -\ln\tan(\theta/2)$. Angular distance is measured in units of $\Delta R = \sqrt{(\Delta\eta)^2 + (\Delta\phi)^2}$.

trigger accepts events from the 40 MHz bunch crossings at a rate below 100 kHz, which the high-level trigger reduces in order to record events to disk at about 1 kHz.

3 Data and Monte Carlo samples

3.1 Data set description

The results presented in this article are obtained from an analysis of pp collision events collected by the ATLAS detector in the years from 2015 to 2018, with proton bunches colliding every 25 ns at a centre-of-mass energy of $\sqrt{s} = 13$ TeV. The data set corresponds to an integrated luminosity of 139 fb^{-1}, with an average number of pp collisions per bunch crossing of $\langle\mu\rangle = 34$, and maximum instantaneous luminosity of 2.1×10^{34} cm^{-2} s^{-1}. The average number of interactions per bunch crossing varied during the data-taking, with values of $\langle\mu\rangle = 13$, $\langle\mu\rangle = 25$, $\langle\mu\rangle = 38$, $\langle\mu\rangle = 36$ during 2015, 2016, 2017, and 2018, respectively.

Events are accepted for the analysis only if both the solenoid and toroid magnets were on during data taking and if the ID, MS, and calorimeter detectors were in good operating condition[2] [11]. The criteria used to define the good operating condition of the RPC subsystem were reoptimised for data taking in 2017 and 2018, allowing the use of about 1% more integrated luminosity with no visible impact on muon reconstruction performance.

Events were selected online using dedicated muon trigger algorithms [12] that identified signatures consistent with the prompt decays of Z and J/ψ resonances into two muons, with the $J/\psi \to \mu\mu$ sample used to measure the low-p_{T} muon reconstruction and identification efficiency.

The online selection of $Z \to \mu\mu$ candidates was based on single-muon trigger algorithms, to avoid any bias in the reconstruction and identification of the other muon from the decay. The trigger algorithms imposed requirements on the muon candidate's minimum p_{T} and isolation with respect to nearby tracks in the ID. These requirements varied according to the LHC running conditions: in 2015 the muon p_{T} threshold was 20 GeV, and a loose isolation selection was applied; starting from 2016 the muon p_{T} threshold was increased to 26 GeV, and a more restrictive isolation requirement was imposed.

The $J/\psi \to \mu\mu$ candidates events were selected online using several triggers, all based on the identification of one muon candidate plus one MS track or one ID track. The use of MS tracking information was needed for an unbiased measurement of the ID track reconstruction efficiency. Similarly, the use of ID tracking information was needed for unbiased measurements of the remaining components of the muon offline reconstruction and identification efficiency. The muon-plus-track pair was required to form an invariant mass in the range 2.5–4.3 GeV. The muon candidate was required to have a minimum p_{T} of 4 GeV, or 6 GeV, depending on the data-taking year and on the specific trigger. For one type of trigger the track was reconstructed using only the MS information and had to satisfy the requirement of $p_{\mathrm{T}} > 4$ GeV (as measured by the MS). For two other types of triggers, active during different data-taking years, the track was reconstructed using only ID information: loose track requirements and a p_{T} threshold of 3.5 GeV were imposed during 2015 and 2016; whereas during 2017 and 2018 a newly deployed trigger algorithm based on partial event building (PEB) in a region of interest [12] allowed a lower p_{T} threshold of 3 GeV. A large number of events satisfied the requirement for the online $J/\psi \to \mu\mu$ selection, and therefore only a

[2] Overall, 95.6% of the recorded proton–proton collision data collected at $\sqrt{s} = 13$ TeV is certified for physics analysis.

fraction of them were saved to disk. This fraction varied depending on the instantaneous luminosity, on the data-taking year, and on the trigger type, with the triggers based on the PEB technique allowing a larger fraction of events to be collected than in the previous years.

3.2 Simulated event samples description

The results presented in this article rely primarily on a comparison of selected $Z \to \mu\mu$ and prompt $J/\psi \to \mu\mu$ decays in data, referred to as signal, with the corresponding Monte Carlo (MC) simulated events.

The $Z \to \mu\mu$ signal process was simulated using the Powheg-Box v2 [13] generator at next-to-leading order (NLO) in QCD with the CT10 parton distribution function (PDF) set [14] for the hard-scatter process. Events were generated with a dimuon invariant mass above 40 GeV. The parton showering was simulated using Pythia 8.186 [15] with the CTEQ6L1 PDF set [16] and the AZNLO [17] set of tuned parameters (tune) for the underlying event. About 210 million events were simulated for this process. A set of signal samples of $Z^*/\gamma^* \to \mu\mu$ events with dimuon invariant mass generated above 120 GeV and the same settings as described above was also used. For comparisons to assess systematic uncertainties, additional $Z \to \mu\mu$ events were generated using the Sherpa v2.2.1 generator with a set-up described in detail in Ref. [18].

The $J/\psi \to \mu\mu$ signal process was simulated using the Pythia 8.186 [15] leading-order generator, with the CTEQ6L1 PDF set and A14 [19] as the underlying-event tune. In addition, Photos++ v3.52 [20, 21] was used to simulate the effect of final-state radiation. To increase the effective number of events in the regions of phase space relevant to this analysis, the events were generated in a reduced phase space, requiring at least one of the two muons to have $p_{\mathrm{T}} > 6$ GeV and both muons to have $|\eta| < 2.5$. About 420 million events were simulated using this configuration.

Other MC simulated processes were used to study additional contributions from prompt muons, non-prompt muons, or hadrons misidentified as muon candidates. The diboson, $Z \to \tau\tau$, and $W \to \mu\nu$ processes were simulated using the same generator and parton showering algorithm as the $Z \to \mu\mu$ signal sample. The contribution from $t\bar{t}$ production was simulated at NLO using the Powheg-Box v2 generator [13], with the NNPDF3.0 NLO PDF set [22] and parton showering performed using Pythia 8.186 with the NNPDF2.3 LO PDF set [23] and A14 tune. Multi-jet events involving heavy-flavour jets, namely $b\bar{b}$ and $c\bar{c}$ production, were simulated using Pythia 8B [15] with the NNPDF2.3 LO PDF set and A14 as the underlying-event tune.

All the generated events were passed through the simulation of the ATLAS detector based on Geant4 [24, 25] and reconstructed with the same algorithms as used for data.

The simulation of multiple proton–proton interactions in each bunch crossing, i.e. pile-up interactions, was done by adding the detector response simulation of minimum-bias interactions, generated using Pythia 8.186 with the A3 min-bias tune [26], on top of the hard-scattering process in amounts corresponding to the pile-up profile observed during the data-taking.

4 Reconstruction

The main signature exploited for muon identification in ATLAS is that of a minimum-ionising particle, as revealed by the presence of a track in the MS or characteristic energy deposits in the calorimeters. The

muon reconstruction is based primarily on information from the ID and MS tracking detectors. Information from the calorimeters is also used: in the determination of track parameters, to account for cases of large energy loss in the calorimeters, and for MS-independent tagging of ID tracks as muon candidates. The reconstruction of charged particles in the ID is described in Refs. [27, 28]. In the following, the MS track reconstruction as well as different muon identification algorithms based on the complete detector information are described. Additional details are available in Ref. [6].

4.1 Muon spectrometer stand-alone track reconstruction

The reconstruction of tracks in the MS starts with the identification of short straight-line local track segments reconstructed from hits in an individual MS station. Segments are identified in the individual stations by means of a Hough transform [29]. Segments in the different stations are combined into preliminary track candidates using a loose pointing constraint based on the IP and a parabolic trajectory that constitutes a first-order approximation to the muon bending in the magnetic field. Information from precision measurements in the bending plane is combined with measurements of the second coordinate from the trigger detectors to create three-dimensional track candidates. Finally, a global χ^2 fit of the muon trajectory through the magnetic field is performed, taking into account the effects of possible interactions in the detector material as well as the effects of possible misalignments between the different detector chambers.

Using the muon trajectory as obtained from the global χ^2 fit, outlier hits are removed and hits along the trajectory that were not assigned to the original track candidate are added. The track fit is then performed again using the updated hit information. Ambiguities are resolved by removing tracks that share a large fraction of hits with higher-quality tracks; an exception is made in the case of tracks that are identical in two stations but share no hits in a third station, to ensure a high efficiency for boosted low-mass dimuon systems. The final set of tracks is re-fitted with a loose IP constraint and taking into account the energy loss in the calorimeters, and back-extrapolated to the beam line. The p_{T} of the extrapolated track is then expressed at the IP.

4.2 Muon reconstruction based on complete detector information

Global muon reconstruction is performed using information from the ID and MS detectors as well as the calorimeters. The reconstruction proceeds according to five main reconstruction strategies, leading to the corresponding muon *types*: combined (CB), inside-out combined (IO), muon-spectrometer extrapolated (ME), segment-tagged (ST), and calorimeter-tagged (CT).

Combined muons are identified by matching MS tracks to ID tracks and performing a combined track fit based on the ID and MS hits, taking into account the energy loss in the calorimeters. Based on the particle trajectory from the combined fit, the muon spectrometer hits associated with the track may again be updated and the track fit repeated. For $|\eta| > 2.5$, MS tracks may be combined with short track segments reconstructed from hits in the pixel and SCT detectors, leading to a subset of CB muons referred to as silicon-associated forward (SiF) muons.

IO muons are reconstructed using a complementary inside-out algorithm, which extrapolates ID tracks to the MS and searches for at least three loosely-aligned MS hits. The ID track, the energy loss in the calorimeters and the MS hits are then used in a combined track fit. This algorithm does not rely on an

independently reconstructed MS track, and therefore recovers some efficiency, for example in regions of limited MS coverage and for low-p_{T} muons which may not reach the middle MS station.

If an MS track cannot be matched to an ID track, its parameters are extrapolated to the beamline and used to define an ME muon. Such muons are used to extend the acceptance outside that of the ID, thus fully exploiting the full MS coverage up to $|\eta| = 2.7$.

ST muons are identified by requiring that an ID track extrapolated to the MS satisfies tight angular matching requirements to at least one reconstructed MS segment. A successfully-matched ID track is identified as a muon candidate, and the muon parameters are taken directly from the ID track fit.

Finally, CT muons are identified by extrapolating ID tracks through the calorimeters to search for energy deposits consistent with a minimum-ionising particle. Such deposits are used to tag the ID track as a muon, and the muon parameters are again taken directly from the ID track fit. While the other muon reconstruction algorithms make use of ID tracks with p_{T} down to 2 GeV, a p_{T} threshold of 5 GeV is applied for CT muon reconstruction due to the large background contamination at low p_{T}.

The muon reconstruction described here features several improvements compared to that described in Ref. [7]:

- The use of a parabolic trajectory in the pattern recognition provides better matching between the segments in the different stations than the straight-line trajectory used previously.
- The introduction of SiF muons allows better use of the ID near the boundaries of its acceptance.
- Alignment uncertainties are now accounted for in the track fits via constrained nuisance parameters describing translational and rotational chamber displacements.
- The calorimeter-tagging algorithm has been retuned for improved purity in the region of limited MS coverage, $|\eta| < 0.1$, and an additional, looser working point has been introduced targeting high efficiency for use in tag-and-probe studies.

5 Identification

5.1 Identification criteria

After reconstruction, high-quality muon candidates used for physics analyses are selected by a set of requirements on the number of hits in the different ID subdetectors and different MS stations, on the track fit properties, and on variables that test the compatibility of the individual measurements in the two detector systems. A given set of requirements for each of the muon types defined in Section 4 is referred to as a selection *working point* (WP). Several WPs are defined to suit the needs of the wide variety of physics analyses involving final states containing muons. Different analyses have different requirements in terms of efficiency of prompt-muon identification, resolution of the momentum measurement, and rejection of background due to non-prompt muons. Among non-prompt muons, an explicit distinction is made between muon candidates originating from the semileptonic in-flight decay of light hadrons and those from hadrons containing heavy flavours. The selection WPs target the rejection of light hadrons, which in general result in lower-quality muon tracks, due to the change in trajectory stemming from the in-flight decay within the detector. Bottom and charm decays produce good-quality muon tracks and these can be distinguished from

prompt muons, which are more closely associated with the primary vertex and more isolated in the ID and/or in the calorimeters.

5.1.1 Design rationale for selection working points

The selection efficiency and purity in simulation are among the main metrics considered in the optimisation of the requirements defining each WP. In particular, the prompt muon efficiency of a selection WP represents the probability that a prompt muon traversing the detector is reconstructed as a muon and satisfies the WP. In a similar way, the purity of a selection WP is one minus the hadron misidentification rate, where the hadron misidentification rate is the fraction of light hadrons reconstructed as muons and satisfying the WP.

Three standard selection WPs are designed to cover the needs of the majority of physics analyses. In order of increasing purity and decreasing efficiency, these are the *Loose*, *Medium*, and *Tight* WPs, where the muons passing the *Medium* (*Tight*) WP requirements constitute a subset of those passing *Loose* (*Medium*). The *Medium* WP provides an efficiency and purity suitable for a wide range of analyses, while keeping the systematic uncertainties in the prompt-muon efficiency and background rejection small. The *Loose* selection WP was optimised for the reconstruction of Higgs boson decays in the four-muon final state, which, due to the high muon multiplicity and large signal-to-background ratio, benefits from a higher efficiency at the cost of less purity and larger systematic uncertainties. Finally, the *Tight* selection WP provides the highest purity, offering a substantially improved background rejection at the cost of a few percent efficiency loss for prompt muons compared to *Medium*. The *Tight* WP benefits analyses that are limited by background from non-prompt muons.

Two additional selection WPs are designed for analyses targeting extreme phase space regions. The *High-*p_T WP ensures an optimal momentum measurement for muons with p_{T} above 100 GeV. Optimised for W' and Z' searches, this WP provides the best momentum resolution and an optimal rejection of poorly reconstructed tracks affected by large uncertainties. The *Low-*p_T WP targets the lowest-p_{T} muons, which are less likely to be reconstructed as full tracks in the MS, so that identification based on MS segments is necessary. For these muons, the background from non-prompt muons can be large, and the *Low-*p_T WP exploits a set of variables providing a good separation between prompt muons and light-hadron decays to obtain an optimal background rejection while maintaining high efficiency. Two versions of the *Low-*p_T WP have been developed: a *cut-based* selection, which reduces the kinematic dependencies of the background efficiencies, simplifying the implementation of data-driven estimates, and a *multivariate* (MVA) WP, maximising the overall performance. Typical analyses that benefit from the use of the *Low-*p_T WP are measurements of Standard Model parameters in the quark-mixing sector [3], and searches for supersymmetry with compressed mass spectra [4].

In the following, the number of *precision stations* of a muon is defined as the number of MS stations in which the muon has at least three hits in the MDT or CSC detectors. A *precision hole station* is defined as a station where the muon has less than three hits and is missing at least three hits that are expected given its trajectory and the detector layout and operational status. The q/p compatibility is defined for CB and IO muons with an MS track as:

$$q/p \text{ compatibility} = \frac{|q/p_{\mathrm{ID}} - q/p_{\mathrm{MS}}|}{\sqrt{\sigma^2(q/p_{\mathrm{ID}}) + \sigma^2(q/p_{\mathrm{MS}})}},$$

where q/p_{ID} and q/p_{MS} are the measurements in the ID and MS of the ratio of the charge q to the momentum p of the muon, expressed at the IP, while $\sigma(q/p_{\mathrm{ID}})$ and $\sigma(q/p_{\mathrm{MS}})$ are the corresponding

uncertainties. Finally, ρ' is defined for CB and IO muons with an MS track as the absolute difference between the ID and MS p_{T} measurements divided by the p_{T} of the combined track:

$$\rho' = \frac{|p_{\mathrm{T,ID}} - p_{\mathrm{T,MS}}|}{p_{\mathrm{T,CB}}},$$

where $p_{\mathrm{T,ID}}$ and $p_{\mathrm{T,MS}}$ are respectively the muon p_{T} measured in the ID and in the MS, while $p_{\mathrm{T,CB}}$ is the value resulting from the combined track fit. No requirements on the q/p compatibility and ρ' variables are considered for muons without an ID or MS track, for which these variables are not defined.

All CB, IO, ST, and CT muons are subject to a common set of requirements on the ID track for all WPs. At least one hit in the pixel detector and at least five hits in the SCT detector are required, and at most two missing hits are allowed in total in these detectors. A missing hit is counted where the muon trajectory crosses an active sensor that does not register a hit. An exception is made for SiF muons, for which at least one pixel hit but only at least four hits in total in the pixel and SCT detectors are required at the reconstruction stage.

5.1.2 The *Loose*, *Medium*, and *Tight* selection working points

Within the ID acceptance $|\eta| < 2.5$, the *Medium* WP accepts only CB and IO muons. These are required to have at least two precision stations, except in the region $|\eta| < 0.1$, where muons with only one precision station are also included provided they have at most one precision hole station. The q/p compatibility is required to be less than seven to ensure a loose agreement between the ID and MS measurements. The acceptance is extended outside the ID coverage by including ME and SiF muons, required to have at least three precision stations, in the range $2.5 < |\eta| < 2.7$. Among prompt muons passing the *Medium* WP in $t\bar{t}$ events, more than 98% are CB muons.

The *Loose* selection WP accepts all the muons passing the *Medium* WP. In addition, it includes CT and ST muons in the range $|\eta| < 0.1$, where the gap in the MS coverage leads to a loss of efficiency for CB muon reconstruction. To increase the efficiency of the *Loose* criteria for low-p_{T} muons, IO muons with p_{T} below 7 GeV and only one precision station are accepted in the range $|\eta| < 1.3$, provided they are independently reconstructed also as ST muons. Requiring that IO muons are independently confirmed by the ST reconstruction strategy significantly increases their purity. Among prompt muons passing the *Loose* WP in $t\bar{t}$ events, about 97% are CB or IO muons. Approximately 1.5% are CT and ST muons in the region $|\eta| < 0.1$, among which the majority are CT muons. The efficiency increase of the *Loose* WP compared to *Medium* is around 20% for 3 GeV $< p_{\mathrm{T}} <$ 5 GeV and approximately 1–2% for higher p_{T}.

Among the muons passing the *Medium* selection WP, only CB and IO muons with at least two precision stations are accepted for the *Tight* WP. The normalised χ^2 of the combined track fit is required to be less than 8 to reject pathological tracks due to hadron decays in flight. Further requirements are placed on the q/p compatibility and ρ' depending on the p_{T} and $|\eta|$ of the muon. These are optimised to provide better background rejection for lower-p_{T} muons, because of the higher expected non-prompt background at low p_{T}. In the optimisation, the rejection of non-prompt muons is maximised for a given target prompt-muon efficiency that rises from approximately 91% at $p_{\mathrm{T}} = 4$ GeV to 95% at $p_{\mathrm{T}} = 9$ GeV and approaches 96% as the p_{T} approaches 20 GeV. For the region 6 GeV $< p_{\mathrm{T}} <$ 20 GeV, the *Tight* WP achieves a background reduction of more than 50% compared to *Medium*, with a corresponding efficiency loss for prompt muons of approximately 6%.

The performance of the *Loose*, *Medium* and *Tight* selection WPs for tracks with $p_{\mathrm{T}} > 10$ GeV in simulation is illustrated in Figure 1.

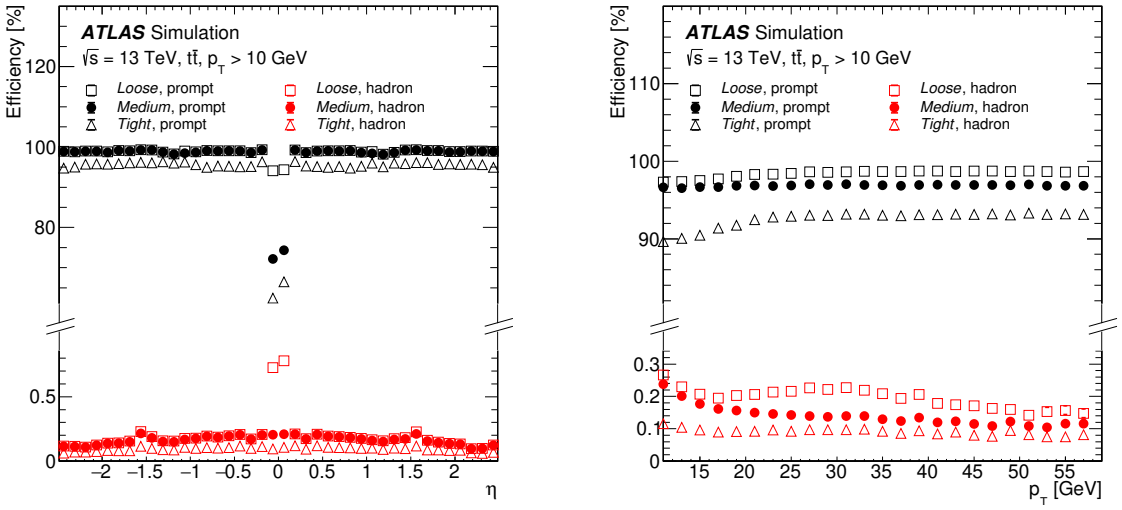


Figure 1: Efficiency as a function of η (left) and p_{T} (right) of the ID track for the *Loose*, *Medium* and *Tight* WP requirements in simulated $t\bar{t}$ events, shown separately for prompt muons and muons from light hadron decays. The efficiency is calculated as the fraction of ID tracks that are associated with a reconstructed muon passing the given WP requirements. The ID tracks are matched, respectively, to generator-level prompt muons or light hadrons.

5.1.3 The *High-p_T* selection working point

In the reconstruction of very high p_{T} muons with almost straight trajectories, the limiting factors are the intrinsic detector resolution of the individual measurements along the track and the knowledge of the relative alignment between the corresponding detector elements. The design resolution for stand-alone momentum measurements in the MS can only be achieved for muons with hits in at least three precision stations. For muons with only two precision stations, the resolution of the stand-alone measurement deteriorates significantly, but some of the loss in momentum resolution can be recovered through the combined track fit, which uses the hits in the ID as well.

Only CB and IO muons passing the *Medium* WP requirements are accepted for the *High-p_T* WP. At least three precision stations are required, with the following exceptions:

- For muons traversing the B-field inversion zones instrumented with additional chambers, at least four precision stations are required due to the particular trajectory of muons in this region.
- Muons with only two precision stations are accepted provided the missing hits are in the inner station, as this category of tracks shows a better momentum resolution than other tracks with less than three precision stations. They are, however, restricted to the $|\eta| < 1.3$ region, where the effects of relative misalignments between the ID and MS on muons with two precision stations are less pronounced.

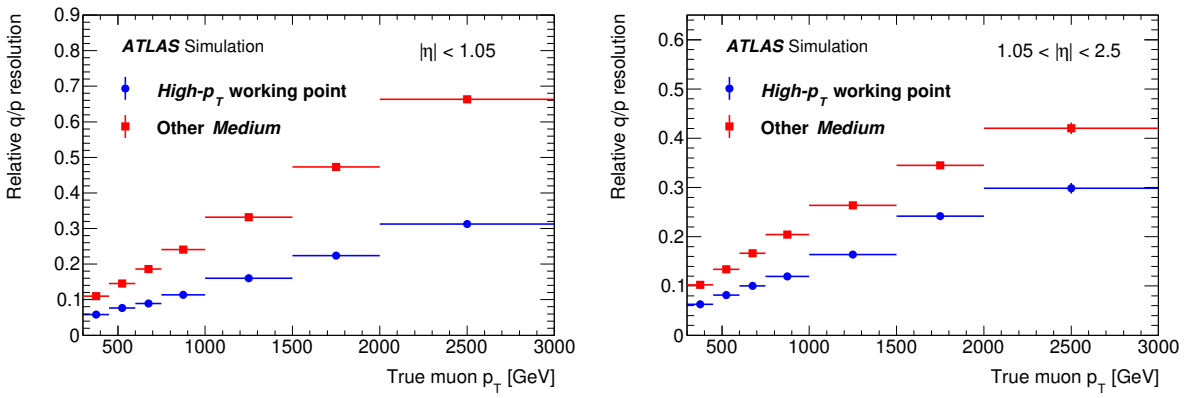


Figure 2: The q/p resolution as a function of the transverse momentum of muons in the barrel (left) and endcaps (right), shown separately for muons passing the *High-p_T* WP requirements and for the rest of the muons passing the *Medium* WP requirements. The resolutions are evaluated in MC samples that include realistic misalignments corresponding to the data-taking conditions in 2015.

Muons are rejected if their η and ϕ coordinates correspond to regions of the MS where the relative alignment between the traversed chambers is not known with sufficient precision. For this reason, all muons in the barrel–endcap overlap region $1.0 < |\eta| < 1.1$ are rejected, while partial acceptance losses also occur in $1.1 < |\eta| < 1.3$, and in the $|\eta| < 1.0$ region corresponding to the detector support structures, around $\phi = -1.2$ and $\phi = -2.0$.

The resolution of high-p_{T} muons is evaluated in MC samples that include a realistic simulation of relative misalignments between the MS chambers and between the ID and MS. The resolution is extracted from a Gaussian fit to the core of the distribution of relative residuals $[(q/p)_{\mathrm{reco}} - (q/p)_{\mathrm{truth}}]/(q/p)_{\mathrm{truth}}$, with $(q/p)_{\mathrm{reco}}$ and $(q/p)_{\mathrm{truth}}$ being the reconstructed and generated q/p values, respectively. Figure 2 shows the resolution as a function of p_{T} for muons passing the *High-p_T* WP requirements, and for comparison, the resolution for muons failing the *High-p_T* requirements but passing the *Medium* WP ones. As expected, superior resolution is obtained for the muons passing the *High-p_T* WP requirements, while the resolution for the rest of the muons passing *Medium* is worse by up to roughly a factor of two depending on the detector region and p_{T}.

An additional selection is placed on the estimated momentum uncertainty from the combined track fit to reject suboptimal momentum measurements. Specifically, the relative q/p uncertainty $\sigma_{\mathrm{rel}}(q/p) = \sigma(q/p)/|q/p|$ is required to be below a given threshold, defined as a p_{T}-dependent coefficient multiplied by the expected momentum resolution. The p_{T}-dependent coefficient is optimised separately for muons with different numbers of precision stations, and follows a decreasing trend for p_{T} greater than 1 TeV due to the presence of larger resolution tails at very high p_{T}. The expected resolution is parameterised as a function of p_{T} in five $|\eta|$ regions, separately for the muons with two precision stations and those with at least three. The resulting criterion, referred to as the $\sigma_{\mathrm{rel}}(q/p)$ selection hereafter, is more than 99% efficient at $p_{\mathrm{T}} = 1$ TeV for muons with at least three precision stations. The efficiency decreases slightly for higher p_{T}, reaching approximately 96% at $p_{\mathrm{T}} = 2$ TeV and 89% at $p_{\mathrm{T}} = 2.5$ TeV. For muons with only two precision stations, the $\sigma_{\mathrm{rel}}(q/p)$ selection is more stringent, with an efficiency of around 50% for p_{T} between 1 and 2 TeV.

A p_{T}-dependent uncertainty in the efficiency of the $\sigma_{\mathrm{rel}}(q/p)$ selection is assigned. As the impact of the selection becomes sizeable only at very high p_{T}, where the available number of muons from $Z \to \mu\mu$

decays is limited, the uncertainty is evaluated from an inclusive sample of muons with high p_{T}. All muons in the sample are required to satisfy the *High-p_T* WP criteria, not including the $\sigma_{\mathrm{rel}}(q/p)$ selection. The fraction of muons that also pass the $\sigma_{\mathrm{rel}}(q/p)$ selection is compared between data and Drell–Yan dimuon MC samples covering the invariant mass range up to several TeV. The difference is assigned as the uncertainty in the selection efficiency, which becomes a dominant source of uncertainty at very high p_{T}, approaching for example 55% for p_{T} above 3 TeV in the region $|\eta| < 1.3$.

The overall reconstruction and selection efficiency of the *High-p_T* WP criteria for muons in Z/γ^* events, simulated with realistic detector misalignments corresponding to the data taking conditions in 2015, is about 80% at $p_{\mathrm{T}} = 100$ GeV, and decreases approximately to 76% at $p_{\mathrm{T}} = 500$ GeV, 72% at $p_{\mathrm{T}} = 1$ TeV, and 68% at $p_{\mathrm{T}} = 2$ TeV.

5.1.4 The *Low-p_T* selection working point

Only CB and IO muons are used in the *Low-p_T* selection WP. Muons, on average, lose roughly 3 GeV of their energy while traversing the calorimeters. At very low p_{T}, a muon may not reach the middle station of the MS, or even the MS itself, leading to a loss of efficiency for stand-alone MS track reconstruction. For this reason, a significant fraction of muons in this p_{T} region are reconstructed only by the IO algorithm, and these are required to be independently reconstructed also as ST muons for increased purity. At least one precision station is required, except in the region $|\eta| > 1.3$, where muons with p_{T} greater than 3 GeV generally have enough energy to reach the second station and thus the requirement is at least two. For p_{T} above 10 GeV, the efficiency improvement relative to *Medium* becomes marginal, and the *Low-p_T* WP is defined to be identical to *Medium* above $p_{\mathrm{T}} = 18$ GeV.

Further selection requirements are imposed to reject light-hadron decays. CB and IO muon tracks resulting from hadron decays in flight are characterised by a distinctive *kink* along the trajectory in the ID due to the momentum carried away by the undetected neutrino. Several variables offering good discrimination between prompt and non-prompt muons are exploited in the *Low-p_T* WP. For the cut-based WP, selection requirements are imposed independently on the individual discriminating variables, while the multivariate WP further exploits correlations by combining several discriminating variables in a boosted decision tree (BDT).

Three variables quantifying the presence of a kink on the muon track are used to define the cut-based WP: the momentum balance significance (MBS), the scattering neighbour significance (SNS), and the scattering curvature significance (SCS). The MBS is defined as:

$$\mathrm{MBS} = \frac{|p_{\mathrm{ID}} - \hat{p}_{\mathrm{MS}} - E_{\mathrm{loss}}|}{\sigma(E_{\mathrm{loss}})},$$

where p_{ID} and $\hat{p}_{\mathrm{MS}}$ are respectively the momentum measured in the ID and in the MS, with the latter expressed at the entrance of the MS, E_{loss} the energy loss in the calorimeter system, and $\sigma(E_{\mathrm{loss}})$ its uncertainty. For muons with no momentum measured in the MS, MBS is set to 0. The SNS and SCS are variables estimating the significance of a change in trajectory (kink) along the track under the hypothesis of a decay vertex between adjacent hits, as expected in the presence of a hadron decaying to a muon. The SNS is defined as the largest value of scattering angle significance over the entire track. Scattering angle significance is computed considering pairs of adjacent hits along the track, and evaluated as the angular distance in the bending plane between the two half tracks ending/starting at each of the hits, divided by the corresponding uncertainty. The SCS looks for the most pronounced discontinuity along the track by

evaluating the integral of the scattering angle significances before/after the hypothesized decay vertex. It considers all possible pairs of partial tracks starting/ending at each of the hits, and is computed as the maximum, in absolute value and among all pairs, of the difference between the two sums of significances along each partial track. It is then normalized to the square root of the total number of pairs. For the cut-based *Low-p_T* WP, each of the three significance variables is required to be below three. Furthermore, in the region $|\eta| > 1.55$, the *Medium* WP requirements have a high efficiency for low-p_{T} muons, and are applied in addition for further reduction of the background from non-prompt muons in this region.

The multivariate *Low-p_T* selection WP is based on a gradient BDT which is trained on separate samples containing prompt muons from W boson decays and non-prompt muons from light-hadron decays, respectively, in both cases from simulated $t\bar{t}$ events. The training is performed separately for muons reconstructed by the CB and IO algorithms, using in both cases the same set of discriminating variables. A total of eight variables are deployed, which provide good discriminating power between prompt and non-prompt muons, and are well modelled in the MC simulation. The variables used include SCS, SNS, and MBS, as well as additional ones that take advantage of different information from the detector: the energy loss in the calorimeters, the number of MS segments associated with the muon and their direction relative to the track in the ID, and the number of missing precision hits in the middle MS station.

The modelling of all variables in simulation is verified by a comparison with data in dedicated control regions with a high purity of low-p_{T} prompt muons and muons from hadron decays. The modelling for prompt muons is evaluated using a selection targeting the J/ψ resonance. The modelling for muons from hadron decays is evaluated using a selection targeting the decay $B_s^0 \to J/\psi\,\phi$ with subsequent decays $J/\psi \to \mu\mu$ and $\phi \to K^+K^-$. The two muons are required to satisfy the *Medium* WP requirements and have an invariant mass close to the J/ψ mass. A B_s^0 candidate is reconstructed by matching the muons to a common vertex with two ID tracks that have an invariant mass close to the ϕ mass. A high purity of B_s^0 events is attained by selecting candidates where the four-particle invariant mass is close to the B_s^0 mass, and the corresponding sideband regions are used to estimate the background. The modelling is checked for muon candidates matched to the ID tracks forming the ϕ candidate.

The distributions of the gradient BDT score for prompt and non-prompt muons are shown in Figure 3, where good separation between the two categories is observed. Good agreement is observed when comparing the distributions obtained from the event sample used for the BDT training to those extracted from a statistically independent sample, indicating that there is no overtraining of the BDT.

The performance of the cut-based and multivariate *Low-p_T* selection WPs in simulation is compared with that of the *Medium* selection WP in Figure 4. Relative to *Medium*, the cut-based *Low-p_T* WP achieves a substantial increase in the prompt-muon efficiency in the barrel region while retaining good rejection of non-prompt muons. In the endcap regions, improved rejection of light-hadron decays is achieved at the cost of a small prompt-muon efficiency loss. Relative to the cut-based *Low-p_T* WP, the multivariate WP achieves better rejection of non-prompt muons in the barrel region and a higher prompt-muon efficiency in the endcap regions. Overall, compared to the *Medium* selection WP, the cut-based (multivariate) *Low-p_T* WP accepts an additional 16% (18%) of the prompt muons with 3 GeV $< p_{\mathrm{T}} <$ 5 GeV, while the corresponding increase for light hadrons is approximately 0.2% (0.1%).

5.1.5 Efficiencies and misidentification rates

The prompt muon efficiencies and light-hadron misidentification rates for muons in the region $|\eta| < 2.5$ are shown in Table 1. In this case, the efficiency is calculated for each selection WP as the fraction of ID

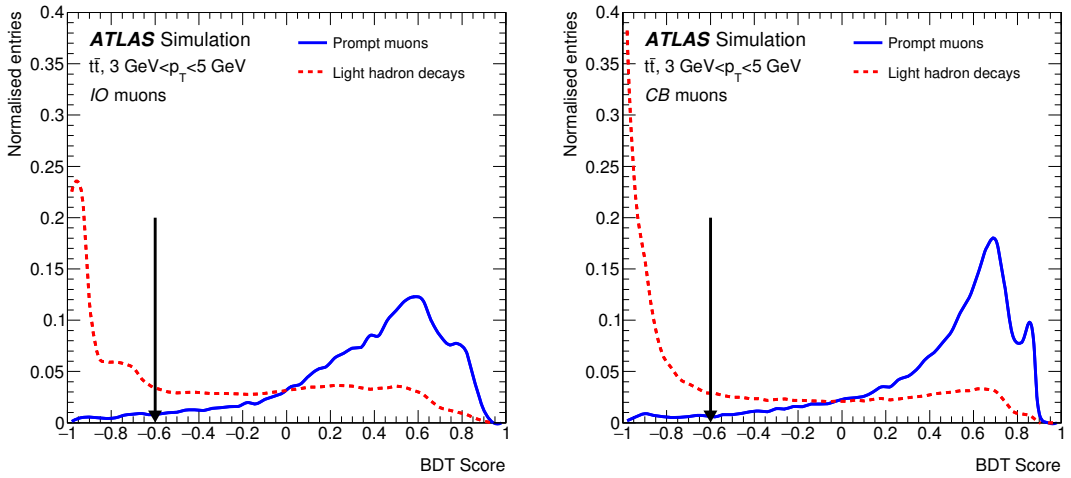


Figure 3: Distributions of the gradient BDT score for muons reconstructed with the IO algorithm (left) and CB algorithm (right) in simulated $t\bar{t}$ events. The distributions are shown for prompt muons (full line, blue), and for light hadron decays (dashed line, red). The black arrows indicate the values of the requirements that define the multivariate *Low-*p_T selection.

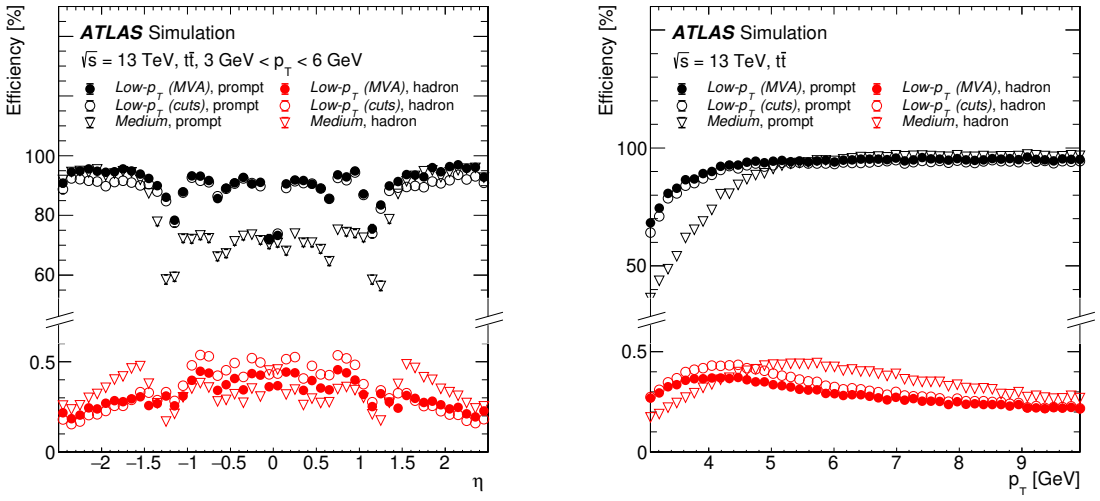


Figure 4: Efficiency as a function of η (left) and p_{T} (right) of the ID track for the *Low-*p_T and *Medium* WP requirements in simulated $t\bar{t}$ events, shown separately for prompt muons and muons from light hadron decays. The efficiency is calculated as the fraction of ID tracks that are associated with a reconstructed muon passing the given WP requirements. The ID tracks are matched, respectively, to generator-level prompt muons or light hadrons. Both the cut-based and multivariate *Low-*p_T WPs are shown.

Table 1: Prompt-muon efficiencies ϵ_μ and light-hadron misidentification rates ϵ_{had} for the different selection working points, evaluated in a $t\bar{t}$ MC sample in different p_{T} regions for $|\eta| < 2.5$. It should be noted that the *Tight* WP by construction does not select any muons with $p_{\text{T}} < 4$ GeV, which is reflected in the corresponding efficiency in the first p_{T} region. The statistical uncertainties are at least one order of magnitude smaller than the last digit reported.

	$3 < p_{\text{T}}$ [GeV] < 5		$5 < p_{\text{T}}$ [GeV] < 20		$20 < p_{\text{T}}$ [GeV] < 100		$p_{\text{T}} > 100$ GeV	
Selection WP	ϵ_μ [%]	ϵ_{had} [%]	ϵ_μ [%]	ϵ_{had} [%]	ϵ_μ [%]	ϵ_{had} [%]	ϵ_μ [%]	ϵ_{had} [%]
Loose	90	1.17	98	1.06	99	0.25	98	0.12
Medium	70	0.63	97	0.85	97	0.17	97	0.07
Tight	36	0.15	90	0.38	93	0.12	93	0.04
Low-p_T (cut-based)	86	0.82	95	0.71	97	0.17	97	0.07
Low-p_T (multivariate)	88	0.73	96	0.66	97	0.17	97	0.07
High-p_T	45	0.34	79	0.60	80	0.13	80	0.05

tracks associated with a reconstructed muon passing the given WP requirements. It is evaluated in a $t\bar{t}$ MC sample, for ID tracks matched to generator-level prompt muons from W boson decays. Similarly, the misidentification rate is calculated using ID tracks matched to generator-level hadrons.

As expected, the highest prompt-muon efficiency is achieved for the *Loose* selection WP, while the *Tight* WP achieves the lowest misidentification rate. In the region 3 GeV $< p_{\text{T}} < 5$ GeV, the *Low-*p_T WP offers an efficiency close to that of *Loose*, with a significantly lower misidentification rate. The efficiency of the *High-*p_T WP is significantly lower than that of all the other WPs due to the strict requirements necessary to achieve optimal momentum resolution. The misidentification rates are further reduced by approximately one order of magnitude, or more, after the application of vertex association and isolation requirements, discussed in the following sections.

5.2 Vertex association criteria

Selection requirements are imposed on the impact parameters of the muon track to reject muons originating from hadron decays in flight as well as muons not originating from the hard-scattering proton–proton interaction, for example those due to pile-up interactions or cosmic rays. The transverse impact parameter $|d_0|$ is the distance from the beamline to the point of closest approach of the muon track in the transverse plane. It is measured relative to the actual beam position rather than the reconstructed primary vertex,[3] as the beam width is smaller than the typical uncertainty in the reconstructed primary vertex position in the transverse plane. The longitudinal impact parameter z_0 is the coordinate along the beam axis of the point of closest approach of the muon track to the beamline, measured relative to the reconstructed primary vertex position. Consequently, the shortest distance from the muon track to the primary vertex in a longitudinal projection is $|z_0| \sin\theta$, where θ is the polar angle of the muon track. For tracks with $p_{\text{T}} > 10$ GeV, the impact parameter resolution approaches asymptotically a value of about 10 μm in the transverse plane and 50 μm in the longitudinal direction, while it degrades progressively at lower transverse momenta as a consequence of multiple scattering in the detector material.

The transverse impact parameter selection requirement is defined in terms of the d_0 *significance*, $|d_0|/\sigma(d_0)$, which is required to be less than three. Due to the excellent tracking resolution for muons with intermediate to high p_{T}, the beam width is not negligible compared to the estimated uncertainty in d_0 from the track fit,

[3] Collision vertices are reconstructed from ID tracks that satisfy $p_{\text{T}} > 0.5$ GeV, and the primary vertex is chosen as the vertex with the largest $\sum p_{\text{T}}^2$ for the tracks associated with this vertex.

and is hence accounted for in the total uncertainty $\sigma(d_0)$. Finally, the muon track is ensured to be compatible with originating from the reconstructed primary vertex by the requirement $|z_0| \sin\theta < 0.5$ mm.

5.3 Isolation requirements

Muons from prompt decays of SM bosons or hypothetical BSM particles can be discriminated from muons from hadronic sources by measuring the amount of hadronic activity in their vicinity. The transverse energy (or momentum if considering only tracks) reconstructed in a cone around a muon and divided by the muon p_{T} defines the muon isolation. Depending on the topology, most non-prompt muons that can be rejected using isolation criteria originate from heavy-flavour hadron decays. Conversely, the contributions from light-hadron decays or hadrons misidentified as muons are generally efficiently suppressed by the selection requirements described in Sections 5.1 and 5.2. Isolation can be measured independently using either the ID (with ID tracks [30]) or the calorimeters (with topological cell clusters [31]), or through a combination of the two (with particle flow [32]). Several isolation WPs are defined, balancing prompt-muon acceptance, rejection of non-prompt muons, and performance in close proximity to other objects.

Track-based isolation is defined as the scalar sum of the transverse momenta of the ID tracks associated with the primary vertex in an η–ϕ cone of a given size ΔR around the muon, excluding the muon track itself. Depending on the isolation selection criterion, ΔR is either 0.2, labelled as $p_{\mathrm{T}}^{\mathrm{cone20}}$, or min(10 GeV/$p_{\mathrm{T}}^{\mu}$, 0.3), labelled as $p_{\mathrm{T}}^{\mathrm{varcone30}}$, where the latter is optimised for topologies where jets or other leptons are expected in close proximity to an energetic muon [33]. In order to increase the rejection of hadronic activity, some isolation selection criteria use $p_{\mathrm{T}}^{\mathrm{varcone30}}$ for $p_{\mathrm{T}}^{\mu} < 50$ GeV and $p_{\mathrm{T}}^{\mathrm{cone20}}$ for $p_{\mathrm{T}}^{\mu} > 50$ GeV. The minimum transverse momentum of tracks used in the calculation varies for each isolation criterion and can be either 500 MeV or 1 GeV. Track-based isolation variables are largely independent of pile-up, due to the rejection of tracks originating from pile-up vertices or with large transverse impact parameters relative to the primary vertex. All muon isolation WPs include a selection on one track-based isolation variable, with or without an additional criterion for calorimeter-based or particle-flow-based isolation.

Calorimeter-based isolation, labelled as $E_{\mathrm{T}}^{\mathrm{topocone20}}$, is defined as the sum of the transverse energy of topological cell clusters in a cone of size $\Delta R = 0.2$ around the position of the muon, extrapolated to the calorimeters, after subtracting the contribution from the energy deposit of the muon itself and correcting for pile-up effects. Contributions from pile-up and the underlying event are estimated using an ambient energy-density technique and are corrected on an event-by-event basis, similarly to the pile-up correction performed in the ATLAS jet calibration [34]. This technique, although it corrects calorimeter-based isolation for the effects of pile-up on average, results in poor energy resolution due to the large size of the pile-up correction relative to the average calorimeter isolation values. As a result, the performance of calorimeter-based isolation tends to have more pile-up dependence than track-based isolation, and all criteria that include a requirement on calorimeter-based isolation also apply a more stringent selection on track-based isolation.

Combining selections on track-based and calorimeter-based isolation generally results in better performance than employing one but not the other, as the two isolation variables provide complementary information. Track-based isolation has better resolution and lower pile-up dependence than calorimeter isolation, and the ID provides a better transverse momentum scale and resolution than the calorimeters for individual soft hadrons. On the other hand, calorimeter-based isolation includes neutral particles and particles below the ID track p_{T} threshold, which are otherwise ignored by track isolation. However, track and calorimeter isolation measure hadronic activity in a redundant manner, as charged particles are measured by both the

calorimeters and the ID. The particle-flow algorithm allows removal of overlapping contributions from the track-based and calorimeter-based isolation, decreasing the correlation between the two variables.

The particle-flow-based isolation variable is defined as the sum of track-based isolation, chosen in the configuration with $p_{\mathrm{T}}^{\mathrm{varcone30}}$ for $p_{\mathrm{T}}^{\mu} < 50$ GeV and $p_{\mathrm{T}}^{\mathrm{cone20}}$ for $p_{\mathrm{T}}^{\mu} > 50$ GeV, and the transverse energy of neutral particle-flow objects in a cone of size $\Delta R = 0.2$ around the muon, labelled as $E_{\mathrm{T}}^{\mathrm{neflow20}}$. The latter is corrected for the contribution from the energy deposit of the muon itself and for pile-up effects, and is assigned a weighting factor $w = 0.4$, optimised to maximise the rejection of heavy-flavour hadron decays in the desired range of prompt-muon efficiencies. Contributions from pile-up and the underlying event are estimated using the ambient energy-density technique and are corrected for on an event-by-event basis. As with the calorimeter isolation, this pile-up correction can result in poor resolution. However, due to the removal of the contribution from charged particles, the average contribution from pile-up to neutral particle-flow isolation is much smaller than the contribution to calorimeter isolation, and as a result, the pile-up dependency of the efficiency for isolation selections based on neutral particle flow is decreased.

Figure 5 shows the behaviour of the previously defined isolation variables, after dividing their values by the p_{T} of the muon, for prompt and non-prompt muons extracted from simulated $t\bar{t}$ events. As expected, the distributions for prompt muons show a sharp peak near zero, while those for non-prompt muons are relatively flat.

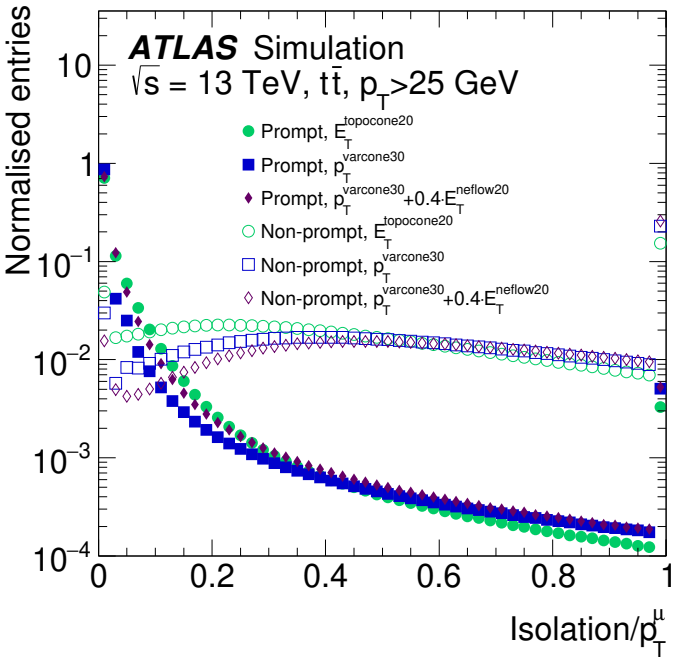


Figure 5: Distributions of the isolation variables defined in Section 5.3, after dividing their value by the p_{T} of the muon. Prompt and non-prompt muons are extracted from simulated $t\bar{t}$ events. The distributions are normalised to unit area. The rightmost bin contains all the events exceeding the range of the horizontal axis.

A multivariate discriminant, *prompt lepton BDT* [35], is developed for physics analyses that need the highest rejection of non-prompt muons such as $t\bar{t}H$ searches [35, 36] and WWW measurements [37]. This discriminant is based on a BDT exploiting eight input variables to maximise the rejection power for non-prompt muons from heavy-flavour hadrons: calorimeter and track isolation, information about

tracks within a cone of size $\Delta R = 0.4$ around the muon including the track multiplicity, and the likelihood of originating within a jet stemming from a b-hadron decay, calculated using the DL1mu or RNNIP algorithms [38]. The training is performed using the $t\bar{t}$ MC sample with two separate ranges of muon transverse momentum, 3 GeV $< p_{\mathrm{T}} <$ 10 GeV and $p_{\mathrm{T}} >$ 10 GeV, to account for the drastic change in the distributions of the input variables.

The various isolation WPs are summarised in Table 2. A track-only isolation WP is the most robust with respect to pile-up and suffers the lowest drop in efficiency from nearby objects. Two loose isolation WPs are defined using track isolation and either calorimeter or neutral particle-flow isolation and are optimised for cases where high prompt-muon efficiency is prioritised over rejection of non-prompt muons. Two tight isolation WPs are defined using track isolation and either calorimeter or neutral particle-flow isolation and are optimised for cases suffering from large backgrounds from non-prompt muons. Moreover, two isolation WPs are defined using the *prompt lepton BDT*: *PLBDTLoose* and *PLBDTTight*. In addition to a loose cut on the track isolation, a p_{T}-dependent BDT threshold selection is applied in each of these to achieve the same prompt-muon efficiency as the *TightTrackOnly* and *Tight* isolation WPs, respectively.

Table 2: Definitions of the muon isolation WPs. The criteria used are listed in the second column, while the requirement on the minimum track p_{T} is shown in the third column. WPs marked with * exist in two variants: one with the cone ΔR parameter decreasing with p_{T}^{μ} as min(10 GeV/p_{T}^{μ}, 0.3), the other remaining constant at $\Delta R = 0.2$ for $p_{\mathrm{T}}^{\mu} > 50$ GeV.

Isolation WP	Definition	Track p_{T} requirement
*PflowLoose**	$(p_{\mathrm{T}}^{\mathrm{varcone30}} + 0.4 \cdot E_{\mathrm{T}}^{\mathrm{neflow20}}) < 0.16 \cdot p_{\mathrm{T}}^{\mu}$	$p_{\mathrm{T}} > 500$ MeV
*PflowTight**	$(p_{\mathrm{T}}^{\mathrm{varcone30}} + 0.4 \cdot E_{\mathrm{T}}^{\mathrm{neflow20}}) < 0.045 \cdot p_{\mathrm{T}}^{\mu}$	
*Loose**	$p_{\mathrm{T}}^{\mathrm{varcone30}} < 0.15 \cdot p_{\mathrm{T}}^{\mu}$, $E_{\mathrm{T}}^{\mathrm{topocone20}} < 0.3 \cdot p_{\mathrm{T}}^{\mu}$	$p_{\mathrm{T}} > 1$ GeV
*Tight**	$p_{\mathrm{T}}^{\mathrm{varcone30}} < 0.04 \cdot p_{\mathrm{T}}^{\mu}$, $E_{\mathrm{T}}^{\mathrm{topocone20}} < 0.15 \cdot p_{\mathrm{T}}^{\mu}$	
HighPtTrackOnly	$p_{\mathrm{T}}^{\mathrm{cone20}} < 1.25$ GeV	$p_{\mathrm{T}} > 1$ GeV
*TightTrackOnly**	$p_{\mathrm{T}}^{\mathrm{varcone30}} < 0.06 \cdot p_{\mathrm{T}}^{\mu}$	
PLBDTLoose (PLBDTTight)	$p_{\mathrm{T}}^{\mathrm{varcone30}} < \max(1.8\ \mathrm{GeV}, 0.15 \cdot p_{\mathrm{T}}^{\mu})$ BDT cut to mimic *TightTrackOnly* (*Tight*) efficiency	$p_{\mathrm{T}} > 1$ GeV

The efficiencies for prompt muons and muons from bottom and charm semileptonic decays in $t\bar{t}$ MC events are summarised in Table 3, for tracks satisfying the *Medium* identification and the vertex association selections. For these tracks, the suppression factor, defined as the inverse of the efficiency, for muons from bottom and charm semileptonic decays in $t\bar{t}$ simulation ranges from 8 (12) at very low p_{T} to 20 (100) for $p_{\mathrm{T}} > 25$ GeV for the *PflowLoose* (*PflowTight*) criteria. The highest suppression factor achieved is 250, and is obtained with the *PLBDTTight* criteria around $p_{\mathrm{T}} = 30$ GeV.

6 Methodology for efficiency measurements

Two different methods are used to measure the reconstruction, identification, isolation and vertex association efficiencies with high precision.

In the $|\eta| < 2.5$ region, corresponding to the ID acceptance, two independent detectors are available and the tag-and-probe method detailed in Section 6.1 is used. Section 6.2 describes the measurements of the reconstruction and identification efficiencies for muons with p_{T} greater than 15 GeV, and of the isolation and vertex association efficiencies down to $p_{\mathrm{T}} = 3$ GeV, with an almost pure sample of $Z \to \mu\mu$ events.

Table 3: Isolation efficiencies for prompt muons, ϵ_μ, and muons from bottom and charm semileptonic decays, ϵ_{HF}, for the different isolation working points, evaluated in a $t\bar{t}$ MC sample in different p_{T} regions for tracks satisfying the *Medium* identification and the vertex association criteria. The isolation working points considered correspond to the variants with the cone size remaining constant at $\Delta R = 0.2$ for $p_{\text{T}}^{\mu} > 50$ GeV. The statistical uncertainties are at least one order of magnitude smaller than the last digit reported.

	$3 < p_{\text{T}}$ [GeV] < 5		$5 < p_{\text{T}}$ [GeV] < 20		$20 < p_{\text{T}}$ [GeV] < 100		$p_{\text{T}} > 100$ GeV	
Isolation WP	ϵ_μ [%]	ϵ_{HF} [%]	ϵ_μ [%]	ϵ_{HF} [%]	ϵ_μ [%]	ϵ_{HF} [%]	ϵ_μ [%]	ϵ_{HF} [%]
Loose	63	14.3	86	7.2	97	6.1	99	12.7
Tight	53	11.9	70	4.2	89	1.0	98	1.6
PflowLoose	62	12.9	86	6.8	97	5.0	99	9.1
PflowTight	45	8.5	63	3.1	87	0.9	97	0.8
HighPtTrackOnly	92	35.9	92	17.2	92	4.5	92	0.6
TightTrackOnly	80	19.9	81	7.0	94	3.2	99	3.3
PLBDTLoose	81	17.4	83	5.1	93	1.3	98	1.7
PLBDTTight	57	9.6	69	2.7	87	0.5	98	1.7

$J/\psi \to \mu\mu$ events, selected as detailed in Section 6.3, are deployed to further extend the reconstruction and identification efficiency measurements down to $p_{\text{T}} = 3$ GeV.

In the $2.5 < |\eta| < 2.7$ region, muons are reconstructed only as ME of SiF muons. The level of agreement between collision data and detector simulation is measured via the method summarised in Section 6.4.

6.1 The tag-and-probe method in the $|\eta| < 2.5$ region

The tag-and-probe method is based on the selection of a sample containing dimuon pairs, for example from $Z \to \mu\mu$ decays, via a set of requirements on the event topology used to reduce the background contamination. One leg of the decay, the *tag*, is required to satisfy stringent identification criteria and to have triggered the online event selection. The second muon candidate in the pair, the *probe*, is used to test the efficiency of a certain reconstruction algorithm or of certain selection criteria. Probes are usually required to be reconstructed with a detector subsystem independent of the one under study.

Several types of probes are used to measure the various efficiencies:

- ID probes are ID tracks used to measure the reconstruction efficiency in the MS, or of specific identification algorithms.
- MS probes are ME tracks used to test the efficiency of the ID reconstruction.
- CT probes are ID tracks also satisfying the calo-tagging reconstruction algorithm described in Section 4. In the same way as the ID probes, they are used to measure the reconstruction efficiency in the MS, or of specific muon identification algorithms.
- ST probes are ID tracks also satisfying the segment-tagging reconstruction algorithm described in Section 4. In the same way as the ID probes, they are used to measure the reconstruction efficiency in the MS, or of specific muon identification algorithms.

- *Two-track* probes are MS tracks required to be within $\Delta R = 0.05$ of an ID track. They are used to measure the combined reconstruction efficiency of a muon candidate with ID and MS tracks, or the efficiency of specific identification criteria.
- *Loose* probes are muon candidates satisfying the *Loose* identification requirements. They are used to measure the isolation and vertex association efficiencies.

The efficiency of a certain algorithm is measured using a matching requirement of $\Delta R < 0.05$ between the given probe and any muon candidate reconstructed and identified with the algorithm of interest. The efficiency is then computed as the number of probes P that are successfully matched to a muon reconstructed and identified according to the X criterion, N_P^X, divided by the total number of selected probes N_P^{All}:

$$\epsilon\left(X|P\right) = \frac{N_P^X}{N_P^{\text{All}}}.$$

Probes are counted in data events after the subtraction of the backgrounds, using different techniques in the $J/\psi \to \mu\mu$ and in the $Z \to \mu\mu$ data sets. In simulation, to eliminate any background contamination, both the tag and the probe muons are required to be a prompt muon at generator level.

The level of agreement between the efficiency measured in data for a given algorithm X, $\epsilon^{\text{Data}}\left(X\right)$, and the corresponding efficiency in simulation, $\epsilon^{\text{MC}}\left(X\right)$, is assessed via the ratio of these two numbers, called the efficiency scale factor (SF):

$$\text{SF} = \frac{\epsilon^{\text{Data}}\left(X\right)}{\epsilon^{\text{MC}}\left(X\right)}.$$

In the ratio, possible biases introduced by the measurement method which appear both in data and MC simulation cancel out. The SF quantifies the deviation of the simulation from the real detector behaviour, and is therefore used in physics analysis to correct the simulation.

6.2 Efficiency measurements with $Z \to \mu\mu$ decays

To select $Z \to \mu\mu$ decays, the invariant mass $m_{\text{tag–probe}}$ of the tag-and-probe pair is required to be between 61 and 121 GeV. The tag muon is required to satisfy the *Medium* identification criteria, $p_{\text{T}} > 27$ GeV, $|\eta| < 2.5$, and the single-muon trigger requirements described in Section 3. In order to suppress the contamination from misidentified candidates from jet activity, the tag must fulfil the *Tight* isolation criteria. Furthermore, the vertex association criteria ensure a maximal purity of tags originating from the hard-scattering proton–proton collision. The probes have to satisfy $p_{\text{T}} > 3$ GeV and $|\eta| < 2.5$. Additional requirements that are specific to the different measurements described in Sections 6.2.1, 6.2.2, and 6.2.3 are also employed.

6.2.1 Reconstruction and identification efficiencies

To minimise the systematic uncertainties, a maximal purity in the selection of $Z \to \mu\mu$ decays is mandatory, and additional criteria are applied to the probe: $p_{\text{T}} > 10$ GeV is required, and the impact parameters of the probe track must satisfy $|d_0/\sigma\left(d_0\right)| < 3$ and $|z_0| < 10$ mm. Moreover, the probe must carry opposite charge relative to the tag, and fulfil an isolation selection which consists of stricter calorimeter-based and looser track-based isolation criteria than the *Tight* isolation WP.

After tightening the tag-and-probe selection, the purity of $Z \to \mu\mu$ decays in the probe sample is about 99.9%. Diboson production involving $Z \to \mu\mu$ decays and contributions from $Z \to \tau\tau$ and $t\bar{t}$ are considered as signal in the efficiency calculation, and account for about 0.06% of the selected sample. The contributions arising from processes such as $W(\to \mu\nu)$+jets and multi-jet events, where the probes stem from pion, kaon or heavy-flavour decays, account for the remaining fraction and amount to less than 0.05%.

The method described in Refs. [39] and [7] expressed the efficiency of the reconstruction and identification algorithm X (X = *Loose*, *Medium*, *Tight*, *Low-p_T*, *Low-p_T-MVA*, *High-p_T*) in terms of conditional probabilities:

$$\epsilon\,(X) = \epsilon\,(\mathrm{ID}) \times \epsilon\,(X|\mathrm{ID}) \simeq \epsilon\,(X|\mathrm{CT}) \times \epsilon\,(\mathrm{ID}|\mathrm{MS})\,. \tag{1}$$

In Eq. (1), $\epsilon\,(X)$ is factorised as the measured tracking efficiency in the ID, $\epsilon\,(\mathrm{ID})$, multiplied by the conditional probability $\epsilon\,(X|\mathrm{ID})$ that a muon track reconstructed in the ID is also reconstructed and identified with the X algorithm. The validity of this procedure is guaranteed by the fact that the track reconstruction in the ID is independent of that in the MS, and of the other details of the muon identification algorithms. However, $\epsilon\,(\mathrm{ID})$ cannot be measured directly. It is therefore replaced, in Eq. (1), by $\epsilon\,(\mathrm{ID}|\mathrm{MS})$, the conditional efficiency for a muon reconstructed by the MS to be also reconstructed in the ID. The quantity $\epsilon\,(\mathrm{ID}|\mathrm{MS})$ is computed as the fraction of MS probes matched to an ID track. To further reduce the background contamination, the $\epsilon\,(X|\mathrm{ID}) \simeq \epsilon\,(X|\mathrm{CT})$ approximation was used, replacing ID probes with the more pure CT probes, and a systematic uncertainty was assigned to cover for the small bias introduced.

In order to improve the precision of the measurement, the approach above was revised, and four different contributions to $\epsilon\,(X)$ are now considered explicitly:

$$\begin{aligned}\epsilon\,(X) &\simeq \epsilon\,(X|\mathrm{ID}\wedge\mathrm{MS}) \times \epsilon\,(\mathrm{MS}|\mathrm{ID}) \times \epsilon\,(\mathrm{ID}|\mathrm{MS}) + \epsilon\,(X\wedge\neg\mathrm{MS}|\mathrm{ID}) \times \epsilon\,(\mathrm{ID}|\mathrm{MS}) \\ &\simeq \left[\epsilon\,(X|\mathrm{ID}\wedge\mathrm{MS}) \times \epsilon\,(\mathrm{MS}|\mathrm{CT}) + \epsilon\,(X\wedge\neg\mathrm{MS}|\mathrm{CT})\right] \times \epsilon\,(\mathrm{ID}|\mathrm{MS})\,.\end{aligned} \tag{2}$$

Each of the terms appearing on the right-hand side of Eq. (2) is measured separately. The first term, $\epsilon\,(X|\mathrm{ID}\wedge\mathrm{MS})$, is the component of the X reconstruction and identification efficiency conditional on the combined reconstruction in the ID and MS, and it is thus measured via *two-track* probes. Conversely, $\epsilon\,(X\wedge\neg\mathrm{MS}|\mathrm{CT})$ describes the contribution to the X efficiency from muons reconstructed without a full track in the MS, as measured with CT probes. The MS reconstruction efficiency $\epsilon\,(\mathrm{MS}|\mathrm{CT})$ is also measured with CT probes, while the ID reconstruction efficiency $\epsilon\,(\mathrm{ID}|\mathrm{MS})$ is measured with MS probes. The advantage of this method is that the bias in Eq. (1) stemming from $\epsilon\,(X|\mathrm{CT})$, due to the neglected correlation between the probability of reconstructing a CT muon and that of fulfilling X criterion, is substantially mitigated. The residual bias in Eq. (2) was tested using generator-level information in detector simulation, and found to be about a factor five smaller than that achieved in Ref. [7], which in the $|\eta| > 0.1$ region ranged between 0.1% and 0.7%.

The signal and background contributions in data are extracted via a fit to the $m_{\mathrm{tag-probe}}$ spectrum in the 61–121 GeV range, separately for the samples of all selected probes, and for the samples of matched probes. An example is shown in Figure 6. All SM processes producing an opposite-charge pair of prompt muons are treated as signal, and modelled with a $m_{\mathrm{tag-probe}}$ template obtained using MC simulation. The background contribution stemming from all processes involving non-prompt muons is modelled using the following functional form:

$$f\,(m_{\mathrm{tag-probe}}) = \left(1 - \frac{m_{\mathrm{tag-probe}}}{\Lambda}\right)^{p_1} \cdot \left(\frac{m_{\mathrm{tag-probe}}}{\Lambda}\right)^{p_2}, \tag{3}$$

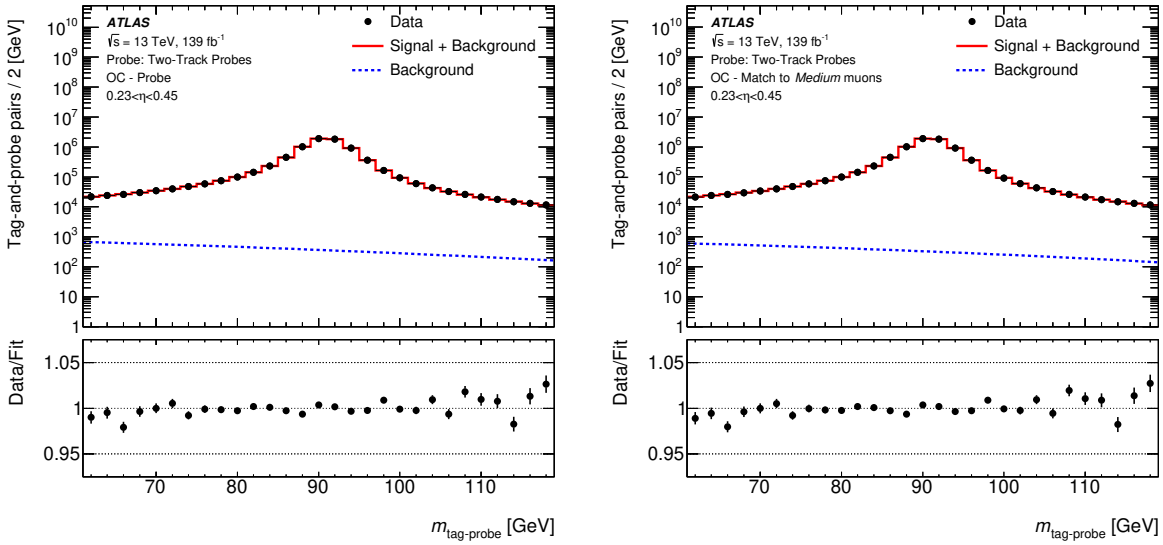


Figure 6: Fit to the $m_{\text{tag-probe}}$ distribution for the selected probes (left), and the probes matched to the *Medium* selection (right), for *two-track* probes with $0.23 < \eta < 0.45$ and opposite-charge (OC) tag-and-probe pairs. The blue line indicates the fitted non-prompt muon background component, while the red line represents the total fitted signal plus the background contribution. The panel beneath shows the data to fit-function ratio for each bin. The error bars indicate the statistical uncertainty.

where the Λ parameter, approximating the energy necessary to produce the dimuon pair [40], is set as 2.5 times the upper boundary of the considered $m_{\text{tag-probe}}$ spectrum. The p_1 and p_2 parameters are instead obtained via a separate fit using a sample of same-charge tag-and-probe pairs, satisfying all the selection criteria except the isolation requirements.

6.2.2 Vertex association efficiencies

Run conditions and ID distortions and misalignments impact the efficiency of the vertex association criteria detailed in Section 5.2. For its measurement, the same strategy used for the reconstruction and identification efficiencies is deployed, with some relevant adjustments. $J/\psi \to \mu\mu$ events are not suited for measuring the muon vertex association efficiencies, due to the sizeable displacement of the J/ψ mesons originating for example from the decay of b-hadrons. Therefore, $Z \to \mu\mu$ decays are exploited down to low muon transverse momentum by selecting probes with $p_{\text{T}} > 3$ GeV which satisfy the *Loose* identification criteria. Further, no requirements on the longitudinal and transverse impact parameters of the probe can be applied. To reduce the consequent increase in background contamination, the tag-and-probe invariant mass region considered is restricted to 86–96 GeV. The tag muon selection is instead identical to the one used for measuring the reconstruction and identification efficiencies, as well as for the template fit method and the efficiency and SF computation.

6.2.3 Isolation efficiencies

Similarly to the measurement of the vertex association efficiencies, $Z \to \mu\mu$ decays with $p_{\text{T}} > 3$ GeV probes are used to measure the muon isolation efficiencies in the full transverse momentum range of

interest. To improve the background rejection at low p_{T}, *Loose* identification criteria and the standard vertex association requirements are additionally applied to the probe. Moreover, the two muons originating from the Z boson decay are required to be separated by $\Delta R_{\mu\mu} > 0.3$, to reject events where the tag muon lies inside the isolation cone of the probe.

The fitting procedure used to extract the background contribution in data is identical to that used in the measurement of the reconstruction and identification efficiencies, but an $m_{\mathrm{tag-probe}}$ interval of 81–101 GeV is instead considered. The non-prompt muon background is obtained by fitting same-charge data with the functional form of Eq. (3). In the efficiency computation, the contribution of $Z \to \mu\mu$ events is separated from that of all other processes producing pairs of oppositely charged prompt muons, as modelled with MC simulation. Restricting the measurement of the isolation efficiencies to a clean and well-defined process such as $Z \to \mu\mu$ does not affect the generality of the results obtained, provided that the most relevant kinematic dependencies of the efficiencies are accounted for in the derived SFs, but simplifies the evaluation of the associated uncertainties.

To ensure applicability to a wide range of physics processes, the measured efficiencies and SFs are studied as a function of the muon p_{T}, η, and angular distance ΔR (jet, μ) from the closest reconstructed jet. Jets are reconstructed from calorimeter topological energy clusters [31] in the region $|\eta| < 4.5$ using the anti-k_t algorithm [41, 42] with radius parameter $R = 0.4$. The jets are required to have $p_{\mathrm{T}} > 20$ GeV after being calibrated [43] and after subtracion of the expected energy contribution from pile-up according to the jet area [34]. In order to suppress jets due to pile-up, jets with $p_{\mathrm{T}} < 120$ GeV and $|\eta| < 2.5$ are required to satisfy the *Medium* working point of the jet vertex tagger [34], which uses information from the tracks associated with the jet.

A dedicated procedure is used to resolve reconstruction ambiguities between probes and jets. When a jet overlaps with a selected probe within ΔR (jet, μ) < 0.4, if the ratio of the probe's p_{T} to the jet's p_{T} (*probe-to-jet* p_{T} ratio) is below 0.5, or if the ratio of the probe's p_{T} to the magnitude of the summed vector p_{T} of all tracks associated with the jet (*probe-to-jet-tracks* p_{T} ratio) is below 0.7, the probe is rejected to suppress bottom and charm hadron decays.

6.2.4 Systematic uncertainties

The main contributions to the systematic uncertainty in the measurement of the reconstruction and identification efficiency SFs using $Z \to \mu\mu$ events are discussed below:

- *T&P method*: possible biases in the tag-and-probe method, such as biases due to different kinematic distributions between reconstructed probes and generated muons or correlations between ID and MS efficiencies, are estimated in simulation by comparing the measured efficiency with the fraction of generator-level muons that are successfully reconstructed. This type of bias is expected to affect data and simulation in a similar way, and therefore to approximately cancel out in the SF computation. Half of the observed difference is nevertheless assigned as the SF uncertainty, in order to conservatively account for possible imperfections of the simulation. The use of *two-track* probes reduces this uncertainty to below approximately 0.1%, with a progressive decrease as p_{T} rises.
- *Probe matching*: the default ΔR-based matching procedure is varied in order to assess an uncertainty in how much a given probe type contributed to a certain type of reconstructed muon candidate. This is done by comparing the nominal fraction of matched probes with the fraction of probe tracks for which muon candidate reconstruction is successful.

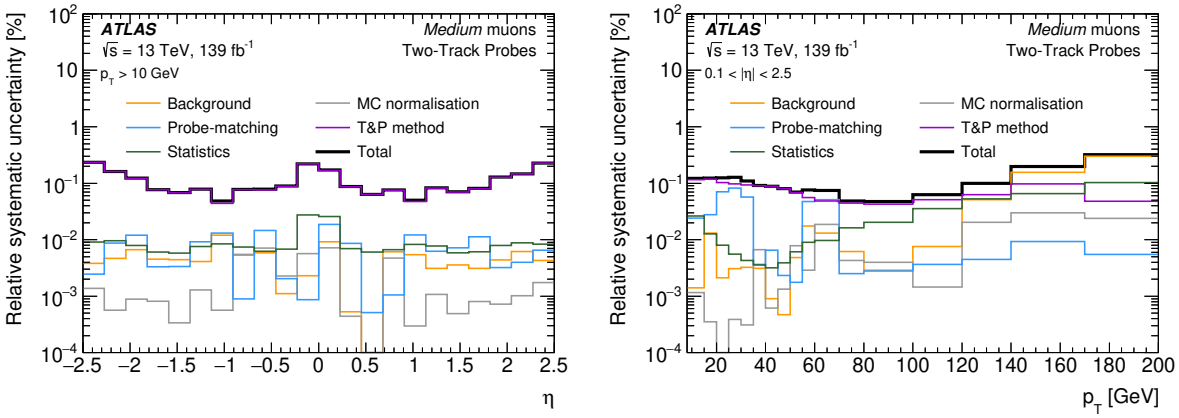


Figure 7: Relative contributions to the systematic uncertainty in the efficiency SFs for *Medium* muons measured with $Z \to \mu\mu$ decays, as a function of η (left) and p_{T} (right) for muons with $p_{\mathrm{T}} > 10$ GeV, and integrated over the other kinematic observables. The uncertainty depicted as *Background* is the sum in quadrature of the *Template shape*, Λ-*SC*, and *Background fit* uncertainties, whereas the *MC normalisation* comprises the *Cross-section* and *Luminosity* uncertainties. The total uncertainty is the sum in quadrature of the individual contributions.

- *Template shape*: the uncertainty in the shape of the template modelling the non-prompt muon background is evaluated by simultaneously varying the p_1 and p_2 parameters in Eq. (3) by their fit uncertainties. The consequent deviation of the SFs from their nominal value is taken as the systematic uncertainty.
- Λ-*SC*: the numerical value of the Λ parameter in Eq. (3) guarantees a well-behaved, smooth function across $m_{\mathrm{tag-probe}}$. Possible effects on the SFs are estimated by varying its value by ±20%.
- *Background fit*: to cover effects associated with the fitting procedure used to extract the contribution of the non-prompt muon background, the change in the SFs obtained when varying the fitted non-prompt muon background by its corresponding fit uncertainty is assigned as a systematic uncertainty.
- *Cross-section*: the uncertainty in the cross-sections of the simulated processes impacts the shape of the signal template by altering its composition, especially in the mass sidebands. Therefore, the normalisation of each MC sample is varied by the measured cross-section's uncertainty [44–46].
- *Luminosity*: the invariant-mass template used to model the non-prompt muon background is corrected for the contamination from same-charge prompt muons, estimated from simulation normalised to the integrated luminosity of the data. The procedure is therefore sensitive to uncertainties in the cross-section of the simulated samples, and in the integrated luminosity of the same-charge data sample. The uncertainty in the combined 2015–2018 integrated luminosity is 1.7% [47], obtained using the LUCID-2 detector [48] for the primary luminosity measurements. To evaluate the impact of this systematic effect, the normalisation factor for the whole simulation is varied accordingly.

Figure 7 shows the relative contributions to the systematic uncertainty in the reconstruction and identification efficiency SFs of *Medium* muons, as a function of η and p_{T}. For muons with $p_{\mathrm{T}} < 100$ GeV, the largest relative contribution stems from the *T&P method* uncertainty, while for muons with $p_{\mathrm{T}} > 150$ GeV the uncertainties in the non-prompt muon background estimates become dominant.

The impact of the muon momentum resolution and scale uncertainties in simulation [7], which can lead to small alterations of the shape of the signal template, was found to be negligible. In the momentum

range considered, the measured SFs do not show a significant dependence on p_{T}. For muon tracks with $p_{\mathrm{T}} > 500$ GeV, the muon reconstruction efficiency is expected to progressively decrease as p_{T} increases, due to a higher likelihood of large energy losses in the calorimeters that can impair the combined muon reconstruction. To account for possible imperfections in the simulation of such extreme energy losses, the full decrease of reconstruction efficiency as a function of p_{T} in simulation is conservatively assigned as a systematic uncertainty.

All the uncertainties detailed above apply also to the measurement of the vertex association and isolation efficiency SFs, with the exception of the *T&P method* and *Probe matching* uncertainties. Conversely, other sources of systematic uncertainty are considered in the measurement of the isolation efficiencies and SFs:

- *Probe PID*: the choice of probe identification working point influences the background contamination level and the signal yield, and therefore is a source of systematic uncertainty. This uncertainty is computed as the difference between the scale factors obtained using *Loose* versus *LowPt* probes, for $p_{\mathrm{T}} < 15$ GeV, or *Loose* versus *Tight* probes, for $p_{\mathrm{T}} > 15$ GeV.
- *Mass window*: a variation of the $m_{\mathrm{tag-probe}}$ range considered in the template fit could lead to different SF values. An uncertainty is assigned as the largest difference observed after changing the nominal $m_{\mathrm{tag-probe}}$ interval of 81–101 GeV for the $\epsilon^{\mathrm{Data}}_{X,Z\to\mu\mu}$ computation to 86–96 GeV and 71–111 GeV.
- *Jet modelling*: to account for possible differences in the modelling of isolation criteria between different MC generators, a dedicated uncertainty is computed as the efficiency difference in $Z \to \mu\mu$ events simulated with Sherpa 2.2.1 and Powheg+Pythia8.
- $\Delta R\,(\mathrm{jet}, \mu)$: as the isolation efficiencies and scale factors are found to depend on the angular distance between the probe and the closest jet, the procedure used to resolve muon–jet reconstruction ambiguities is a source of systematic uncertainty. To account for it, the criteria for the *probe-to-jet* and *probe-to-jet-tracks* p_{T} ratios are independently dropped, and the largest change in the SFs is taken as the uncertainty.

Figures 8 and 9 summarise the uncertainties in the measurement of the vertex association and *Pflow Loose* isolation efficiency SFs, respectively. In the former case, the precision of the measurement is limited by the available statistics. The *Jet modelling* and *Mass window* uncertainties instead show the largest impact on the *Pflow Loose* isolation efficiency SFs.

6.3 Efficiency measurements with $J/\psi \to \mu\mu$ decays

The $J/\psi \to \mu\mu$ events offer a large sample suited to measuring the muon reconstruction and identification efficiencies in the 3–20 GeV transverse momentum range with small statistical uncertainties. To cope with the larger background contamination at very low muon p_{T}, ST probes are deployed. Contrary to CT probes, ST probes are available also for ID tracks with $p_{\mathrm{T}} < 5$ GeV.

Tag-and-probe pairs are selected within the invariant mass window of 2.7–3.5 GeV. The tag muon is required to have $p_{\mathrm{T}} > 6$ GeV, to satisfy the *Tight* muon identification selection, and to have triggered the read-out of the event. In order to avoid low-momentum curved tracks sharing the same trigger region, tag and probe tracks are extrapolated to the MS trigger plane furthest from the interaction point and the extrapolated positions are required to be $\Delta R > 0.2$ apart. Finally, events are selected with $|z_0^T - z_0^P| < 5$ mm, where z_0^T (z_0^P) is the longitudinal impact parameter of the tag (probe) track, to suppress backgrounds. A

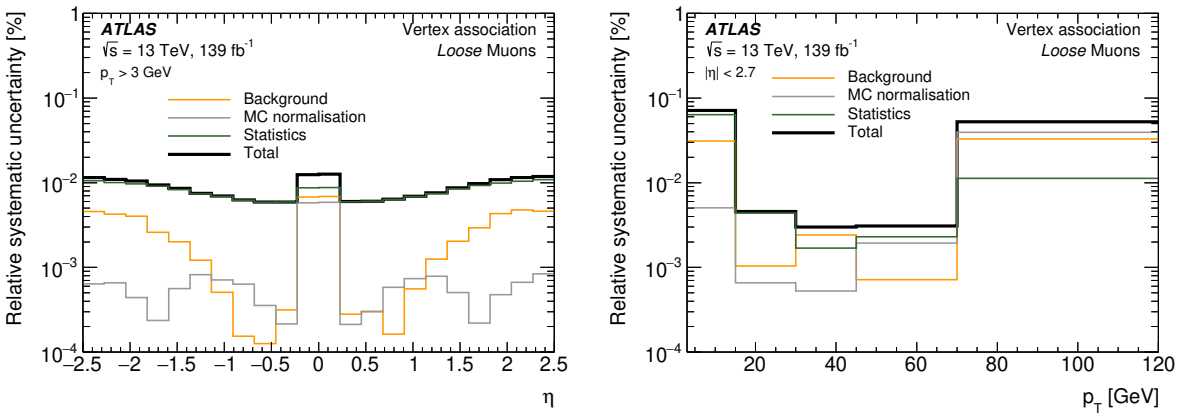


Figure 8: Relative contributions to the systematic uncertainty in the efficiency SFs for the vertex association criteria measured with $Z \to \mu\mu$ decays, as a function of η (left) and p_{T} (right) for muons with $p_{\mathrm{T}} > 3$ GeV, and integrated over the other kinematic observables. The uncertainty depicted as *Background* is the sum in quadrature of the *Template shape*, Λ-*SC*, and *Background fit* uncertainties, whereas the *MC normalisation* comprises the *Cross-section* and *Luminosity* uncertainties. The total uncertainty is the sum in quadrature of the individual contributions.

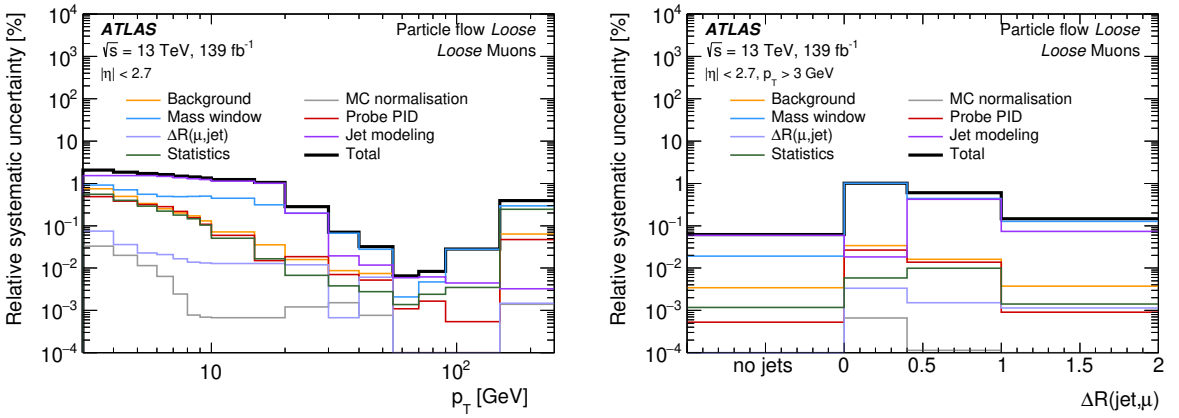


Figure 9: Relative contributions to the systematic uncertainty in the efficiency SFs for the *PflowLoose* isolation criteria, measured with $Z \to \mu\mu$ decays, as a function of p_{T} (left) and ΔR (jet, μ) (right) for muons with $p_{\mathrm{T}} > 3$ GeV, and integrated over the other kinematic observables. The uncertainty depicted as *Background* is the sum in quadrature of the *Template shape*, Λ-*SC*, and *Background fit* uncertainties, whereas the *MC normalisation* comprises the *Cross-section* and *Luminosity* uncertainties. The total uncertainty is the sum in quadrature of the individual contributions.

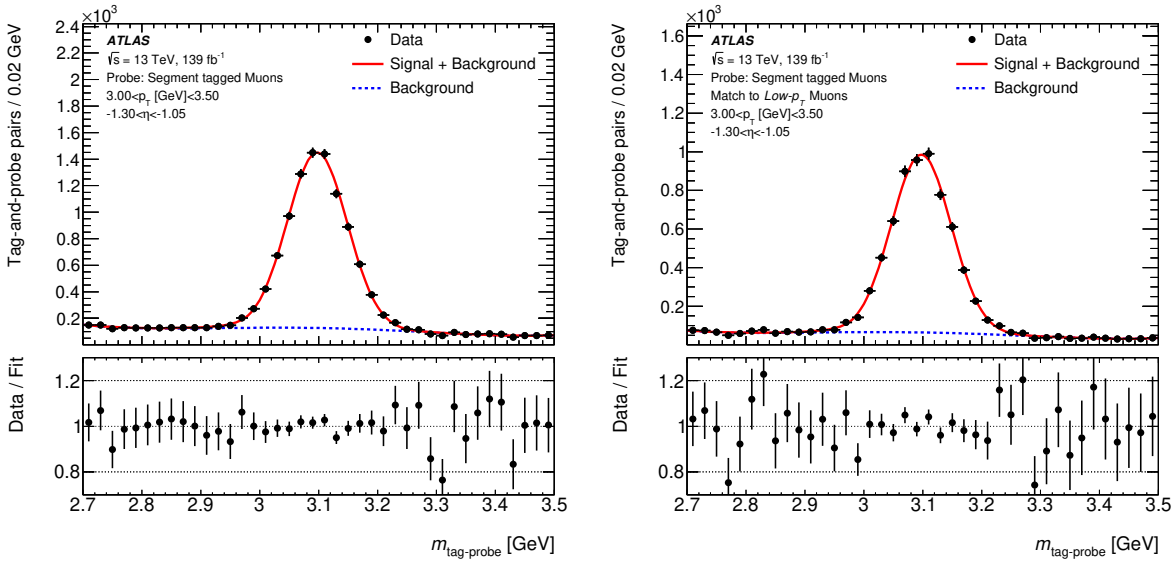


Figure 10: Fit to the $m_{\text{tag-probe}}$ distribution for the selected probes (left), and the probes matched to the *Low-p_T* selection (right), for ST probes with $-1.30 < \eta < -1.05$ and $3.0 < p_{\text{T}} < 3.5$ GeV. The blue line indicates the fitted non-prompt muon background component, while the red line represents the total fitted signal plus the background contribution. The panel beneath shows the data to fit-function ratio for each bin.

probe is required to have $p_{\text{T}} > 3$ GeV, and is considered successfully reconstructed if a selected muon is found within a cone of size $\Delta R = 0.05$ around the probe track.

6.3.1 Reconstruction and identification efficiencies

With the introduction of ST probes, Eq. (1) needs to be modified as follows:

$$\begin{aligned}\epsilon\,(X) &\simeq \epsilon\,(X|\text{ID}) \times \epsilon\,(\text{ID}|\text{MS}) = \frac{\epsilon\,(X|\text{ST})}{\epsilon\,(\text{ST}|X)} \times \epsilon\,(\text{ST}|\text{ID}) \times \epsilon\,(\text{ID}|\text{MS}) \\ &\simeq \epsilon\,(X|\text{ST}) \times \epsilon\,(\text{ST}|\text{ID} \vee \text{CT if } p_{\text{T}} > 5\,\text{GeV}) \times \epsilon\,(\text{ID}|\text{MS})\,.\end{aligned}$$

This approach allows the measurement of the efficiency of the X requirements given an ST probe, $\epsilon\,(X|\text{ST})$, to be separated from that of terms common to all selection criteria, such as the ID efficiency $\epsilon\,(\text{ID}|\text{MS})$ and the ST efficiency $\epsilon\,(\text{ST}|\text{ID} \vee \text{CT if } p_{\text{T}} > 5\,\text{GeV})$ given an ID probe ($p_{\text{T}} < 5$ GeV) or a CT probe ($p_{\text{T}} > 5$ GeV). The $\epsilon\,(\text{ST}|X)$ term accounts for the conditional probability of a successful ST reconstruction given a muon fulfilling the X criterion. In the kinematic regime of interest, it is measured to be compatible with one within its uncertainty.

The muon reconstruction and identification efficiency and the background contamination are measured with a simultaneous maximum-likelihood fit of the tag-and-probe invariant mass in the all-probes and matched-probes samples. An example is shown in Figure 10. A Crystal Ball [49] function is used to model the signal. For the background model, an iterative procedure is deployed, where second-, third- and fourth-order polynomial functions are tested and the one resulting in the fit with the smallest $\chi^2/N_{\text{d.o.f.}}$ is retained.

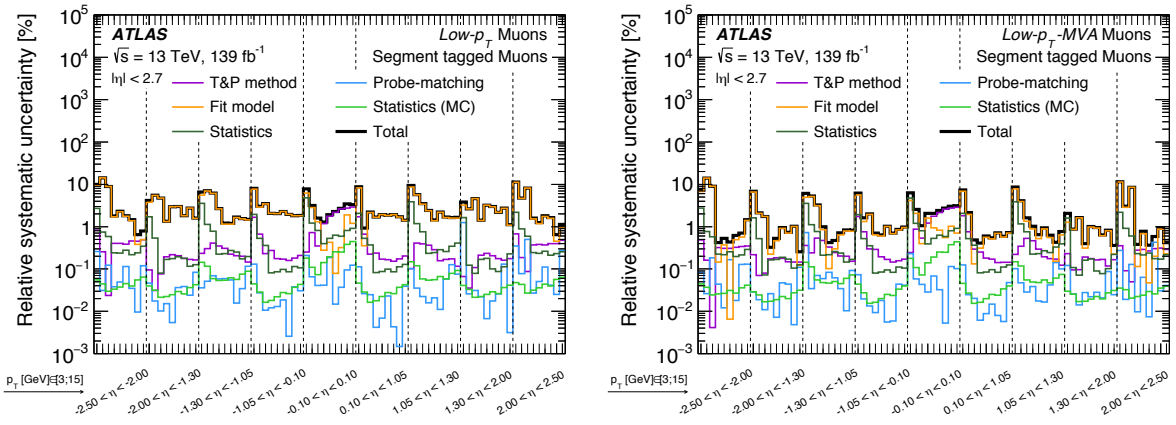


Figure 11: Relative contributions to the systematic uncertainty in the efficiency SFs for muons with $3 < p_{\mathrm{T}} < 15$ GeV fulfilling the cut-based (left) and multivariate (right) *Low-p_T* selection criteria, obtained from $J/\psi \to \mu\mu$ data, as a function of η and p_{T}, and integrated over the other kinematic observables. The resulting values are plotted as distinct measurements in each η bin with p_{T} increasing from 3 to 15 GeV going from left to right. The total uncertainty is the sum in quadrature of all the individual contributions.

6.3.2 Systematic uncertainties

The main contributions to the systematic uncertainty in the measurement of the reconstruction and identification efficiency SFs using $J/\psi \to \mu\mu$ events are shown in Figure 11.

In addition to the *T&P method* and *Probe matching* uncertainties discussed in Section 6.2.4, a *Fit model* systematic uncertainty is assigned to cover the possible biases introduced by the fitting procedure. This uncertainty is estimated by generating pseudo-data mimicking the level of background observed in each invariant mass bin in the data, and injecting it into the corresponding $m_{\mathrm{tag-probe}}$ distribution from J/ψ MC simulation. The latter is then fit using the same procedure as deployed for data, and the difference between the fitted efficiencies and those obtained by counting the fraction of probes in J/ψ MC simulation that satisfy the selection of interest is assigned as the uncertainty. This is found to be the dominant systematic uncertainty in the lowest p_{T} bins, where the background contamination is larger.

6.4 The double-ratio method for the $2.5 < |\eta| < 2.7$ region

The *Loose* and *Medium* selections accept muons within the full MS acceptance, allowing physics analyses to benefit from ME and SiF muons in the $2.5 < |\eta| < 2.7$ region. As the ID coverage is limited to $|\eta| < 2.5$, a tag-and-probe method involving the two independent detectors is not a viable option in this region. A direct measurement of the muon efficiency SF is instead performed, using the same technique as described in Ref. [39], and detailed below.

The SF is calculated from the double ratio:

$$SF = \left[\frac{N_X^{\mathrm{Data}}}{N_X^{\mathrm{MC}}}\right]^{Z\to\mu\mu}_{|\eta|>2.5} \Bigg/ \left[\frac{N_X^{\mathrm{Data}}}{N_X^{\mathrm{MC}}}\right]^{Z\to\mu\mu}_{2.2<|\eta|<2.5}. \tag{4}$$

The numerator of Eq. (4) is the ratio of the number of $Z \to \mu\mu$ candidates in data to the number in MC simulation, where one of the muons (called a *forward* muon hereafter) is identified according to the X

criterion in the $2.5 < |\eta| < 2.7$ region, while the other leg of the Z decay (called a *central* muon) is required to have $|\eta| < 2.4$. The denominator is instead the data-to-MC ratio of $Z \to \mu\mu$ candidates with the *forward* muon lying in the $2.2 < |\eta| < 2.5$ region, and the *central* muon in the $|\eta| < 2.4$ region.

The main assumption behind this method is that the ratio of the number of $Z \to \mu\mu$ events with one *forward* muon to the number of $Z \to \mu\mu$ events with two *central* muons, prior to detector effects, is well modelled in the simulation. In the double ratio, theoretical and experimental uncertainties common to the numerator and the denominator cancel out to first order.

The *central* muon is required to have triggered the event read-out, to fulfil the *Medium* selection, the standard vertex association and the *Tight* isolation criteria, and to have p_{T} greater than 25 GeV. The *forward* muon is selected with p_{T} above 10 GeV and opposite charge to the *central* muon. Their invariant mass must be in the 81–101 GeV interval. The simulation of muons with $|\eta| < 2.5$ is corrected using the standard SF described in the previous section.

To evaluate the systematic uncertainties affecting the measured SF, the pseudorapidity requirement on the *forward* muon used in the denominator is changed to $2.0 < |\eta| < 2.2$, $2.0 < |\eta| < 2.5$, and $|\eta| < 2.2$, and the largest deviation from the nominal SF is taken as the uncertainty. Furthermore, the isolation requirements on the *central* muon are changed to *Loose*, and independently its minimum p_{T} is raised to 35 GeV, computing in either case a symmetric uncertainty as half the deviation from the nominal SF. The uncertainty in the background processes is estimated by subtracting from data the doubled and halved background contributions predicted with MC simulation: half of the largest deviation from the nominal SF is assigned as the uncertainty.The impact of the limited number of MC events is also accounted for. Finally, theoretical uncertainties such as the uncertainty in the knowledge of the true parton distribution functions are evaluated as the variation in the double ratio observed after reweighting the CT10 PDF set used in the $Z \to \mu\mu$ MC simulation to MSTW2008 NLO [50], and after considering the uncertainties associated to the MSTW2008 NLO PDF set.

7 Results

The muon reconstruction, identification, vertex association and isolation efficiencies were measured for tracks with $p_{\mathrm{T}} > 3$ GeV and $|\eta| < 2.7$. In the following paragraphs, the observed performance of the various selection algorithms and the level of agreement between the predicted efficiencies and the corresponding measurements in collision data are discussed.

7.1 Reconstruction and identification efficiencies

Figure 12 shows the muon reconstruction and identification efficiency for *Loose*, *Medium*, and *Tight* muons as measured in $J/\psi \to \mu\mu$ and $Z \to \mu\mu$ events. For muon tracks with p_{T} greater than 10 GeV, the efficiencies and the data/MC agreement are stable for all selection levels. Conversely, the efficiencies drop significantly in the p_{T} region below 5 GeV, as soft muons crossing the calorimeters often do not have enough residual energy to reach the second station of precision MS chambers. The measurements from $J/\psi \to \mu\mu$ and $Z \to \mu\mu$ events agree within uncertainties in the overlap region between 10 and 20 GeV, as visible in Figure 13. For all these reasons, the reconstruction and identification SFs and the corresponding uncertainties are computed in the (η,ϕ) plane for muons with p_{T} above 15 GeV, using $Z \to \mu\mu$ events. In particular, sixteen ϕ bins are used, following the layout of the MS precision chambers. In the SF for

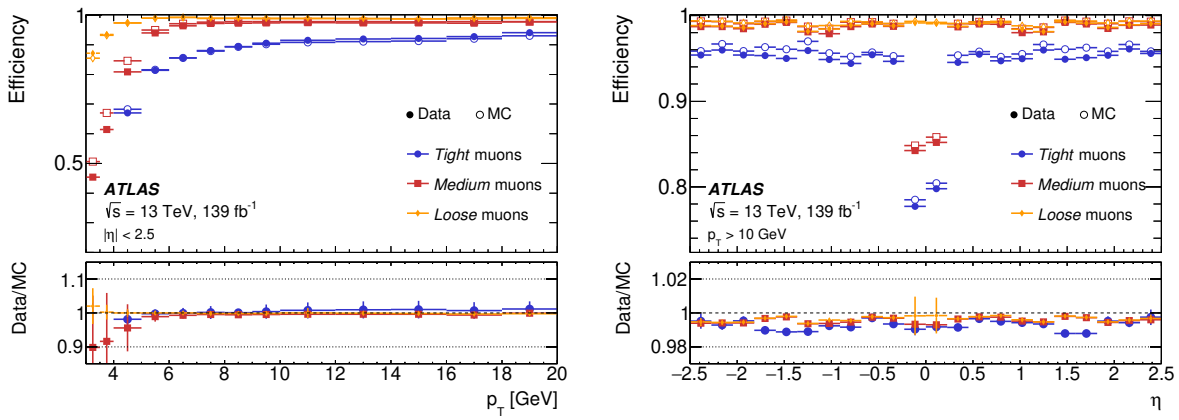


Figure 12: Muon reconstruction and identification efficiencies for the *Loose*, *Medium*, and *Tight* criteria. The left plot shows the efficiencies measured in $J/\psi \to \mu\mu$ events as function of p_{T}. The right plot displays the efficiencies measured in $Z \to \mu\mu$ events as a function of η, for muons with $p_{\mathrm{T}} > 10$ GeV. The predicted efficiencies are depicted as open markers, while filled markers illustrate the result of the measurement in collision data. The statistical uncertainty in the efficiency measurement is smaller than the size of the markers, and thus not displayed. The panel at the bottom shows the ratio of the measured to predicted efficiencies, with statistical and systematic uncertainties.

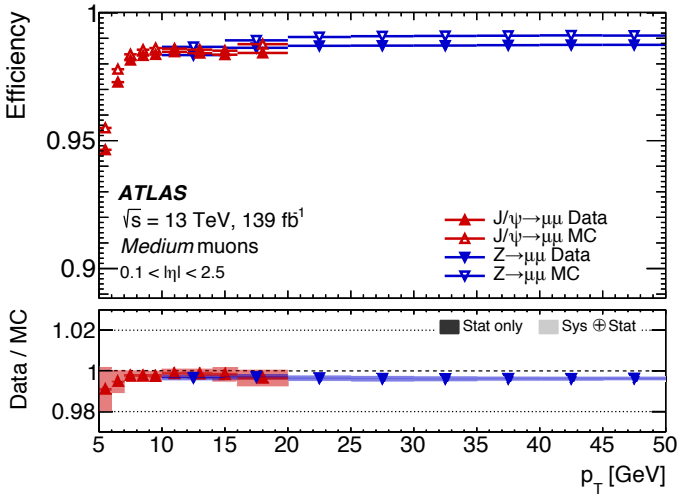


Figure 13: Muon reconstruction and identification efficiencies for the *Medium* criteria measured in $J/\psi \to \mu\mu$ and $Z \to \mu\mu$ events as a function of p_{T} for muons with $0.1 < |\eta| < 2.5$. When not negligible, the statistical uncertainty in the efficiency measurement is indicated by the error bars. The panel at the bottom shows the ratio of the measured to predicted efficiencies, with statistical and systematic uncertainties.

the *High-*p_T selection, the number of η bins and the ϕ bin boundaries are adjusted to reflect the unique characteristics of the WP, which is the most sensitive to the presence or absence of hits in each of the MS stations. In the 3–15 GeV transverse momentum range, the SFs are measured in $J/\psi \to \mu\mu$ events as a function of p_{T} and η.

The *Loose* and *Medium* selections are characterised by very similar efficiency throughout the detector with the exception of the region $|\eta| < 0.1$, where the *Loose* selection accepts CT and ST muons to fill the gap in the MS coverage. The efficiency of the *Loose* and *Medium* criteria exceeds 98% for tracks with

$0.1 < |\eta| < 2.5$. Excellent agreement between detector simulation and the collision data is observed, with differences on average at the level of 0.5%. The efficiency of the *Tight* selection is measured to exceed 95% for tracks with $0.1 < |\eta| < 2.5$, with differences between data and simulation at the 1% level or below.

The efficiencies as measured in $Z \rightarrow \mu\mu$ data events and the corresponding SFs for the *Medium* and *High-*p_T selections are shown as a function of η and ϕ in Figures 14 and 15, respectively. The efficiency of the *High-*p_T selection is significantly lower, as a consequence of the strict requirements on momentum resolution.

For the *Medium* WP, overall agreement between data and simulation across the (η,ϕ) plane is at the level of 0.5%, with about 9% of the measured SFs showing a deviation from unity greater than 1%, and with only two bins with a deviation greater than 5%, both in the $|\eta| < 0.1$ region. The most pronounced local inefficiencies are also observed in the $|\eta| < 1.0$ region, around $\phi = -1.2$ and $\phi = -2.0$, corresponding to the detector support structures that prevent complete coverage by the MS. Further inefficiencies for *Medium* muons are visible in the region $1.0 < |\eta| < 1.3$, characterised by poorly aligned MDT chambers in half of the ϕ sectors of the innermost station. Tracks reconstructed in these chambers are rejected by the *High-*p_T selection, as visible in Figure 15. The efficiency drops localised around $(\eta, \phi) = (-2.5, 0)$ and $(\eta, \phi) = (-2.5, -1)$ were traced to temporary faults in the corresponding CSCs during the 2017 data taking. Similarly, the efficiency drops around $(\eta, \phi) = (-2.5, +2.7)$ and $(\eta, \phi) = (+2.5, -1.5)$ are linked to malfunctioning CSCs during 2018. Finally, the visible efficiency loss in the *High-*p_T selection for tracks with $|\eta| > 2.0$ is associated with the stringent quality requirements imposed on the hits collected in the CSCs, which are particularly important for a robust muon momentum measurement due to the structure of the ATLAS magnetic field. The acceptance gap around $(\eta, \phi) = (-2.0, 0)$ is instead linked to a problematic CSC chamber throughout most of Run 2.

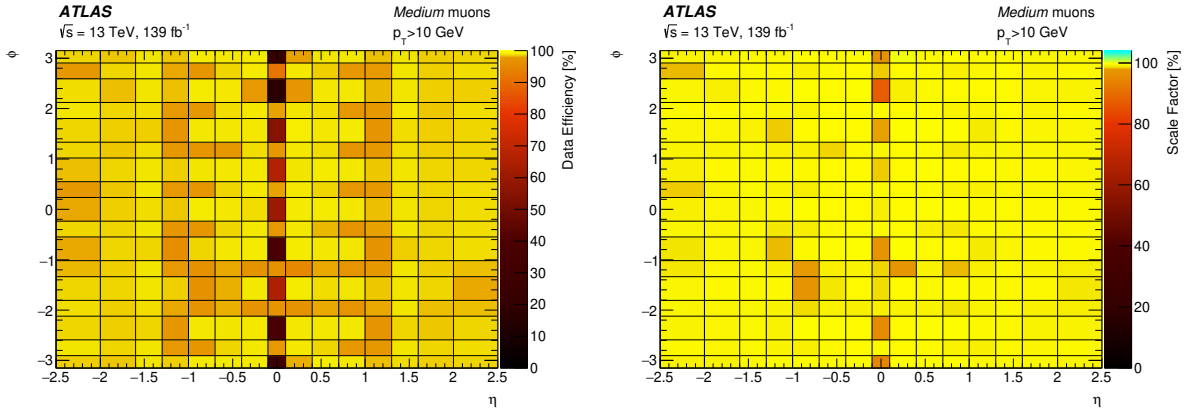


Figure 14: Reconstruction and identification efficiency measured in collision data (left), and the data/MC efficiency scale factor (right) for *Medium* muons as a function of η and ϕ for muons with $p_{\mathrm{T}} > 10$ GeV in $Z \rightarrow \mu\mu$ events.

The efficiencies for the cut-based and multivariate *Low-*p_T selections are shown in Figure 16. For muons with p_{T} greater than 10 GeV, the efficiencies of the two selections are very similar, as expected. Below 10 GeV in muon p_{T} the differences are more marked, with the multivariate selection having a larger efficiency especially in the forward η regions. The multivariate criteria also show, in general, smaller uncertainties in the SFs, due to having more power to reject the non-prompt muon backgrounds contaminating the event sample used for the measurement. Good agreement is found between predicted and observed efficiencies, except in the $|\eta| > 2.0$ region for tracks with p_{T} below 4 GeV, where the differences are larger than 10%. The efficiency drop in collision data is partly associated with the faulty CSCs discussed

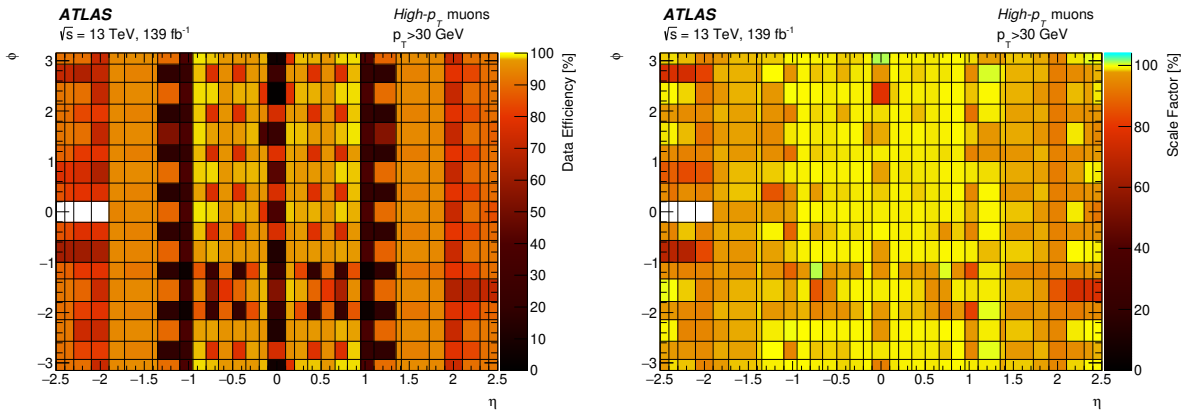


Figure 15: Reconstruction and identification efficiency measured in collision data (left), and the data/MC efficiency scale factor (right) for *High-p_T* muons as a function of η and ϕ for muons with $p_{\mathrm{T}} > 30$ GeV in $Z \to \mu\mu$ events. The white area in the $\eta < -2.0$ and $\phi \simeq 0$ region corresponds to a vetoed problematic CSC.

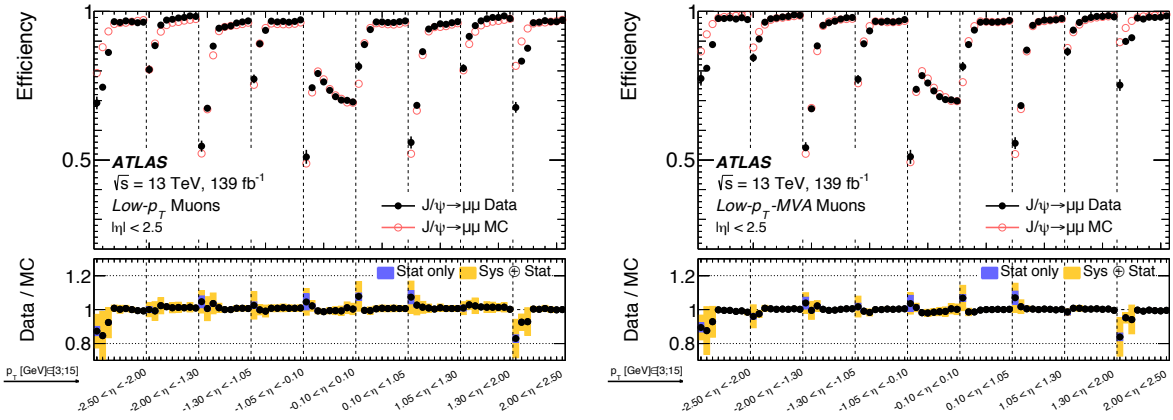


Figure 16: Muon reconstruction and identification efficiency measured in $J/\psi \to \mu\mu$ events for the cut-based (left) and multivariate (right) *Low-p_T* criteria. In the plots, within each η region, the efficiency is measured in nine p_{T} bins (3–3.5, 3.5–4, 4–5, 5–6, 6–7, 7–8, 8–10, 10–12, 12–15 GeV). The resulting values are plotted as distinct measurements in each η bin with p_{T} increasing from 3 to 15 GeV going from left to right. When not negligible, the statistical uncertainty in the efficiency measurement is indicated by the error bars. The panel at the bottom shows the ratio of the measured to predicted efficiencies, with statistical and systematic uncertainties.

previously, which are not modelled by the detector simulation. Furthermore, it stems from an overall lower segment-reconstruction efficiency in the CSC relative to simulation predictions. Since tracks with p_{T} below 4 GeV often have insufficient residual energy to reach the second station of MS precision chambers, efficiency losses in the innermost MS station have a direct impact on the overall reconstruction efficiency.

Figure 17 summarises the efficiencies and SFs for *Medium* muons in the pseudorapidity range of $2.5 < |\eta| < 2.7$ as measured with the double-ratio method described in Section 6.4, and compares them with those obtained with the tag-and-probe technique for $|\eta| < 2.5$. The observed decrease in reconstruction and identification efficiency for $|\eta| > 2.5$ muons stems from the different reconstruction strategy and the more stringent selection criteria applied to tracks in a region where the ID coverage is partial or absent, and reconstruction is mainly based on the MS information. The measured SFs in the forward regions deviate

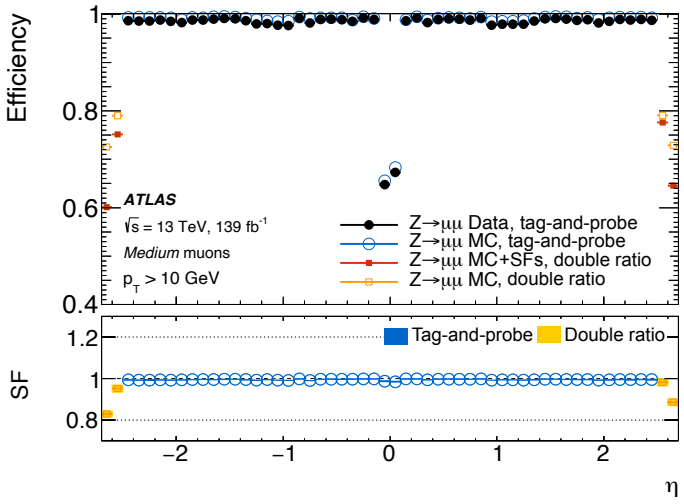


Figure 17: Muon reconstruction and identification efficiencies for the *Medium* criteria measured in $Z \rightarrow \mu\mu$ events as a function of η for muons with $p_{\mathrm{T}} > 10$ GeV. Circular markers show the results obtained using the tag-and-probe method for $|\eta| < 2.5$, while square markers represent the MC simulation efficiencies for $|\eta| > 2.5$ before and after the SFs computed with the double-ratio method are applied. The predicted efficiencies are depicted as open markers, while filled markers illustrate the efficiencies resulting from a direct measurement in collision data ($|\eta| < 2.5$), or from the application of the measured SFs ($|\eta| > 2.5$). The data efficiencies are not shown for $|\eta| > 2.5$ as the double-ratio method allows only the SFs to be measured. The panel at the bottom shows the measured SFs. The statistical and systematic uncertainties are smaller than the size of the markers, and thus not displayed.

significantly from unity, and account for an observed degradation of reconstruction and identification efficiencies in ϕ sectors of the MS with overlapping precision chambers, which is only partially reproduced in simulation. For this reason, the SFs for $|\eta| > 2.5$ muons used in physics analyses are computed as a function of η and ϕ.

7.2 Vertex association efficiencies

Figure 18 shows the muon vertex association efficiency and SFs as a function of the muon p_{T} and $|\eta|$. With the exception of the $|\eta| > 2.5$ region, where tracks fall outside the acceptance of the ID and can therefore only be reconstructed with limited impact parameter resolution, the vertex association efficiency is observed to always exceed 97%, approaching 99% when p_{T} is greater than 20 GeV. In the lowest p_{T} bins, the poorer impact parameter resolution due to multiple interactions with the detector material leads to lower efficiency. Excellent agreement between collision data and detector simulation is found everywhere, with the largest deviation within the ID coverage being of the order of 2% for low-p_{T} tracks near the edge of the TRT detector acceptance around $|\eta|$ of 1.9.

7.3 Isolation efficiencies

Figures 19 and 20 display one-dimensional projections of the measured isolation efficiencies for the *Loose*, *PflowLoose*, and*PLBDTLoose* selections, and the *Tight*, *PflowTight*, and *PLBDTTight* selections,

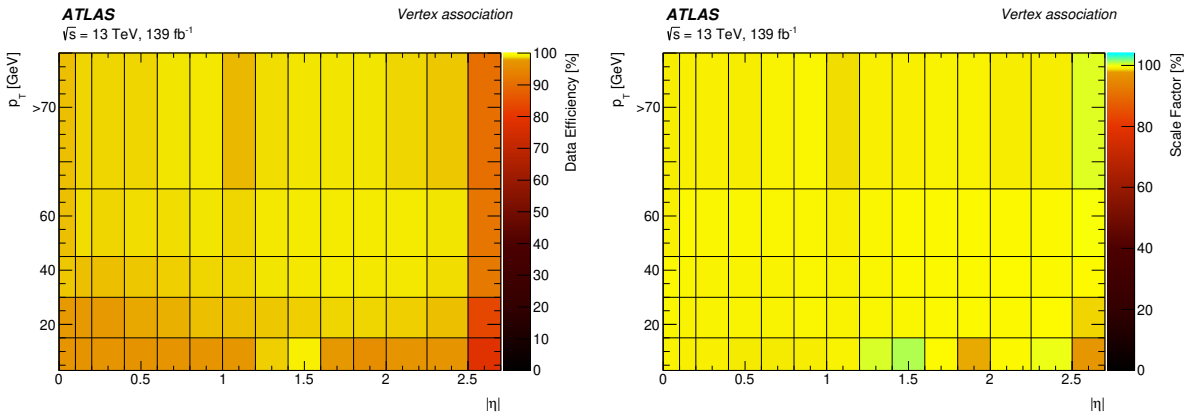


Figure 18: Efficiency of the vertex association criteria measured in data (left), and the data/MC efficiency scale factor (right) as a function of p_{T} and $|\eta|$ for muons with $p_{\mathrm{T}} > 3$ GeV in $Z \to \mu\mu$ events.

respectively, along the muon p_{T} and the angular distance $\Delta R\,(\mathrm{jet}, \mu)$ from the closest jet. Muons well separated from jets and with $p_{\mathrm{T}} > 20$ GeV show SFs very close to unity for all selections, with uncertainties at the per-mille level. At very low transverse momentum and near or within jets, the uncertainties increase to approximately 5%, and are dominated by the *Jet modelling* uncertainty discussed in Section 6.2.4. Reflecting the plots on the right of Figures 19 and 20, the SFs provided to physics analyses are computed as a function of p_{T} in four wide $\Delta R\,(\mathrm{jet}, \mu)$ bins: $\Delta R\,(\mathrm{jet}, \mu) < 0$ corresponding to the case of no jets in the event, $0 < \Delta R\,(\mathrm{jet}, \mu) < 0.4$ corresponding to muons within an anti-k_t jet with $R = 0.4$, $0.4 < \Delta R\,(\mathrm{jet}, \mu) < 1.0$ for muons near an $R = 0.4$ jet or within a large radius jet, and $\Delta R\,(\mathrm{jet}, \mu) > 1.0$ for muons far from any jet.

7.4 Stability throughout data taking

The overall reconstruction and identification efficiency for *Medium* muons fulfilling vertex association and *PflowLoose* isolation criteria is summarised in Figure 21.

In Figure 22 the reconstruction and identification efficiency for *Medium* muons is studied as a function of the delivered integrated luminosity during Run 2, and as a function of the number of simultaneous interactions per bunch crossing. Thanks to the high standards maintained in the operation of the detector and to the robustness of muon reconstruction, no significant drops in efficiency are observed within Run 2. Furthermore, the performance of the reconstruction and identification algorithms remained insensitive to the harshening of the pile-up conditions.

The stability of the vertex association efficiency is illustrated in Figure 23. A progressive but small decrease in the measured efficiency throughout data taking is observed, and corresponds to a gradual deterioration of the impact parameter resolution related to the worse pile-up conditions. Stability is reached during the second half of the 2017 data taking and maintained until the end of Run 2, with some fluctuations at the beginning of 2018 corresponding to collision runs with high pile-up.

Finally, Figure 24 shows the isolation efficiency for the *PflowLoose* criteria throughout Run 2 and as a function of pile-up, for muons with p_{T} greater than 10 GeV. In spite of the very different pile-up conditions

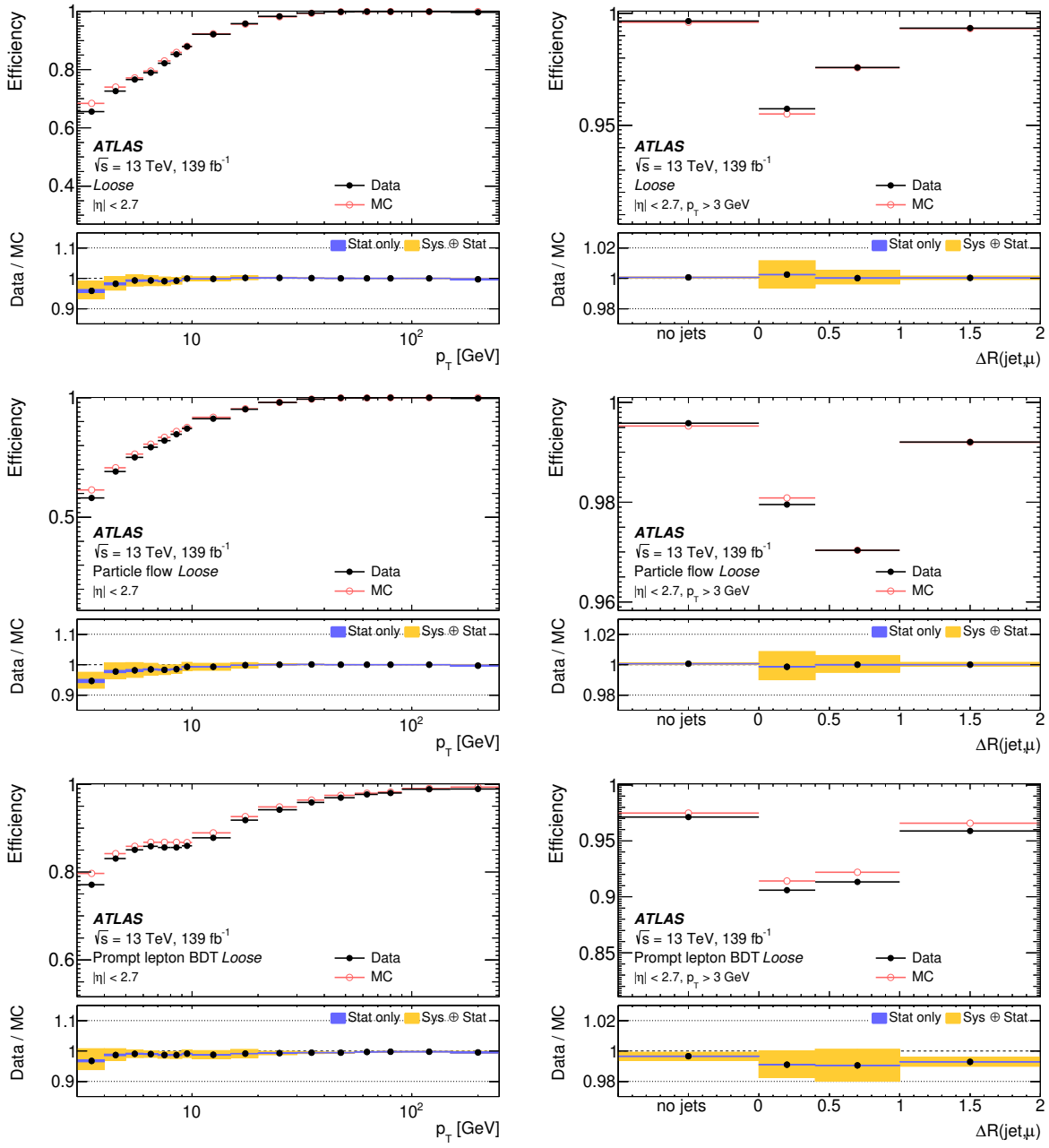


Figure 19: Muon isolation efficiency measured in $Z \to \mu\mu$ events for the *Loose* (top plots), *PflowLoose* (middle plots), and *PLBDTLoose* (bottom plots) criteria, as a function of p_{T} (left plots) and ΔR (jet, μ) (right plots) for muons with $p_{\mathrm{T}} > 3$ GeV. The statistical uncertainty in the efficiency measurement is smaller than the size of the markers, and thus not displayed. The panel at the bottom shows the ratio of the measured to predicted efficiencies, with statistical and systematic uncertainties.

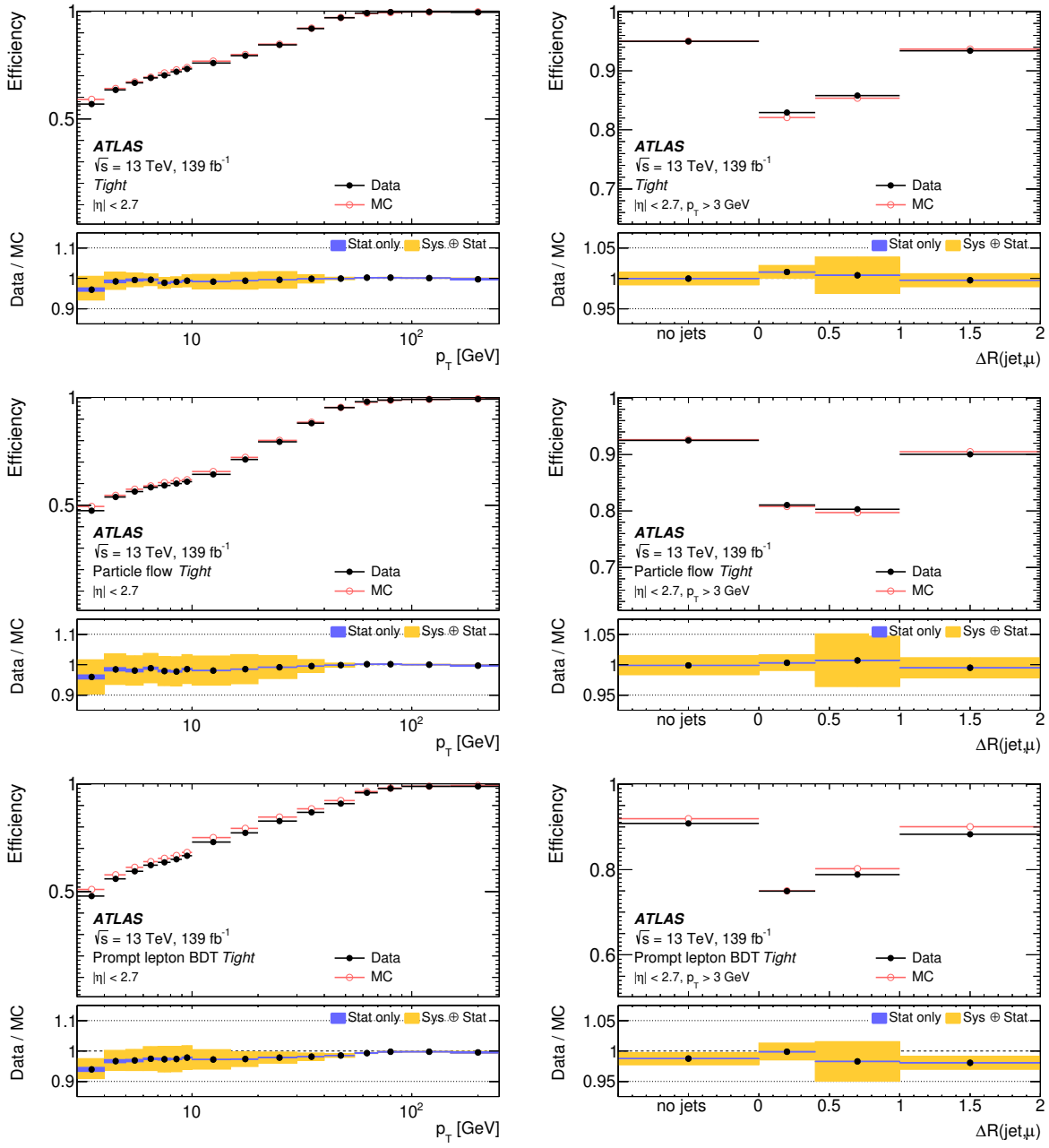


Figure 20: Muon isolation efficiency measured in $Z \to \mu\mu$ events for the *Tight* (top plots), *PflowTight* (middle plots), and *PLBDTTight* (bottom plots) criteria, as a function of p_{T} (left plots) and ΔR (jet, μ) (right plots) for muons with $p_{\mathrm{T}} > 3$ GeV. The statistical uncertainty in the efficiency measurement is smaller than the size of the markers, and thus not displayed. The panel at the bottom shows the ratio of the measured to predicted efficiencies, with statistical and systematic uncertainties.

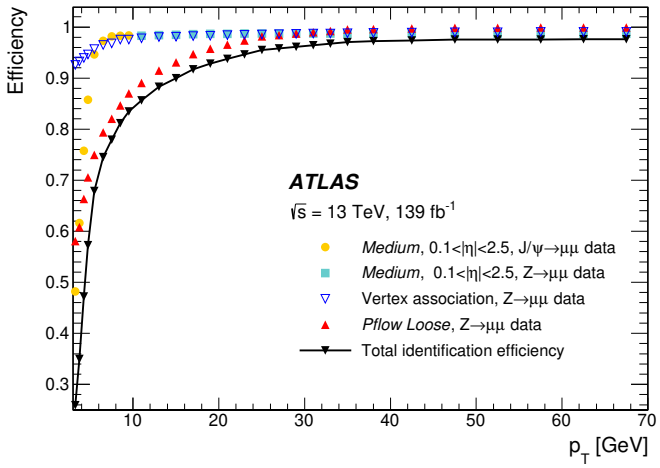


Figure 21: Overall reconstruction and identification efficiency measured in data with $Z \to \mu\mu$ and $J/\psi \to \mu\mu$ decays for prompt muons with $p_{\mathrm{T}} > 3$ GeV. The total identification efficiency for satisfying simultaneously the *Medium*, *PflowLoose* isolation and vertex association criteria (black line) is shown together with its separate components (coloured markers).

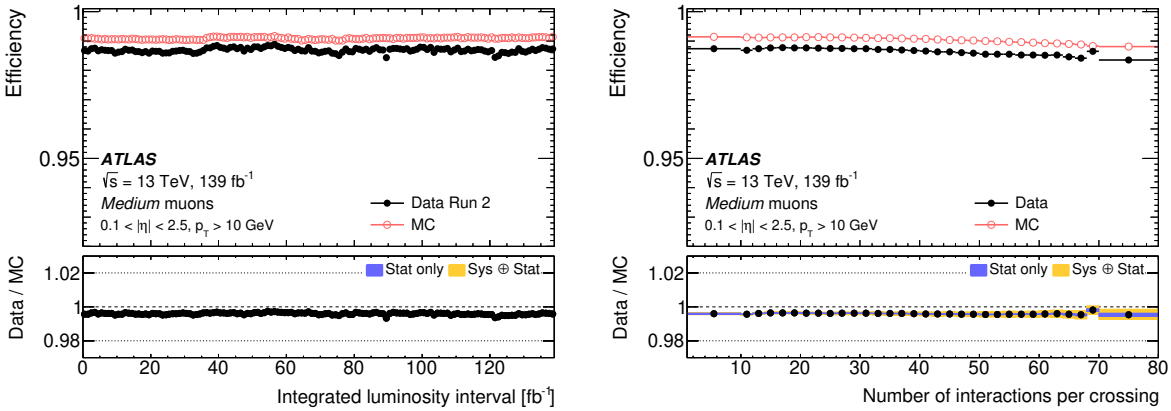


Figure 22: Muon reconstruction and identification efficiency for the *Medium* identification criteria measured in $Z \to \mu\mu$ events as a function of the integrated luminosity interval (left) and the actual number of interactions per bunch crossing (right) for muons with $p_{\mathrm{T}} > 10$ GeV and $0.1 < |\eta| < 2.5$. The statistical uncertainty in the efficiency measurement is smaller than the size of the markers, and thus not displayed. In the left plot each data point corresponds to 1 fb^{-1} of collected data in Run 2. The panel at the bottom shows the ratio of the measured to predicted efficiencies, with statistical and systematic uncertainties.

reached within the various data-taking periods, which have a direct but overall small impact on the efficiency of the isolation selections, agreement between data and simulation remained excellent and stable.

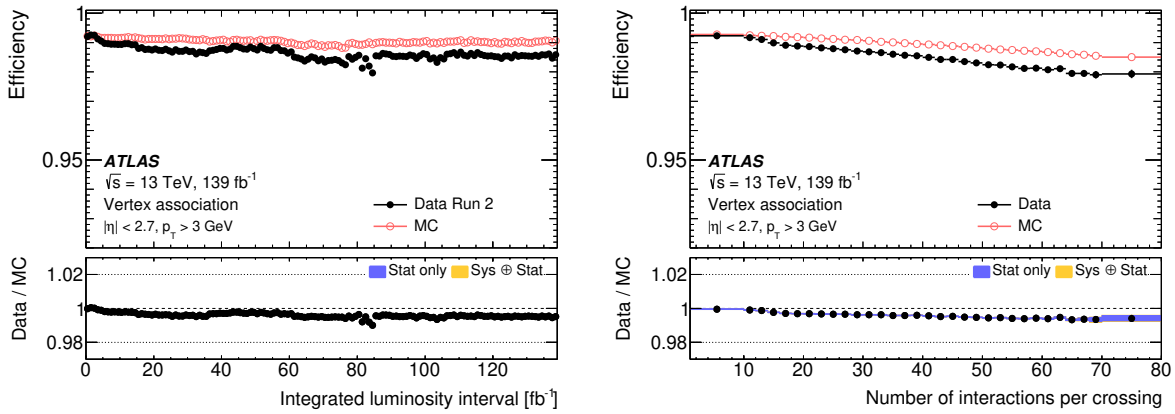


Figure 23: Efficiency for the vertex association criteria measured in $Z \rightarrow \mu\mu$ events as a function of the integrated luminosity interval (left) and the actual number of interactions per bunch crossing (right) for muons with $p_{\mathrm{T}} > 3$ GeV. In the left plot each data point corresponds to 1 fb^{-1} of collected data in Run 2. The statistical uncertainty in the efficiency measurement is smaller than the size of the markers, and thus not displayed. The panel at the bottom shows the ratio of the measured to predicted efficiencies, with statistical and systematic uncertainties. Stable efficiencies are reached during 2017, after 60 fb^{-1} of collected data, and maintained until the end of Run 2, with some fluctuations at the beginning of 2018 corresponding to collision runs with high pile-up.

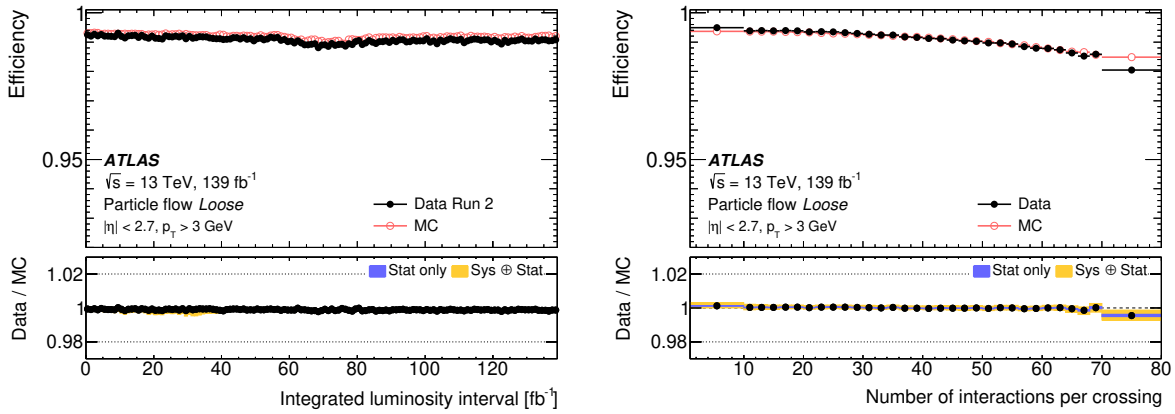


Figure 24: Efficiency for the *PflowLoose* isolation criteria measured in $Z \rightarrow \mu\mu$ events as a function of the integrated luminosity interval (left) and the actual number of interactions per bunch crossing (right) for muons with $p_{\mathrm{T}} > 3$ GeV. In the left plot each data point corresponds to 1 fb^{-1} of collected data in Run 2. The statistical uncertainty in the efficiency measurement is smaller than the size of the markers, and thus not displayed. The panel at the bottom shows the ratio of the measured to predicted efficiencies, with statistical and systematic uncertainties.

8 Conclusions

The ATLAS muon reconstruction, identification, vertex association, and isolation efficiencies have been measured using 139 fb^{-1} of pp collision data at $\sqrt{s}$ = 13 TeV recorded between 2015 and 2018 at the LHC. The measured efficiencies have been compared with the predictions from simulation over the full acceptance of $|\eta| < 2.7$ and over the transverse momentum range of 3 GeV $< p_{\mathrm{T}} <$ 250 GeV, deploying large MC samples of $Z \to \mu\mu$ and $J/\psi \to \mu\mu$ decays consisting of more than 210 and 45 million events, respectively. In the efficiency and SF measurements, the available phase space was subdivided into well-populated regions, choosing a granularity suitable for most of the physics analyses in the ATLAS experiment.

The $Z \to \mu\mu$ sample allows the reconstruction and identification efficiencies to be measured with a precision better than the per-mille level for muons with p_{T} above 10 GeV in most of the detector regions. The $J/\psi \to \mu\mu$ sample extends the measurement down to p_{T} = 3 GeV, with a precision better than 1% in the 5–20 GeV range.

The efficiency of the muon vertex association criteria has been measured with a precision better than 0.2% in the entire transverse momentum range considered, and not exceeding 0.01% for muons with p_{T} above 20 GeV. Excellent agreement with the MC simulation was found. Similarly, the measured efficiencies for the eight isolation working points have been found to agree well with the predictions from simulation, with calibration factors very close to unity and uncertainties at the per-mille level for muons with p_{T} above 20 GeV and well separated from jets.

These results have been used to correct the MC simulation to improve the data–simulation agreement and to minimise the uncertainties in physics analyses.

Acknowledgements

We thank CERN for the very successful operation of the LHC, as well as the support staff from our institutions without whom ATLAS could not be operated efficiently.

We acknowledge the support of ANPCyT, Argentina; YerPhI, Armenia; ARC, Australia; BMWFW and FWF, Austria; ANAS, Azerbaijan; SSTC, Belarus; CNPq and FAPESP, Brazil; NSERC, NRC and CFI, Canada; CERN; ANID, Chile; CAS, MOST and NSFC, China; COLCIENCIAS, Colombia; MSMT CR, MPO CR and VSC CR, Czech Republic; DNRF and DNSRC, Denmark; IN2P3-CNRS and CEA-DRF/IRFU, France; SRNSFG, Georgia; BMBF, HGF and MPG, Germany; GSRT, Greece; RGC and Hong Kong SAR, China; ISF and Benoziyo Center, Israel; INFN, Italy; MEXT and JSPS, Japan; CNRST, Morocco; NWO, Netherlands; RCN, Norway; MNiSW and NCN, Poland; FCT, Portugal; MNE/IFA, Romania; JINR; MES of Russia and NRC KI, Russian Federation; MESTD, Serbia; MSSR, Slovakia; ARRS and MIZŠ, Slovenia; DST/NRF, South Africa; MICINN, Spain; SRC and Wallenberg Foundation, Sweden; SERI, SNSF and Cantons of Bern and Geneva, Switzerland; MOST, Taiwan; TAEK, Turkey; STFC, United Kingdom; DOE and NSF, United States of America. In addition, individual groups and members have received support from BCKDF, CANARIE, Compute Canada, CRC and IVADO, Canada; Beijing Municipal Science & Technology Commission, China; COST, ERC, ERDF, Horizon 2020 and Marie Skłodowska-Curie Actions, European Union; Investissements d'Avenir Labex, Investissements d'Avenir Idex and ANR, France; DFG and AvH Foundation, Germany; Herakleitos, Thales and Aristeia programmes co-financed by EU-ESF and the Greek NSRF, Greece; BSF-NSF and GIF, Israel; La Caixa Banking Foundation, CERCA Programme

Generalitat de Catalunya and PROMETEO and GenT Programmes Generalitat Valenciana, Spain; Göran Gustafssons Stiftelse, Sweden; The Royal Society and Leverhulme Trust, United Kingdom.

The crucial computing support from all WLCG partners is acknowledged gratefully, in particular from CERN, the ATLAS Tier-1 facilities at TRIUMF (Canada), NDGF (Denmark, Norway, Sweden), CC-IN2P3 (France), KIT/GridKA (Germany), INFN-CNAF (Italy), NL-T1 (Netherlands), PIC (Spain), ASGC (Taiwan), RAL (UK) and BNL (USA), the Tier-2 facilities worldwide and large non-WLCG resource providers. Major contributors of computing resources are listed in Ref. [51].

References

[1] ATLAS Collaboration, *The ATLAS Experiment at the CERN Large Hadron Collider*, JINST **3** (2008) S08003.

[2] ATLAS Collaboration, *Measurements of the Higgs boson inclusive and differential fiducial cross sections in the 4ℓ decay channel at $\sqrt{s} = 13$ TeV*, Eur. Phys. J. C **80** (2020) 941, arXiv: 2004.03969 [hep-ex].

[3] ATLAS Collaboration, *Measurement of the CP-violating phase ϕ_s in $B_s^0 \to J/\psi\phi$ decays in ATLAS at 13 TeV*, (2020), arXiv: 2001.07115 [hep-ex].

[4] ATLAS Collaboration, *Searches for electroweak production of supersymmetric particles with compressed mass spectra in $\sqrt{s} = 13$ TeV pp collisions with the ATLAS detector*, Phys. Rev. D **101** (2020) 052005, arXiv: 1911.12606 [hep-ex].

[5] ATLAS Collaboration, *Search for a heavy charged boson in events with a charged lepton and missing transverse momentum from pp collisions at $\sqrt{s} = 13$ TeV with the ATLAS detector*, Phys. Rev. D **100** (2019) 052013, arXiv: 1906.05609 [hep-ex].

[6] ATLAS Collaboration, *ATLAS Muon Spectrometer: Technical Design Report*, ATLAS-TDR-10; CERN-LHCC-97-022, CERN, 1997, URL: https://cds.cern.ch/record/331068.

[7] ATLAS Collaboration, *Muon reconstruction performance of the ATLAS detector in proton–proton collision data at $\sqrt{s} = 13$ TeV*, Eur. Phys. J. C **76** (2016) 292, arXiv: 1603.05598 [hep-ex].

[8] ATLAS Collaboration, *ATLAS Insertable B-Layer Technical Design Report*, ATLAS-TDR-19; CERN-LHCC-2010-013, 2010, URL: https://cds.cern.ch/record/1291633.

[9] B. Abbott et al., *Production and integration of the ATLAS Insertable B-Layer*, JINST **13** (2018) T05008, arXiv: 1803.00844 [physics.ins-det].

[10] ATLAS Collaboration, *Performance of the ATLAS trigger system in 2015*, Eur. Phys. J. C **77** (2017) 317, arXiv: 1611.09661 [hep-ex].

[11] ATLAS Collaboration, *ATLAS data quality operations and performance for 2015–2018 data-taking*, JINST **15** (2020) P04003, arXiv: 1911.04632 [physics.ins-det].

[12] ATLAS Collaboration, *Performance of the ATLAS muon triggers in Run 2*, JINST **15** (2020) P09015, arXiv: 2004.13447 [hep-ex].

[13] S. Alioli, P. Nason, C. Oleari and E. Re, *A general framework for implementing NLO calculations in shower Monte Carlo programs: the POWHEG BOX*, JHEP **06** (2010) 043, arXiv: 1002.2581 [hep-ph].

[14] H.-L. Lai et al., *New parton distributions for collider physics*, Phys. Rev. D **82** (2010) 074024.

[15] T. Sjöstrand et al., *An introduction to PYTHIA 8.2*, Comput. Phys. Commun. **191** (2015) 159, arXiv: 1410.3012 [hep-ph].

[16] J. Pumplin et al., *New Generation of Parton Distributions with Uncertainties from Global QCD Analysis*, JHEP **07** (2002) 012, arXiv: hep-ph/0201195.

[17] ATLAS Collaboration, *Measurement of the Z/γ^* boson transverse momentum distribution in pp collisions at $\sqrt{s} = 7$ TeV with the ATLAS detector*, JHEP **09** (2014) 145, arXiv: 1406.3660 [hep-ex].

[18] ATLAS Collaboration, *Monte Carlo Generators for the Production of a W or Z/γ^* Boson in Association with Jets at ATLAS in Run 2*, ATL-PHYS-PUB-2016-003, 2016, URL: https://cds.cern.ch/record/2120133.

[19] ATLAS Collaboration, *ATLAS Pythia 8 tunes to 7 TeV data*, ATL-PHYS-PUB-2014-021, 2014, URL: https://cds.cern.ch/record/1966419.

[20] P. Golonka and Z. Was, *PHOTOS Monte Carlo: a precision tool for QED corrections in Z and W decays*, Eur. Phys. J. C **45** (2006) 97, arXiv: hep-ph/0506026.

[21] N. Davidson, T. Przedzinski and Z. Was, *PHOTOS Interface in C++: Technical and physics documentation*, Comput. Phys. Commun. **199** (2016) 86, arXiv: 1011.0937 [hep-ph].

[22] R. D. Ball et al., *Parton distributions for the LHC run II*, JHEP **04** (2015) 040, arXiv: 1410.8849 [hep-ph].

[23] R. D. Ball et al., *Parton distributions with LHC data*, Nucl. Phys. B **867** (2013) 244, arXiv: 1207.1303 [hep-ph].

[24] ATLAS Collaboration, *The ATLAS Simulation Infrastructure*, Eur. Phys. J. C **70** (2010) 823, arXiv: 1005.4568 [physics.ins-det].

[25] S. Agostinelli et al., *GEANT4 – a simulation toolkit*, Nucl. Instrum. Meth. A **506** (2003) 250.

[26] ATLAS Collaboration, *The Pythia 8 A3 tune description of ATLAS minimum bias and inelastic measurements incorporating the Donnachie–Landshoff diffractive model*, ATL-PHYS-PUB-2016-017, 2016, URL: https://cds.cern.ch/record/2206965.

[27] T. Cornelissen et al., *Concepts, Design and Implementation of the ATLAS New Tracking (NEWT)*, tech. rep. ATL-SOFT-PUB-2007-007. ATL-COM-SOFT-2007-002, CERN, 2007, URL: https://cds.cern.ch/record/1020106.

[28] ATLAS Collaboration, *Performance of the ATLAS Silicon Pattern Recognition Algorithm in Data and Simulation at $\sqrt{s} = 7$ TeV*, ATLAS-CONF-2010-072, 2010, URL: https://cds.cern.ch/record/1281363.

[29] J. Illingworth and J. Kittler, *A survey of the Hough transform*, Computer Vision, Graphics, and Image Processing **44** (1988) 87, ISSN: 0734-189X, URL: http://www.sciencedirect.com/science/article/pii/S0734189X88800331.

[30] ATLAS Collaboration, *Track Reconstruction Performance of the ATLAS Inner Detector at $\sqrt{s} = 13$ TeV*, ATL-PHYS-PUB-2015-018, 2015, URL: https://cds.cern.ch/record/2037683.

[31] ATLAS Collaboration, *Topological cell clustering in the ATLAS calorimeters and its performance in LHC Run 1*, Eur. Phys. J. C **77** (2017) 490, arXiv: 1603.02934 [hep-ex].

[32] ATLAS Collaboration, *Jet reconstruction and performance using particle flow with the ATLAS Detector*, Eur. Phys. J. C **77** (2017) 466, arXiv: 1703.10485 [hep-ex].

[33] K. Rehermann and B. Tweedie,
Efficient identification of boosted semileptonic top quarks at the LHC, JHEP **03** (2011) 059, arXiv: 1007.2221 [hep-ph].

[34] ATLAS Collaboration, *Performance of pile-up mitigation techniques for jets in pp collisions at $\sqrt{s} = 8$ TeV using the ATLAS detector*, Eur. Phys. J. C **76** (2016) 581, arXiv: 1510.03823 [hep-ex].

[35] ATLAS Collaboration, *Evidence for the associated production of the Higgs boson and a top quark pair with the ATLAS detector*, Phys. Rev. D **97** (2018) 072003, arXiv: 1712.08891 [hep-ex].

[36] ATLAS Collaboration, *Measurement of VH, $H \to b\bar{b}$ production as a function of the vector-boson transverse momentum in 13 TeV pp collisions with the ATLAS detector*, JHEP **05** (2019) 141, arXiv: 1903.04618 [hep-ex].

[37] ATLAS Collaboration,
Evidence for the production of three massive vector bosons with the ATLAS detector, Phys. Lett. B **798** (2019) 134913, arXiv: 1903.10415 [hep-ex].

[38] ATLAS Collaboration,
Optimisation and performance studies of the ATLAS b-tagging algorithms for the 2017-18 LHC run, ATL-PHYS-PUB-2017-013, 2017, URL: https://cds.cern.ch/record/2273281.

[39] ATLAS Collaboration, *Measurement of the muon reconstruction performance of the ATLAS detector using 2011 and 2012 LHC proton–proton collision data*, Eur. Phys. J. C **74** (2014) 3130, arXiv: 1407.3935 [hep-ex].

[40] CDF Collaboration,
Search for new particles decaying into dijets in proton-antiproton collisions at $\sqrt{s} = 1.96$ TeV, Phys. Rev. D **79** (2009) 112002.

[41] M. Cacciari, G. P. Salam and G. Soyez, *The anti-k_t jet clustering algorithm*, JHEP **04** (2008) 063, arXiv: 0802.1189 [hep-ph].

[42] M. Cacciari, G. P. Salam and G. Soyez, *FastJet user manual*, Eur. Phys. J. C **72** (2012) 1896, arXiv: 1111.6097 [hep-ph].

[43] ATLAS Collaboration, *Jet energy scale measurements and their systematic uncertainties in proton–proton collisions at $\sqrt{s} = 13$ TeV with the ATLAS detector*, Phys. Rev. D **96** (2017) 072002, arXiv: 1703.09665 [hep-ex].

[44] ATLAS Collaboration, *Measurements of top-quark pair differential cross-sections in the lepton+jets channel in pp collisions at $\sqrt{s} = 13$ TeV using the ATLAS detector*, JHEP **11** (2017) 191, arXiv: 1708.00727 [hep-ex].

[45] ATLAS Collaboration, *Measurement of the $W^{\pm}Z$ boson pair-production cross section in pp collisions at $\sqrt{s} = 13$ TeV with the ATLAS Detector*, Phys. Lett. B **762** (2016) 1, arXiv: 1606.04017 [hep-ex].

[46] ATLAS Collaboration, *Measurements of the production cross section of a Z boson in association with jets in pp collisions at $\sqrt{s} = 13$ TeV with the ATLAS detector*, Eur. Phys. J. C **77** (2017) 361, arXiv: 1702.05725 [hep-ex].

[47] ATLAS Collaboration,
Luminosity determination in pp collisions at $\sqrt{s} = 13$ TeV using the ATLAS detector at the LHC, ATLAS-CONF-2019-021, 2019, URL: https://cds.cern.ch/record/2677054.

[48] G. Avoni et al., *The new LUCID-2 detector for luminosity measurement and monitoring in ATLAS*, JINST **13** (2018) P07017.

[49] M. Oreglia, *A Study of the Reactions $\psi' \to \gamma\gamma\psi$*, Ph.D. thesis, SLAC-0236, SLAC-236, UMI-81-08973, SLAC-R-0236, SLAC-R-236, 1980.

[50] A. D. Martin, W. J. Stirling, R. S. Thorne and G. Watt, *Parton distributions for the LHC*, Eur. Phys. J. C **63** (2009) 189, arXiv: 0901.0002 [hep-ph].

[51] ATLAS Collaboration, *ATLAS Computing Acknowledgements*, ATL-SOFT-PUB-2020-001, URL: https://cds.cern.ch/record/2717821.

The ATLAS Collaboration

G. Aad[102], B. Abbott[128], D.C. Abbott[103], A. Abed Abud[36], K. Abeling[53], D.K. Abhayasinghe[94], S.H. Abidi[167], O.S. AbouZeid[40], N.L. Abraham[156], H. Abramowicz[161], H. Abreu[160], Y. Abulaiti[6], B.S. Acharya[67a,67b,n], B. Achkar[53], L. Adam[100], C. Adam Bourdarios[5], L. Adamczyk[84a], L. Adamek[167], J. Adelman[121], A. Adiguzel[12c,ac], S. Adorni[54], T. Adye[143], A.A. Affolder[145], Y. Afik[160], C. Agapopoulou[65], M.N. Agaras[38], A. Aggarwal[119], C. Agheorghiesei[27c], J.A. Aguilar-Saavedra[139f,139a,ab], A. Ahmad[36], F. Ahmadov[80], W.S. Ahmed[104], X. Ai[18], G. Aielli[74a,74b], S. Akatsuka[86], M. Akbiyik[100], T.P.A. Åkesson[97], E. Akilli[54], A.V. Akimov[111], K. Al Khoury[65], G.L. Alberghi[23b,23a], J. Albert[176], M.J. Alconada Verzini[161], S. Alderweireldt[36], M. Aleksa[36], I.N. Aleksandrov[80], C. Alexa[27b], T. Alexopoulos[10], A. Alfonsi[120], F. Alfonsi[23b,23a], M. Alhroob[128], B. Ali[141], S. Ali[158], M. Aliev[166], G. Alimonti[69a], C. Allaire[36], B.M.M. Allbrooke[156], B.W. Allen[131], P.P. Allport[21], A. Aloisio[70a,70b], F. Alonso[89], C. Alpigiani[148], E. Alunno Camelia[74a,74b], M. Alvarez Estevez[99], M.G. Alviggi[70a,70b], Y. Amaral Coutinho[81b], A. Ambler[104], L. Ambroz[134], C. Amelung[36], D. Amidei[106], S.P. Amor Dos Santos[139a], S. Amoroso[46], C.S. Amrouche[54], F. An[79], C. Anastopoulos[149], N. Andari[144], T. Andeen[11], J.K. Anders[20], S.Y. Andrean[45a,45b], A. Andreazza[69a,69b], V. Andrei[61a], C.R. Anelli[176], S. Angelidakis[9], A. Angerami[39], A.V. Anisenkov[122b,122a], A. Annovi[72a], C. Antel[54], M.T. Anthony[149], E. Antipov[129], M. Antonelli[51], D.J.A. Antrim[18], F. Anulli[73a], M. Aoki[82], J.A. Aparisi Pozo[174], M.A. Aparo[156], L. Aperio Bella[46], N. Aranzabal[36], V. Araujo Ferraz[81a], R. Araujo Pereira[81b], C. Arcangeletti[51], A.T.H. Arce[49], J-F. Arguin[110], S. Argyropoulos[52], J.-H. Arling[46], A.J. Armbruster[36], O. Arnaez[167], H. Arnold[120], Z.P. Arrubarrena Tame[114], G. Artoni[134], H. Asada[117], K. Asai[126], S. Asai[163], T. Asawatavonvanich[165], N.A. Asbah[59], E.M. Asimakopoulou[172], L. Asquith[156], J. Assahsah[35e], K. Assamagan[29], R. Astalos[28a], R.J. Atkin[33a], M. Atkinson[173], N.B. Atlay[19], H. Atmani[65], P.A. Atmasiddha[106], K. Augsten[141], V.A. Austrup[182], G. Avolio[36], M.K. Ayoub[15a], G. Azuelos[110,aj], D. Babal[28a], H. Bachacou[144], K. Bachas[162], F. Backman[45a,45b], P. Bagnaia[73a,73b], H. Bahrasemani[152], A.J. Bailey[174], V.R. Bailey[173], J.T. Baines[143], C. Bakalis[10], O.K. Baker[183], P.J. Bakker[120], E. Bakos[16], D. Bakshi Gupta[8], S. Balaji[157], R. Balasubramanian[120], E.M. Baldin[122b,122a], P. Balek[180], F. Balli[144], W.K. Balunas[134], J. Balz[100], E. Banas[85], M. Bandieramonte[138], A. Bandyopadhyay[19], Sw. Banerjee[181,i], L. Barak[161], W.M. Barbe[38], E.L. Barberio[105], D. Barberis[55b,55a], M. Barbero[102], G. Barbour[95], T. Barillari[115], M-S. Barisits[36], J. Barkeloo[131], T. Barklow[153], R. Barnea[160], B.M. Barnett[143], R.M. Barnett[18], Z. Barnovska-Blenessy[60a], A. Baroncelli[60a], G. Barone[29], A.J. Barr[134], L. Barranco Navarro[45a,45b], F. Barreiro[99], J. Barreiro Guimarães da Costa[15a], U. Barron[161], S. Barsov[137], F. Bartels[61a], R. Bartoldus[153], G. Bartolini[102], A.E. Barton[90], P. Bartos[28a], A. Basalaev[46], A. Basan[100], A. Bassalat[65,ag], M.J. Basso[167], R.L. Bates[57], S. Batlamous[35f], J.R. Batley[32], B. Batool[151], M. Battaglia[145], M. Bauce[73a,73b], F. Bauer[144,*], P. Bauer[24], H.S. Bawa[31], A. Bayirli[12c], J.B. Beacham[49], T. Beau[135], P.H. Beauchemin[170], F. Becherer[52], P. Bechtle[24], H.C. Beck[53], H.P. Beck[20,p], K. Becker[178], C. Becot[46], A. Beddall[12d], A.J. Beddall[12a], V.A. Bednyakov[80], M. Bedognetti[120], C.P. Bee[155], T.A. Beermann[182], M. Begalli[81b], M. Begel[29], A. Behera[155], J.K. Behr[46], F. Beisiegel[24], M. Belfkir[5], A.S. Bell[95], G. Bella[161], L. Bellagamba[23b], A. Bellerive[34], P. Bellos[9], K. Beloborodov[122b,122a], K. Belotskiy[112], N.L. Belyaev[112], D. Benchekroun[35a], N. Benekos[10], Y. Benhammou[161], D.P. Benjamin[6], M. Benoit[29], J.R. Bensinger[26], S. Bentvelsen[120], L. Beresford[134], M. Beretta[51], D. Berge[19], E. Bergeaas Kuutmann[172], N. Berger[5], B. Bergmann[141], L.J. Bergsten[26], J. Beringer[18], S. Berlendis[7], G. Bernardi[135], C. Bernius[153], F.U. Bernlochner[24], T. Berry[94], P. Berta[100], A. Berthold[48], I.A. Bertram[90], N. Besson[144], S. Bethke[115], A. Betti[42], A.J. Bevan[93], J. Beyer[115], S. Bhatta[155], D.S. Bhattacharya[177], P. Bhattarai[26], V.S. Bhopatkar[6], R.M. Bianchi[138], O. Biebel[114], D. Biedermann[19], R. Bielski[36], K. Bierwagen[100], M. Biglietti[75a], T.R.V. Billoud[141], M. Bindi[53], A. Bingul[12d], C. Bini[73a,73b], S. Biondi[23b,23a], C.J. Birch-sykes[101], M. Birman[180], T. Bisanz[36],

J.P. Biswal[3], D. Biswas[181,i], A. Bitadze[101], C. Bittrich[48], K. Bjørke[133], T. Blazek[28a], I. Bloch[46], C. Blocker[26], A. Blue[57], U. Blumenschein[93], G.J. Bobbink[120], V.S. Bobrovnikov[122b,122a], S.S. Bocchetta[97], D. Bogavac[14], A.G. Bogdanchikov[122b,122a], C. Bohm[45a], V. Boisvert[94], P. Bokan[172,53], T. Bold[84a], A.E. Bolz[61b], M. Bomben[135], M. Bona[93], J.S. Bonilla[131], M. Boonekamp[144], C.D. Booth[94], A.G. Borbély[57], H.M. Borecka-Bielska[91], L.S. Borgna[95], A. Borisov[123], G. Borissov[90], D. Bortoletto[134], D. Boscherini[23b], M. Bosman[14], J.D. Bossio Sola[104], K. Bouaouda[35a], J. Boudreau[138], E.V. Bouhova-Thacker[90], D. Boumediene[38], A. Boveia[127], J. Boyd[36], D. Boye[33c], I.R. Boyko[80], A.J. Bozson[94], J. Bracinik[21], N. Brahimi[60d,60c], G. Brandt[182], O. Brandt[32], F. Braren[46], B. Brau[103], J.E. Brau[131], W.D. Breaden Madden[57], K. Brendlinger[46], R. Brener[160], L. Brenner[36], R. Brenner[172], S. Bressler[180], B. Brickwedde[100], D.L. Briglin[21], D. Britton[57], D. Britzger[115], I. Brock[24], R. Brock[107], G. Brooijmans[39], W.K. Brooks[146d], E. Brost[29], P.A. Bruckman de Renstrom[85], B. Brüers[46], D. Bruncko[28b], A. Bruni[23b], G. Bruni[23b], M. Bruschi[23b], N. Bruscino[73a,73b], L. Bryngemark[153], T. Buanes[17], Q. Buat[155], P. Buchholz[151], A.G. Buckley[57], I.A. Budagov[80], M.K. Bugge[133], O. Bulekov[112], B.A. Bullard[59], T.J. Burch[121], S. Burdin[91], C.D. Burgard[120], A.M. Burger[129], B. Burghgrave[8], J.T.P. Burr[46], C.D. Burton[11], J.C. Burzynski[103], V. Büscher[100], E. Buschmann[53], P.J. Bussey[57], J.M. Butler[25], C.M. Buttar[57], J.M. Butterworth[95], P. Butti[36], W. Buttinger[143], C.J. Buxo Vazquez[107], A. Buzatu[158], A.R. Buzykaev[122b,122a], G. Cabras[23b,23a], S. Cabrera Urbán[174], D. Caforio[56], H. Cai[138], V.M.M. Cairo[153], O. Cakir[4a], N. Calace[36], P. Calafiura[18], G. Calderini[135], P. Calfayan[66], G. Callea[57], L.P. Caloba[81b], A. Caltabiano[74a,74b], S. Calvente Lopez[99], D. Calvet[38], S. Calvet[38], T.P. Calvet[102], M. Calvetti[72a,72b], R. Camacho Toro[135], S. Camarda[36], D. Camarero Munoz[99], P. Camarri[74a,74b], M.T. Camerlingo[75a,75b], D. Cameron[133], C. Camincher[36], S. Campana[36], M. Campanelli[95], A. Camplani[40], V. Canale[70a,70b], A. Canesse[104], M. Cano Bret[78], J. Cantero[129], T. Cao[161], Y. Cao[173], M.D.M. Capeans Garrido[36], M. Capua[41b,41a], R. Cardarelli[74a], F. Cardillo[174], G. Carducci[41b,41a], I. Carli[142], T. Carli[36], G. Carlino[70a], B.T. Carlson[138], E.M. Carlson[176,168a], L. Carminati[69a,69b], R.M.D. Carney[153], S. Caron[119], E. Carquin[146d], S. Carrá[46], G. Carratta[23b,23a], J.W.S. Carter[167], T.M. Carter[50], M.P. Casado[14,f], A.F. Casha[167], E.G. Castiglia[183], F.L. Castillo[174], L. Castillo Garcia[14], V. Castillo Gimenez[174], N.F. Castro[139a,139e], A. Catinaccio[36], J.R. Catmore[133], A. Cattai[36], V. Cavaliere[29], V. Cavasinni[72a,72b], E. Celebi[12b], F. Celli[134], K. Cerny[130], A.S. Cerqueira[81a], A. Cerri[156], L. Cerrito[74a,74b], F. Cerutti[18], A. Cervelli[23b,23a], S.A. Cetin[12b], Z. Chadi[35a], D. Chakraborty[121], J. Chan[181], W.S. Chan[120], W.Y. Chan[91], J.D. Chapman[32], B. Chargeishvili[159b], D.G. Charlton[21], T.P. Charman[93], M. Chatterjee[20], C.C. Chau[34], S. Che[127], S. Chekanov[6], S.V. Chekulaev[168a], G.A. Chelkov[80,ae], B. Chen[79], C. Chen[60a], C.H. Chen[79], H. Chen[15c], H. Chen[29], J. Chen[60a], J. Chen[39], J. Chen[26], S. Chen[136], S.J. Chen[15c], X. Chen[15b], Y. Chen[60a], Y-H. Chen[46], H.C. Cheng[63a], H.J. Cheng[15a], A. Cheplakov[80], E. Cheremushkina[123], R. Cherkaoui El Moursli[35f], E. Cheu[7], K. Cheung[64], T.J.A. Chevalérias[144], L. Chevalier[144], V. Chiarella[51], G. Chiarelli[72a], G. Chiodini[68a], A.S. Chisholm[21], A. Chitan[27b], I. Chiu[163], Y.H. Chiu[176], M.V. Chizhov[80], K. Choi[11], A.R. Chomont[73a,73b], Y. Chou[103], Y.S. Chow[120], L.D. Christopher[33f], M.C. Chu[63a], X. Chu[15a,15d], J. Chudoba[140], J.J. Chwastowski[85], L. Chytka[130], D. Cieri[115], K.M. Ciesla[85], V. Cindro[92], I.A. Cioară[27b], A. Ciocio[18], F. Cirotto[70a,70b], Z.H. Citron[180,j], M. Citterio[69a], D.A. Ciubotaru[27b], B.M. Ciungu[167], A. Clark[54], P.J. Clark[50], S.E. Clawson[101], C. Clement[45a,45b], Y. Coadou[102], M. Cobal[67a,67c], A. Coccaro[55b], J. Cochran[79], R. Coelho Lopes De Sa[103], H. Cohen[161], A.E.C. Coimbra[36], B. Cole[39], A.P. Colijn[120], J. Collot[58], P. Conde Muiño[139a,139h], S.H. Connell[33c], I.A. Connelly[57], S. Constantinescu[27b], F. Conventi[70a,ak], A.M. Cooper-Sarkar[134], F. Cormier[175], K.J.R. Cormier[167], L.D. Corpe[95], M. Corradi[73a,73b], E.E. Corrigan[97], F. Corriveau[104,z], M.J. Costa[174], F. Costanza[5], D. Costanzo[149], G. Cowan[94], J.W. Cowley[32], J. Crane[101], K. Cranmer[125], R.A. Creager[136], S. Crépé-Renaudin[58], F. Crescioli[135], M. Cristinziani[24], V. Croft[170], G. Crosetti[41b,41a], A. Cueto[5], T. Cuhadar Donszelmann[171], H. Cui[15a,15d], A.R. Cukierman[153], W.R. Cunningham[57], S. Czekierda[85], P. Czodrowski[36], M.M. Czurylo[61b], M.J. Da Cunha Sargedas De Sousa[60b], J.V. Da Fonseca Pinto[81b],

C. Da Via[101], W. Dabrowski[84a], F. Dachs[36], T. Dado[47], S. Dahbi[33f], T. Dai[106], C. Dallapiccola[103], M. Dam[40], G. D'amen[29], V. D'Amico[75a,75b], J. Damp[100], J.R. Dandoy[136], M.F. Daneri[30], M. Danninger[152], V. Dao[36], G. Darbo[55b], O. Dartsi[5], A. Dattagupta[131], T. Daubney[46], S. D'Auria[69a,69b], C. David[168b], T. Davidek[142], D.R. Davis[49], I. Dawson[149], K. De[8], R. De Asmundis[70a], M. De Beurs[120], S. De Castro[23b,23a], N. De Groot[119], P. de Jong[120], H. De la Torre[107], A. De Maria[15c], D. De Pedis[73a], A. De Salvo[73a], U. De Sanctis[74a,74b], A. De Santo[156], J.B. De Vivie De Regie[65], D.V. Dedovich[80], A.M. Deiana[42], J. Del Peso[99], Y. Delabat Diaz[46], D. Delgove[65], F. Deliot[144], C.M. Delitzsch[7], M. Della Pietra[70a,70b], D. Della Volpe[54], A. Dell'Acqua[36], L. Dell'Asta[74a,74b], M. Delmastro[5], C. Delporte[65], P.A. Delsart[58], S. Demers[183], M. Demichev[80], G. Demontigny[110], S.P. Denisov[123], L. D'Eramo[121], D. Derendarz[85], J.E. Derkaoui[35e], F. Derue[135], P. Dervan[91], K. Desch[24], K. Dette[167], C. Deutsch[24], M.R. Devesa[30], P.O. Deviveiros[36], F.A. Di Bello[73a,73b], A. Di Ciaccio[74a,74b], L. Di Ciaccio[5], W.K. Di Clemente[136], C. Di Donato[70a,70b], A. Di Girolamo[36], G. Di Gregorio[72a,72b], A. Di Luca[76a,76b], B. Di Micco[75a,75b], R. Di Nardo[75a,75b], K.F. Di Petrillo[59], R. Di Sipio[167], C. Diaconu[102], F.A. Dias[120], T. Dias Do Vale[139a], M.A. Diaz[146a], F.G. Diaz Capriles[24], J. Dickinson[18], M. Didenko[166], E.B. Diehl[106], J. Dietrich[19], S. Díez Cornell[46], C. Diez Pardos[151], A. Dimitrievska[18], W. Ding[15b], J. Dingfelder[24], S.J. Dittmeier[61b], F. Dittus[36], F. Djama[102], T. Djobava[159b], J.I. Djuvsland[17], M.A.B. Do Vale[147], M. Dobre[27b], C. Doglioni[97], J. Dolejsi[142], Z. Dolezal[142], M. Donadelli[81c], B. Dong[60c], J. Donini[38], A. D'onofrio[15c], M. D'Onofrio[91], J. Dopke[143], A. Doria[70a], M.T. Dova[89], A.T. Doyle[57], E. Drechsler[152], E. Dreyer[152], T. Dreyer[53], A.S. Drobac[170], D. Du[60b], T.A. du Pree[120], Y. Duan[60d], F. Dubinin[111], M. Dubovsky[28a], A. Dubreuil[54], E. Duchovni[180], G. Duckeck[114], O.A. Ducu[36,27b], D. Duda[115], A. Dudarev[36], A.C. Dudder[100], E.M. Duffield[18], M. D'uffizi[101], L. Duflot[65], M. Dührssen[36], C. Dülsen[182], M. Dumancic[180], A.E. Dumitriu[27b], M. Dunford[61a], S. Dungs[47], A. Duperrin[102], H. Duran Yildiz[4a], M. Düren[56], A. Durglishvili[159b], D. Duschinger[48], B. Dutta[46], D. Duvnjak[1], G.I. Dyckes[136], M. Dyndal[36], S. Dysch[101], B.S. Dziedzic[85], M.G. Eggleston[49], T. Eifert[8], G. Eigen[17], K. Einsweiler[18], T. Ekelof[172], H. El Jarrari[35f], V. Ellajosyula[172], M. Ellert[172], F. Ellinghaus[182], A.A. Elliot[93], N. Ellis[36], J. Elmsheuser[29], M. Elsing[36], D. Emeliyanov[143], A. Emerman[39], Y. Enari[163], M.B. Epland[49], J. Erdmann[47], A. Ereditato[20], P.A. Erland[85], M. Errenst[182], M. Escalier[65], C. Escobar[174], O. Estrada Pastor[174], E. Etzion[161], G. Evans[139a], H. Evans[66], M.O. Evans[156], A. Ezhilov[137], F. Fabbri[57], L. Fabbri[23b,23a], V. Fabiani[119], G. Facini[178], R.M. Fakhrutdinov[123], S. Falciano[73a], P.J. Falke[24], S. Falke[36], J. Faltova[142], Y. Fang[15a], Y. Fang[15a], G. Fanourakis[44], M. Fanti[69a,69b], M. Faraj[67a,67c], A. Farbin[8], A. Farilla[75a], E.M. Farina[71a,71b], T. Farooque[107], S.M. Farrington[50], P. Farthouat[36], F. Fassi[35f], P. Fassnacht[36], D. Fassouliotis[9], M. Faucci Giannelli[50], W.J. Fawcett[32], L. Fayard[65], O.L. Fedin[137,o], W. Fedorko[175], A. Fehr[20], M. Feickert[173], L. Feligioni[102], A. Fell[149], C. Feng[60b], M. Feng[49], M.J. Fenton[171], A.B. Fenyuk[123], S.W. Ferguson[43], J. Ferrando[46], A. Ferrari[172], P. Ferrari[120], R. Ferrari[71a], D.E. Ferreira de Lima[61b], A. Ferrer[174], D. Ferrere[54], C. Ferretti[106], F. Fiedler[100], A. Filipčič[92], F. Filthaut[119], K.D. Finelli[25], M.C.N. Fiolhais[139a,139c,a], L. Fiorini[174], F. Fischer[114], J. Fischer[100], W.C. Fisher[107], T. Fitschen[21], I. Fleck[151], P. Fleischmann[106], T. Flick[182], B.M. Flierl[114], L. Flores[136], L.R. Flores Castillo[63a], F.M. Follega[76a,76b], N. Fomin[17], J.H. Foo[167], G.T. Forcolin[76a,76b], B.C. Forland[66], A. Formica[144], F.A. Förster[14], A.C. Forti[101], E. Fortin[102], M.G. Foti[134], D. Fournier[65], H. Fox[90], P. Francavilla[72a,72b], S. Francescato[73a,73b], M. Franchini[23b,23a], S. Franchino[61a], D. Francis[36], L. Franco[5], L. Franconi[20], M. Franklin[59], G. Frattari[73a,73b], A.N. Fray[93], P.M. Freeman[21], B. Freund[110], W.S. Freund[81b], E.M. Freundlich[47], D.C. Frizzell[128], D. Froidevaux[36], J.A. Frost[134], M. Fujimoto[126], C. Fukunaga[164], E. Fullana Torregrosa[174], T. Fusayasu[116], J. Fuster[174], A. Gabrielli[23b,23a], A. Gabrielli[36], S. Gadatsch[54], P. Gadow[115], G. Gagliardi[55b,55a], L.G. Gagnon[110], G.E. Gallardo[134], E.J. Gallas[134], B.J. Gallop[143], R. Gamboa Goni[93], K.K. Gan[127], S. Ganguly[180], J. Gao[60a], Y. Gao[50], Y.S. Gao[31,l], F.M. Garay Walls[146a], C. García[174], J.E. García Navarro[174], J.A. García Pascual[15a], C. Garcia-Argos[52], M. Garcia-Sciveres[18], R.W. Gardner[37], N. Garelli[153], S. Gargiulo[52], C.A. Garner[167], V. Garonne[133], S.J. Gasiorowski[148],

P. Gaspar[81b], A. Gaudiello[55b,55a], G. Gaudio[71a], P. Gauzzi[73a,73b], I.L. Gavrilenko[111], A. Gavrilyuk[124], C. Gay[175], G. Gaycken[46], E.N. Gazis[10], A.A. Geanta[27b], C.M. Gee[145], C.N.P. Gee[143], J. Geisen[97], M. Geisen[100], C. Gemme[55b], M.H. Genest[58], C. Geng[106], S. Gentile[73a,73b], S. George[94], T. Geralis[44], L.O. Gerlach[53], P. Gessinger-Befurt[100], G. Gessner[47], M. Ghasemi Bostanabad[176], M. Ghneimat[151], A. Ghosh[65], A. Ghosh[78], B. Giacobbe[23b], S. Giagu[73a,73b], N. Giangiacomi[167], P. Giannetti[72a], A. Giannini[70a,70b], G. Giannini[14], S.M. Gibson[94], M. Gignac[145], D.T. Gil[84b], B.J. Gilbert[39], D. Gillberg[34], G. Gilles[182], N.E.K. Gillwald[46], D.M. Gingrich[3,aj], M.P. Giordani[67a,67c], P.F. Giraud[144], G. Giugliarelli[67a,67c], D. Giugni[69a], F. Giuli[74a,74b], S. Gkaitatzis[162], I. Gkialas[9,g], E.L. Gkougkousis[14], P. Gkountoumis[10], L.K. Gladilin[113], C. Glasman[99], J. Glatzer[14], P.C.F. Glaysher[46], A. Glazov[46], G.R. Gledhill[131], I. Gnesi[41b,b], M. Goblirsch-Kolb[26], D. Godin[110], S. Goldfarb[105], T. Golling[54], D. Golubkov[123], A. Gomes[139a,139b], R. Goncalves Gama[53], R. Gonçalo[139a,139c], G. Gonella[131], L. Gonella[21], A. Gongadze[80], F. Gonnella[21], J.L. Gonski[39], S. González de la Hoz[174], S. Gonzalez Fernandez[14], R. Gonzalez Lopez[91], C. Gonzalez Renteria[18], R. Gonzalez Suarez[172], S. Gonzalez-Sevilla[54], G.R. Gonzalvo Rodriguez[174], L. Goossens[36], N.A. Gorasia[21], P.A. Gorbounov[124], H.A. Gordon[29], B. Gorini[36], E. Gorini[68a,68b], A. Gorišek[92], A.T. Goshaw[49], M.I. Gostkin[80], C.A. Gottardo[119], M. Gouighri[35b], A.G. Goussiou[148], N. Govender[33c], C. Goy[5], I. Grabowska-Bold[84a], E.C. Graham[91], J. Gramling[171], E. Gramstad[133], S. Grancagnolo[19], M. Grandi[156], V. Gratchev[137], P.M. Gravila[27f], F.G. Gravili[68a,68b], C. Gray[57], H.M. Gray[18], C. Grefe[24], K. Gregersen[97], I.M. Gregor[46], P. Grenier[153], K. Grevtsov[46], C. Grieco[14], N.A. Grieser[128], A.A. Grillo[145], K. Grimm[31,k], S. Grinstein[14,v], J.-F. Grivaz[65], S. Groh[100], E. Gross[180], J. Grosse-Knetter[53], Z.J. Grout[95], C. Grud[106], A. Grummer[118], J.C. Grundy[134], L. Guan[106], W. Guan[181], C. Gubbels[175], J. Guenther[77], A. Guerguichon[65], J.G.R. Guerrero Rojas[174], F. Guescini[115], D. Guest[77], R. Gugel[100], A. Guida[46], T. Guillemin[5], S. Guindon[36], J. Guo[60c], W. Guo[106], Y. Guo[60a], Z. Guo[102], R. Gupta[46], S. Gurbuz[12c], G. Gustavino[128], M. Guth[52], P. Gutierrez[128], C. Gutschow[95], C. Guyot[144], C. Gwenlan[134], C.B. Gwilliam[91], E.S. Haaland[133], A. Haas[125], C. Haber[18], H.K. Hadavand[8], A. Hadef[100], M. Haleem[177], J. Haley[129], J.J. Hall[149], G. Halladjian[107], G.D. Hallewell[102], K. Hamano[176], H. Hamdaoui[35f], M. Hamer[24], G.N. Hamity[50], K. Han[60a], L. Han[15c], L. Han[60a], S. Han[18], Y.F. Han[167], K. Hanagaki[82,t], M. Hance[145], D.M. Handl[114], M.D. Hank[37], R. Hankache[135], E. Hansen[97], J.B. Hansen[40], J.D. Hansen[40], M.C. Hansen[24], P.H. Hansen[40], E.C. Hanson[101], K. Hara[169], T. Harenberg[182], S. Harkusha[108], P.F. Harrison[178], N.M. Hartman[153], N.M. Hartmann[114], Y. Hasegawa[150], A. Hasib[50], S. Hassani[144], S. Haug[20], R. Hauser[107], M. Havranek[141], C.M. Hawkes[21], R.J. Hawkings[36], S. Hayashida[117], D. Hayden[107], C. Hayes[106], R.L. Hayes[175], C.P. Hays[134], J.M. Hays[93], H.S. Hayward[91], S.J. Haywood[143], F. He[60a], Y. He[165], M.P. Heath[50], V. Hedberg[97], A.L. Heggelund[133], N.D. Hehir[93], C. Heidegger[52], K.K. Heidegger[52], W.D. Heidorn[79], J. Heilman[34], S. Heim[46], T. Heim[18], B. Heinemann[46,ah], J.G. Heinlein[136], J.J. Heinrich[131], L. Heinrich[36], J. Hejbal[140], L. Helary[46], A. Held[125], S. Hellesund[133], C.M. Helling[145], S. Hellman[45a,45b], C. Helsens[36], R.C.W. Henderson[90], L. Henkelmann[32], A.M. Henriques Correia[36], H. Herde[26], Y. Hernández Jiménez[33f], H. Herr[100], M.G. Herrmann[114], T. Herrmann[48], G. Herten[52], R. Hertenberger[114], L. Hervas[36], G.G. Hesketh[95], N.P. Hessey[168a], H. Hibi[83], S. Higashino[82], E. Higón-Rodriguez[174], K. Hildebrand[37], J.C. Hill[32], K.K. Hill[29], K.H. Hiller[46], S.J. Hillier[21], M. Hils[48], I. Hinchliffe[18], F. Hinterkeuser[24], M. Hirose[132], S. Hirose[169], D. Hirschbuehl[182], B. Hiti[92], O. Hladik[140], J. Hobbs[155], R. Hobincu[27e], N. Hod[180], M.C. Hodgkinson[149], A. Hoecker[36], D. Hohn[52], D. Hohov[65], T. Holm[24], T.R. Holmes[37], M. Holzbock[115], L.B.A.H. Hommels[32], T.M. Hong[138], J.C. Honig[52], A. Hönle[115], B.H. Hooberman[173], W.H. Hopkins[6], Y. Horii[117], P. Horn[48], L.A. Horyn[37], S. Hou[158], A. Hoummada[35a], J. Howarth[57], J. Hoya[89], M. Hrabovsky[130], J. Hrivnac[65], A. Hrynevich[109], T. Hryn'ova[5], P.J. Hsu[64], S.-C. Hsu[148], Q. Hu[39], S. Hu[60c], Y.F. Hu[15a,15d,al], D.P. Huang[95], X. Huang[15c], Y. Huang[60a], Y. Huang[15a], Z. Hubacek[141], F. Hubaut[102], M. Huebner[24], F. Huegging[24], T.B. Huffman[134], M. Huhtinen[36], R. Hulsken[58], R.F.H. Hunter[34], N. Huseynov[80,aa], J. Huston[107], J. Huth[59], R. Hyneman[153],

S. Hyrych[28a], G. Iacobucci[54], G. Iakovidis[29], I. Ibragimov[151], L. Iconomidou-Fayard[65], P. Iengo[36], R. Ignazzi[40], R. Iguchi[163], T. Iizawa[54], Y. Ikegami[82], M. Ikeno[82], N. Ilic[119,167,z], F. Iltzsche[48], H. Imam[35a], G. Introzzi[71a,71b], M. Iodice[75a], K. Iordanidou[168a], V. Ippolito[73a,73b], M.F. Isacson[172], M. Ishino[163], W. Islam[129], C. Issever[19,46], S. Istin[160], J.M. Iturbe Ponce[63a], R. Iuppa[76a,76b], A. Ivina[180], J.M. Izen[43], V. Izzo[70a], P. Jacka[140], P. Jackson[1], R.M. Jacobs[46], B.P. Jaeger[152], V. Jain[2], G. Jäkel[182], K.B. Jakobi[100], K. Jakobs[52], T. Jakoubek[180], J. Jamieson[57], K.W. Janas[84a], R. Jansky[54], M. Janus[53], P.A. Janus[84a], G. Jarlskog[97], A.E. Jaspan[91], N. Javadov[80,aa], T. Javůrek[36], M. Javurkova[103], F. Jeanneau[144], L. Jeanty[131], J. Jejelava[159a], P. Jenni[52,c], N. Jeong[46], S. Jézéquel[5], J. Jia[155], Z. Jia[15c], H. Jiang[79], Y. Jiang[60a], Z. Jiang[153], S. Jiggins[52], F.A. Jimenez Morales[38], J. Jimenez Pena[115], S. Jin[15c], A. Jinaru[27b], O. Jinnouchi[165], P. Johansson[149], K.A. Johns[7], C.A. Johnson[66], E. Jones[178], R.W.L. Jones[90], S.D. Jones[156], T.J. Jones[91], J. Jovicevic[36], X. Ju[18], J.J. Junggeburth[115], A. Juste Rozas[14,v], A. Kaczmarska[85], M. Kado[73a,73b], H. Kagan[127], M. Kagan[153], A. Kahn[39], C. Kahra[100], T. Kaji[179], E. Kajomovitz[160], C.W. Kalderon[29], A. Kaluza[100], M. Kaneda[163], N.J. Kang[145], S. Kang[79], Y. Kano[117], J. Kanzaki[82], L.S. Kaplan[181], D. Kar[33f], K. Karava[134], M.J. Kareem[168b], I. Karkanias[162], S.N. Karpov[80], Z.M. Karpova[80], V. Kartvelishvili[90], A.N. Karyukhin[123], E. Kasimi[162], A. Kastanas[45a,45b], C. Kato[60d], J. Katzy[46], K. Kawade[150], K. Kawagoe[88], T. Kawaguchi[117], T. Kawamoto[144], G. Kawamura[53], E.F. Kay[176], F.I. Kaya[170], S. Kazakos[14], V.F. Kazanin[122b,122a], J.M. Keaveney[33a], R. Keeler[176], J.S. Keller[34], E. Kellermann[97], D. Kelsey[156], J.J. Kempster[21], J. Kendrick[21], K.E. Kennedy[39], O. Kepka[140], S. Kersten[182], B.P. Kerševan[92], S. Ketabchi Haghighat[167], F. Khalil-Zada[13], M. Khandoga[144], A. Khanov[129], A.G. Kharlamov[122b,122a], T. Kharlamova[122b,122a], E.E. Khoda[175], T.J. Khoo[77], G. Khoriauli[177], E. Khramov[80], J. Khubua[159b], S. Kido[83], M. Kiehn[36], E. Kim[165], Y.K. Kim[37], N. Kimura[95], A. Kirchhoff[53], D. Kirchmeier[48], J. Kirk[143], A.E. Kiryunin[115], T. Kishimoto[163], D.P. Kisliuk[167], V. Kitali[46], C. Kitsaki[10], O. Kivernyk[24], T. Klapdor-Kleingrothaus[52], M. Klassen[61a], C. Klein[34], M.H. Klein[106], M. Klein[91], U. Klein[91], K. Kleinknecht[100], P. Klimek[36], A. Klimentov[29], F. Klimpel[36], T. Klingl[24], T. Klioutchnikova[36], F.F. Klitzner[114], P. Kluit[120], S. Kluth[115], E. Kneringer[77], E.B.F.G. Knoops[102], A. Knue[52], D. Kobayashi[88], M. Kobel[48], M. Kocian[153], T. Kodama[163], P. Kodys[142], D.M. Koeck[156], P.T. Koenig[24], T. Koffas[34], N.M. Köhler[36], M. Kolb[144], I. Koletsou[5], T. Komarek[130], T. Kondo[82], K. Köneke[52], A.X.Y. Kong[1], A.C. König[119], T. Kono[126], V. Konstantinides[95], N. Konstantinidis[95], B. Konya[97], R. Kopeliansky[66], S. Koperny[84a], K. Korcyl[85], K. Kordas[162], G. Koren[161], A. Korn[95], I. Korolkov[14], E.V. Korolkova[149], N. Korotkova[113], O. Kortner[115], S. Kortner[115], V.V. Kostyukhin[149,166], A. Kotsokechagia[65], A. Kotwal[49], A. Koulouris[10], A. Kourkoumeli-Charalampidi[71a,71b], C. Kourkoumelis[9], E. Kourlitis[6], V. Kouskoura[29], R. Kowalewski[176], W. Kozanecki[101], A.S. Kozhin[123], V.A. Kramarenko[113], G. Kramberger[92], D. Krasnopevtsev[60a], M.W. Krasny[135], A. Krasznahorkay[36], D. Krauss[115], J.A. Kremer[100], J. Kretzschmar[91], K. Kreul[19], P. Krieger[167], F. Krieter[114], S. Krishnamurthy[103], A. Krishnan[61b], M. Krivos[142], K. Krizka[18], K. Kroeninger[47], H. Kroha[115], J. Kroll[140], J. Kroll[136], K.S. Krowpman[107], U. Kruchonak[80], H. Krüger[24], N. Krumnack[79], M.C. Kruse[49], J.A. Krzysiak[85], A. Kubota[165], O. Kuchinskaia[166], S. Kuday[4b], D. Kuechler[46], J.T. Kuechler[46], S. Kuehn[36], T. Kuhl[46], V. Kukhtin[80], Y. Kulchitsky[108,ad], S. Kuleshov[146b], Y.P. Kulinich[173], M. Kuna[58], A. Kupco[140], T. Kupfer[47], O. Kuprash[52], H. Kurashige[83], L.L. Kurchaninov[168a], Y.A. Kurochkin[108], A. Kurova[112], M.G. Kurth[15a,15d], E.S. Kuwertz[36], M. Kuze[165], A.K. Kvam[148], J. Kvita[130], T. Kwan[104], C. Lacasta[174], F. Lacava[73a,73b], D.P.J. Lack[101], H. Lacker[19], D. Lacour[135], E. Ladygin[80], R. Lafaye[5], B. Laforge[135], T. Lagouri[146c], S. Lai[53], I.K. Lakomiec[84a], J.E. Lambert[128], S. Lammers[66], W. Lampl[7], C. Lampoudis[162], E. Lançon[29], U. Landgraf[52], M.P.J. Landon[93], V.S. Lang[52], J.C. Lange[53], R.J. Langenberg[103], A.J. Lankford[171], F. Lanni[29], K. Lantzsch[24], A. Lanza[71a], A. Lapertosa[55b,55a], J.F. Laporte[144], T. Lari[69a], F. Lasagni Manghi[23b,23a], M. Lassnig[36], V. Latonova[140], T.S. Lau[63a], A. Laudrain[100], A. Laurier[34], M. Lavorgna[70a,70b], S.D. Lawlor[94], M. Lazzaroni[69a,69b], B. Le[101], E. Le Guirriec[102], A. Lebedev[79], M. LeBlanc[7], T. LeCompte[6], F. Ledroit-Guillon[58], A.C.A. Lee[95], C.A. Lee[29], G.R. Lee[17], L. Lee[59],

S.C. Lee[158], S. Lee[79], B. Lefebvre[168a], H.P. Lefebvre[94], M. Lefebvre[176], C. Leggett[18], K. Lehmann[152], N. Lehmann[20], G. Lehmann Miotto[36], W.A. Leight[46], A. Leisos[162,u], M.A.L. Leite[81c], C.E. Leitgeb[114], R. Leitner[142], K.J.C. Leney[42], T. Lenz[24], S. Leone[72a], C. Leonidopoulos[50], A. Leopold[135], C. Leroy[110], R. Les[107], C.G. Lester[32], M. Levchenko[137], J. Levêque[5], D. Levin[106], L.J. Levinson[180], D.J. Lewis[21], B. Li[15b], B. Li[106], C-Q. Li[60c,60d], F. Li[60c], H. Li[60a], H. Li[60b], J. Li[60c], K. Li[148], L. Li[60c], M. Li[15a,15d], Q.Y. Li[60a], S. Li[60d,60c], X. Li[46], Y. Li[46], Z. Li[60b], Z. Li[134], Z. Li[104], Z. Li[91], Z. Liang[15a], M. Liberatore[46], B. Liberti[74a], K. Lie[63c], S. Lim[29], C.Y. Lin[32], K. Lin[107], R.A. Linck[66], R.E. Lindley[7], J.H. Lindon[21], A. Linss[46], A.L. Lionti[54], E. Lipeles[136], A. Lipniacka[17], T.M. Liss[173,ai], A. Lister[175], J.D. Little[8], B. Liu[79], B.X. Liu[152], H.B. Liu[29], J.B. Liu[60a], J.K.K. Liu[37], K. Liu[60d,60c], M. Liu[60a], M.Y. Liu[60a], P. Liu[15a], X. Liu[60a], Y. Liu[46], Y. Liu[15a,15d], Y.L. Liu[106], Y.W. Liu[60a], M. Livan[71a,71b], A. Lleres[58], J. Llorente Merino[152], S.L. Lloyd[93], C.Y. Lo[63b], E.M. Lobodzinska[46], P. Loch[7], S. Loffredo[74a,74b], T. Lohse[19], K. Lohwasser[149], M. Lokajicek[140], J.D. Long[173], R.E. Long[90], I. Longarini[73a,73b], L. Longo[36], I. Lopez Paz[101], A. Lopez Solis[149], J. Lorenz[114], N. Lorenzo Martinez[5], A.M. Lory[114], A. Lösle[52], X. Lou[45a,45b], X. Lou[15a], A. Lounis[65], J. Love[6], P.A. Love[90], J.J. Lozano Bahilo[174], M. Lu[60a], Y.J. Lu[64], H.J. Lubatti[148], C. Luci[73a,73b], F.L. Lucio Alves[15c], A. Lucotte[58], F. Luehring[66], I. Luise[155], L. Luminari[73a], B. Lund-Jensen[154], N.A. Luongo[131], M.S. Lutz[161], D. Lynn[29], H. Lyons[91], R. Lysak[140], E. Lytken[97], F. Lyu[15a], V. Lyubushkin[80], T. Lyubushkina[80], H. Ma[29], L.L. Ma[60b], Y. Ma[95], D.M. Mac Donell[176], G. Maccarrone[51], C.M. Macdonald[149], J.C. MacDonald[149], J. Machado Miguens[136], R. Madar[38], W.F. Mader[48], M. Madugoda Ralalage Don[129], N. Madysa[48], J. Maeda[83], T. Maeno[29], M. Maerker[48], V. Magerl[52], N. Magini[79], J. Magro[67a,67c,q], D.J. Mahon[39], C. Maidantchik[81b], A. Maio[139a,139b,139d], K. Maj[84a], O. Majersky[28a], S. Majewski[131], Y. Makida[82], N. Makovec[65], B. Malaescu[135], Pa. Malecki[85], V.P. Maleev[137], F. Malek[58], D. Malito[41b,41a], U. Mallik[78], C. Malone[32], S. Maltezos[10], S. Malyukov[80], J. Mamuzic[174], G. Mancini[51], J.P. Mandalia[93], I. Mandić[92], L. Manhaes de Andrade Filho[81a], I.M. Maniatis[162], J. Manjarres Ramos[48], K.H. Mankinen[97], A. Mann[114], A. Manousos[77], B. Mansoulie[144], I. Manthos[162], S. Manzoni[120], A. Marantis[162,u], G. Marceca[30], L. Marchese[134], G. Marchiori[135], M. Marcisovsky[140], L. Marcoccia[74a,74b], C. Marcon[97], M. Marjanovic[128], Z. Marshall[18], M.U.F. Martensson[172], S. Marti-Garcia[174], C.B. Martin[127], T.A. Martin[178], V.J. Martin[50], B. Martin dit Latour[17], L. Martinelli[75a,75b], M. Martinez[14,v], P. Martinez Agullo[174], V.I. Martinez Outschoorn[103], S. Martin-Haugh[143], V.S. Martoiu[27b], A.C. Martyniuk[95], A. Marzin[36], S.R. Maschek[115], L. Masetti[100], T. Mashimo[163], R. Mashinistov[111], J. Masik[101], A.L. Maslennikov[122b,122a], L. Massa[23b,23a], P. Massarotti[70a,70b], P. Mastrandrea[72a,72b], A. Mastroberardino[41b,41a], T. Masubuchi[163], D. Matakias[29], A. Matic[114], N. Matsuzawa[163], P. Mättig[24], J. Maurer[27b], B. Maček[92], D.A. Maximov[122b,122a], R. Mazini[158], I. Maznas[162], S.M. Mazza[145], J.P. Mc Gowan[104], S.P. Mc Kee[106], T.G. McCarthy[115], W.P. McCormack[18], E.F. McDonald[105], A.E. McDougall[120], J.A. Mcfayden[18], G. Mchedlidze[159b], M.A. McKay[42], K.D. McLean[176], S.J. McMahon[143], P.C. McNamara[105], C.J. McNicol[178], R.A. McPherson[176,z], Z.A. Meadows[103], S. Meehan[36], T. Megy[38], S. Mehlhase[114], A. Mehta[91], B. Meirose[43], D. Melini[160], B.R. Mellado Garcia[33f], J.D. Mellenthin[53], M. Melo[28a], F. Meloni[46], A. Melzer[24], E.D. Mendes Gouveia[139a,139e], A.M. Mendes Jacques Da Costa[21], H.Y. Meng[167], L. Meng[36], X.T. Meng[106], S. Menke[115], E. Meoni[41b,41a], S. Mergelmeyer[19], S.A.M. Merkt[138], C. Merlassino[134], P. Mermod[54,*], L. Merola[70a,70b], C. Meroni[69a], G. Merz[106], O. Meshkov[113,111], J.K.R. Meshreki[151], J. Metcalfe[6], A.S. Mete[6], C. Meyer[66], J-P. Meyer[144], M. Michetti[19], R.P. Middleton[143], L. Mijović[50], G. Mikenberg[180], M. Mikestikova[140], M. Mikuž[92], H. Mildner[149], A. Milic[167], C.D. Milke[42], D.W. Miller[37], L.S. Miller[34], A. Milov[180], D.A. Milstead[45a,45b], A.A. Minaenko[123], I.A. Minashvili[159b], L. Mince[57], A.I. Mincer[125], B. Mindur[84a], M. Mineev[80], Y. Minegishi[163], Y. Mino[86], L.M. Mir[14], M. Mironova[134], T. Mitani[179], J. Mitrevski[114], V.A. Mitsou[174], M. Mittal[60c], O. Miu[167], A. Miucci[20], P.S. Miyagawa[93], A. Mizukami[82], J.U. Mjörnmark[97], T. Mkrtchyan[61a], M. Mlynarikova[121], T. Moa[45a,45b], S. Mobius[53], K. Mochizuki[110], P. Moder[46], P. Mogg[114], S. Mohapatra[39], R. Moles-Valls[24], K. Mönig[46],

E. Monnier[102], A. Montalbano[152], J. Montejo Berlingen[36], M. Montella[95], F. Monticelli[89], S. Monzani[69a], N. Morange[65], A.L. Moreira De Carvalho[139a], D. Moreno[22a], M. Moreno Llácer[174], C. Moreno Martinez[14], P. Morettini[55b], M. Morgenstern[160], S. Morgenstern[48], D. Mori[152], M. Morii[59], M. Morinaga[179], V. Morisbak[133], A.K. Morley[36], G. Mornacchi[36], A.P. Morris[95], L. Morvaj[36], P. Moschovakos[36], B. Moser[120], M. Mosidze[159b], T. Moskalets[144], P. Moskvitina[119], J. Moss[31,m], E.J.W. Moyse[103], S. Muanza[102], J. Mueller[138], R.S.P. Mueller[114], D. Muenstermann[90], G.A. Mullier[97], D.P. Mungo[69a,69b], J.L. Munoz Martinez[14], F.J. Munoz Sanchez[101], P. Murin[28b], W.J. Murray[178,143], A. Murrone[69a,69b], J.M. Muse[128], M. Muškinja[18], C. Mwewa[33a], A.G. Myagkov[123,ae], A.A. Myers[138], G. Myers[66], J. Myers[131], M. Myska[141], B.P. Nachman[18], O. Nackenhorst[47], A.Nag Nag[48], K. Nagai[134], K. Nagano[82], Y. Nagasaka[62], J.L. Nagle[29], E. Nagy[102], A.M. Nairz[36], Y. Nakahama[117], K. Nakamura[82], T. Nakamura[163], H. Nanjo[132], F. Napolitano[61a], R.F. Naranjo Garcia[46], R. Narayan[42], I. Naryshkin[137], M. Naseri[34], T. Naumann[46], G. Navarro[22a], P.Y. Nechaeva[111], F. Nechansky[46], T.J. Neep[21], A. Negri[71a,71b], M. Negrini[23b], C. Nellist[119], C. Nelson[104], M.E. Nelson[45a,45b], S. Nemecek[140], M. Nessi[36,e], M.S. Neubauer[173], F. Neuhaus[100], M. Neumann[182], R. Newhouse[175], P.R. Newman[21], C.W. Ng[138], Y.S. Ng[19], Y.W.Y. Ng[171], B. Ngair[35f], H.D.N. Nguyen[102], T. Nguyen Manh[110], E. Nibigira[38], R.B. Nickerson[134], R. Nicolaidou[144], D.S. Nielsen[40], J. Nielsen[145], M. Niemeyer[53], N. Nikiforou[11], V. Nikolaenko[123,ae], I. Nikolic-Audit[135], K. Nikolopoulos[21], P. Nilsson[29], H.R. Nindhito[54], A. Nisati[73a], N. Nishu[60c], R. Nisius[115], I. Nitsche[47], T. Nitta[179], T. Nobe[163], D.L. Noel[32], Y. Noguchi[86], I. Nomidis[135], M.A. Nomura[29], M. Nordberg[36], J. Novak[92], T. Novak[92], O. Novgorodova[48], R. Novotny[118], L. Nozka[130], K. Ntekas[171], E. Nurse[95], F.G. Oakham[34,aj], J. Ocariz[135], A. Ochi[83], I. Ochoa[139a], J.P. Ochoa-Ricoux[146a], K. O'Connor[26], S. Odaka[82], S. Oerdek[53], A. Ogrodnik[84a], A. Oh[101], C.C. Ohm[154], H. Oide[165], R. Oishi[163], M.L. Ojeda[167], H. Okawa[169], Y. Okazaki[86], M.W. O'Keefe[91], Y. Okumura[163], A. Olariu[27b], L.F. Oleiro Seabra[139a], S.A. Olivares Pino[146a], D. Oliveira Damazio[29], J.L. Oliver[1], M.J.R. Olsson[171], A. Olszewski[85], J. Olszowska[85], Ö.O. Öncel[24], D.C. O'Neil[152], A.P. O'neill[134], A. Onofre[139a,139e], P.U.E. Onyisi[11], H. Oppen[133], R.G. Oreamuno Madriz[121], M.J. Oreglia[37], G.E. Orellana[89], D. Orestano[75a,75b], N. Orlando[14], R.S. Orr[167], V. O'Shea[57], R. Ospanov[60a], G. Otero y Garzon[30], H. Otono[88], P.S. Ott[61a], G.J. Ottino[18], M. Ouchrif[35e], J. Ouellette[29], F. Ould-Saada[133], A. Ouraou[144,*], Q. Ouyang[15a], M. Owen[57], R.E. Owen[143], V.E. Ozcan[12c], N. Ozturk[8], J. Pacalt[130], H.A. Pacey[32], K. Pachal[49], A. Pacheco Pages[14], C. Padilla Aranda[14], S. Pagan Griso[18], G. Palacino[66], S. Palazzo[50], S. Palestini[36], M. Palka[84b], P. Palni[84a], C.E. Pandini[54], J.G. Panduro Vazquez[94], P. Pani[46], G. Panizzo[67a,67c], L. Paolozzi[54], C. Papadatos[110], K. Papageorgiou[9,g], S. Parajuli[42], A. Paramonov[6], C. Paraskevopoulos[10], D. Paredes Hernandez[63b], S.R. Paredes Saenz[134], B. Parida[180], T.H. Park[167], A.J. Parker[31], M.A. Parker[32], F. Parodi[55b,55a], E.W. Parrish[121], J.A. Parsons[39], U. Parzefall[52], L. Pascual Dominguez[135], V.R. Pascuzzi[18], J.M.P. Pasner[145], F. Pasquali[120], E. Pasqualucci[73a], S. Passaggio[55b], F. Pastore[94], P. Pasuwan[45a,45b], S. Pataraia[100], J.R. Pater[101], A. Pathak[181,i], J. Patton[91], T. Pauly[36], J. Pearkes[153], M. Pedersen[133], L. Pedraza Diaz[119], R. Pedro[139a], T. Peiffer[53], S.V. Peleganchuk[122b,122a], O. Penc[140], C. Peng[63b], H. Peng[60a], B.S. Peralva[81a], M.M. Perego[65], A.P. Pereira Peixoto[139a], L. Pereira Sanchez[45a,45b], D.V. Perepelitsa[29], E. Perez Codina[168a], L. Perini[69a,69b], H. Pernegger[36], S. Perrella[36], A. Perrevoort[120], K. Peters[46], R.F.Y. Peters[101], B.A. Petersen[36], T.C. Petersen[40], E. Petit[102], V. Petousis[141], C. Petridou[162], F. Petrucci[75a,75b], M. Pettee[183], N.E. Pettersson[103], K. Petukhova[142], A. Peyaud[144], R. Pezoa[146d], L. Pezzotti[71a,71b], T. Pham[105], P.W. Phillips[143], M.W. Phipps[173], G. Piacquadio[155], E. Pianori[18], A. Picazio[103], R.H. Pickles[101], R. Piegaia[30], D. Pietreanu[27b], J.E. Pilcher[37], A.D. Pilkington[101], M. Pinamonti[67a,67c], J.L. Pinfold[3], C. Pitman Donaldson[95], M. Pitt[161], L. Pizzimento[74a,74b], A. Pizzini[120], M.-A. Pleier[29], V. Plesanovs[52], V. Pleskot[142], E. Plotnikova[80], P. Podberezko[122b,122a], R. Poettgen[97], R. Poggi[54], L. Poggioli[135], I. Pogrebnyak[107], D. Pohl[24], I. Pokharel[53], G. Polesello[71a], A. Poley[152,168a], A. Policicchio[73a,73b], R. Polifka[142], A. Polini[23b], C.S. Pollard[46], V. Polychronakos[29], D. Ponomarenko[112], L. Pontecorvo[36], S. Popa[27a], G.A. Popeneciu[27d], L. Portales[5], D.M. Portillo Quintero[58], S. Pospisil[141],

K. Potamianos[46], I.N. Potrap[80], C.J. Potter[32], H. Potti[11], T. Poulsen[97], J. Poveda[174], T.D. Powell[149], G. Pownall[46], M.E. Pozo Astigarraga[36], A. Prades Ibanez[174], P. Pralavorio[102], M.M. Prapa[44], S. Prell[79], D. Price[101], M. Primavera[68a], M.L. Proffitt[148], N. Proklova[112], K. Prokofiev[63c], F. Prokoshin[80], S. Protopopescu[29], J. Proudfoot[6], M. Przybycien[84a], D. Pudzha[137], A. Puri[173], P. Puzo[65], D. Pyatiizbyantseva[112], J. Qian[106], Y. Qin[101], A. Quadt[53], M. Queitsch-Maitland[36], G. Rabanal Bolanos[59], M. Racko[28a], F. Ragusa[69a,69b], G. Rahal[98], J.A. Raine[54], S. Rajagopalan[29], A. Ramirez Morales[93], K. Ran[15a,15d], D.F. Rassloff[61a], D.M. Rauch[46], F. Rauscher[114], S. Rave[100], B. Ravina[57], I. Ravinovich[180], J.H. Rawling[101], M. Raymond[36], A.L. Read[133], N.P. Readioff[149], M. Reale[68a,68b], D.M. Rebuzzi[71a,71b], G. Redlinger[29], K. Reeves[43], D. Reikher[161], A. Reiss[100], A. Rej[151], C. Rembser[36], A. Renardi[46], M. Renda[27b], M.B. Rendel[115], A.G. Rennie[57], S. Resconi[69a], E.D. Resseguie[18], S. Rettie[95], B. Reynolds[127], E. Reynolds[21], O.L. Rezanova[122b,122a], P. Reznicek[142], E. Ricci[76a,76b], R. Richter[115], S. Richter[46], E. Richter-Was[84b], M. Ridel[135], P. Rieck[115], O. Rifki[46], M. Rijssenbeek[155], A. Rimoldi[71a,71b], M. Rimoldi[46], L. Rinaldi[23b], T.T. Rinn[173], G. Ripellino[154], I. Riu[14], P. Rivadeneira[46], J.C. Rivera Vergara[176], F. Rizatdinova[129], E. Rizvi[93], C. Rizzi[36], S.H. Robertson[104,z], M. Robin[46], D. Robinson[32], C.M. Robles Gajardo[146d], M. Robles Manzano[100], A. Robson[57], A. Rocchi[74a,74b], C. Roda[72a,72b], S. Rodriguez Bosca[174], A. Rodriguez Rodriguez[52], A.M. Rodríguez Vera[168b], S. Roe[36], J. Roggel[182], O. Røhne[133], R. Röhrig[115], R.A. Rojas[146d], B. Roland[52], C.P.A. Roland[66], J. Roloff[29], A. Romaniouk[112], M. Romano[23b,23a], N. Rompotis[91], M. Ronzani[125], L. Roos[135], S. Rosati[73a], G. Rosin[103], B.J. Rosser[136], E. Rossi[46], E. Rossi[75a,75b], E. Rossi[70a,70b], L.P. Rossi[55b], L. Rossini[46], R. Rosten[14], M. Rotaru[27b], B. Rottler[52], D. Rousseau[65], G. Rovelli[71a,71b], A. Roy[11], D. Roy[33f], A. Rozanov[102], Y. Rozen[160], X. Ruan[33f], T.A. Ruggeri[1], F. Rühr[52], A. Ruiz-Martinez[174], A. Rummler[36], Z. Rurikova[52], N.A. Rusakovich[80], H.L. Russell[104], L. Rustige[38,47], J.P. Rutherfoord[7], E.M. Rüttinger[149], M. Rybar[142], G. Rybkin[65], E.B. Rye[133], A. Ryzhov[123], J.A. Sabater Iglesias[46], P. Sabatini[174], L. Sabetta[73a,73b], S. Sacerdoti[65], H.F-W. Sadrozinski[145], R. Sadykov[80], F. Safai Tehrani[73a], B. Safarzadeh Samani[156], M. Safdari[153], P. Saha[121], S. Saha[104], M. Sahinsoy[115], A. Sahu[182], M. Saimpert[36], M. Saito[163], T. Saito[163], H. Sakamoto[163], D. Salamani[54], G. Salamanna[75a,75b], A. Salnikov[153], J. Salt[174], A. Salvador Salas[14], D. Salvatore[41b,41a], F. Salvatore[156], A. Salvucci[63a], A. Salzburger[36], J. Samarati[36], D. Sammel[52], D. Sampsonidis[162], D. Sampsonidou[60d,60c], J. Sánchez[174], A. Sanchez Pineda[67a,36,67c], H. Sandaker[133], C.O. Sander[46], I.G. Sanderswood[90], M. Sandhoff[182], C. Sandoval[22b], D.P.C. Sankey[143], M. Sannino[55b,55a], Y. Sano[117], A. Sansoni[51], C. Santoni[38], H. Santos[139a,139b], S.N. Santpur[18], A. Santra[174], K.A. Saoucha[149], A. Sapronov[80], J.G. Saraiva[139a,139d], O. Sasaki[82], K. Sato[169], F. Sauerburger[52], E. Sauvan[5], P. Savard[167,aj], R. Sawada[163], C. Sawyer[143], L. Sawyer[96], I. Sayago Galvan[174], C. Sbarra[23b], A. Sbrizzi[67a,67c], T. Scanlon[95], J. Schaarschmidt[148], P. Schacht[115], D. Schaefer[37], L. Schaefer[136], U. Schäfer[100], A.C. Schaffer[65], D. Schaile[114], R.D. Schamberger[155], E. Schanet[114], C. Scharf[19], N. Scharmberg[101], V.A. Schegelsky[137], D. Scheirich[142], F. Schenck[19], M. Schernau[171], C. Schiavi[55b,55a], L.K. Schildgen[24], Z.M. Schillaci[26], E.J. Schioppa[68a,68b], M. Schioppa[41b,41a], K.E. Schleicher[52], S. Schlenker[36], K.R. Schmidt-Sommerfeld[115], K. Schmieden[100], C. Schmitt[100], S. Schmitt[46], L. Schoeffel[144], A. Schoening[61b], P.G. Scholer[52], E. Schopf[134], M. Schott[100], J.F.P. Schouwenberg[119], J. Schovancova[36], S. Schramm[54], F. Schroeder[182], A. Schulte[100], H-C. Schultz-Coulon[61a], M. Schumacher[52], B.A. Schumm[145], Ph. Schune[144], A. Schwartzman[153], T.A. Schwarz[106], Ph. Schwemling[144], R. Schwienhorst[107], A. Sciandra[145], G. Sciolla[26], F. Scuri[72a], F. Scutti[105], L.M. Scyboz[115], C.D. Sebastiani[91], K. Sedlaczek[47], P. Seema[19], S.C. Seidel[118], A. Seiden[145], B.D. Seidlitz[29], T. Seiss[37], C. Seitz[46], J.M. Seixas[81b], G. Sekhniaidze[70a], S.J. Sekula[42], N. Semprini-Cesari[23b,23a], S. Sen[49], C. Serfon[29], L. Serin[65], L. Serkin[67a,67b], M. Sessa[60a], H. Severini[128], S. Sevova[153], F. Sforza[55b,55a], A. Sfyrla[54], E. Shabalina[53], J.D. Shahinian[136], N.W. Shaikh[45a,45b], D. Shaked Renous[180], L.Y. Shan[15a], M. Shapiro[18], A. Sharma[36], A.S. Sharma[1], P.B. Shatalov[124], K. Shaw[156], S.M. Shaw[101], M. Shehade[180], Y. Shen[128], A.D. Sherman[25], P. Sherwood[95], L. Shi[95], C.O. Shimmin[183], Y. Shimogama[179],

M. Shimojima[116], J.D. Shinner[94], I.P.J. Shipsey[134], S. Shirabe[165], M. Shiyakova[80,x], J. Shlomi[180], A. Shmeleva[111], M.J. Shochet[37], J. Shojaii[105], D.R. Shope[154], S. Shrestha[127], E.M. Shrif[33f], M.J. Shroff[176], E. Shulga[180], P. Sicho[140], A.M. Sickles[173], E. Sideras Haddad[33f], O. Sidiropoulou[36], A. Sidoti[23b,23a], F. Siegert[48], Dj. Sijacki[16], M.Jr. Silva[181], M.V. Silva Oliveira[36], S.B. Silverstein[45a], S. Simion[65], R. Simoniello[100], C.J. Simpson-allsop[21], S. Simsek[12b], P. Sinervo[167], V. Sinetckii[113], S. Singh[152], S. Sinha[33f], M. Sioli[23b,23a], I. Siral[131], S.Yu. Sivoklokov[113], J. Sjölin[45a,45b], A. Skaf[53], E. Skorda[97], P. Skubic[128], M. Slawinska[85], K. Sliwa[170], V. Smakhtin[180], B.H. Smart[143], J. Smiesko[28b], N. Smirnov[112], S.Yu. Smirnov[112], Y. Smirnov[112], L.N. Smirnova[113,r], O. Smirnova[97], E.A. Smith[37], H.A. Smith[134], M. Smizanska[90], K. Smolek[141], A. Smykiewicz[85], A.A. Snesarev[111], H.L. Snoek[120], I.M. Snyder[131], S. Snyder[29], R. Sobie[176,z], A. Soffer[161], A. Søgaard[50], F. Sohns[53], C.A. Solans Sanchez[36], E.Yu. Soldatov[112], U. Soldevila[174], A.A. Solodkov[123], A. Soloshenko[80], O.V. Solovyanov[123], V. Solovyev[137], P. Sommer[149], H. Son[170], A. Sonay[14], W. Song[143], W.Y. Song[168b], A. Sopczak[141], A.L. Sopio[95], F. Sopkova[28b], S. Sottocornola[71a,71b], R. Soualah[67a,67c], A.M. Soukharev[122b,122a], D. South[46], S. Spagnolo[68a,68b], M. Spalla[115], M. Spangenberg[178], F. Spanò[94], D. Sperlich[52], T.M. Spieker[61a], G. Spigo[36], M. Spina[156], D.P. Spiteri[57], M. Spousta[142], A. Stabile[69a,69b], B.L. Stamas[121], R. Stamen[61a], M. Stamenkovic[120], A. Stampekis[21], E. Stanecka[85], B. Stanislaus[134], M.M. Stanitzki[46], M. Stankaityte[134], B. Stapf[120], E.A. Starchenko[123], G.H. Stark[145], J. Stark[58], P. Staroba[140], P. Starovoitov[61a], S. Stärz[104], R. Staszewski[85], G. Stavropoulos[44], M. Stegler[46], P. Steinberg[29], A.L. Steinhebel[131], B. Stelzer[152,168a], H.J. Stelzer[138], O. Stelzer-Chilton[168a], H. Stenzel[56], T.J. Stevenson[156], G.A. Stewart[36], M.C. Stockton[36], G. Stoicea[27b], M. Stolarski[139a], S. Stonjek[115], A. Straessner[48], J. Strandberg[154], S. Strandberg[45a,45b], M. Strauss[128], T. Strebler[102], P. Strizenec[28b], R. Ströhmer[177], D.M. Strom[131], R. Stroynowski[42], A. Strubig[45a,45b], S.A. Stucci[29], B. Stugu[17], J. Stupak[128], N.A. Styles[46], D. Su[153], W. Su[60d,148,60c], X. Su[60a], N.B. Suarez[138], V.V. Sulin[111], M.J. Sullivan[91], D.M.S. Sultan[54], S. Sultansoy[4c], T. Sumida[86], S. Sun[106], X. Sun[101], C.J.E. Suster[157], M.R. Sutton[156], S. Suzuki[82], M. Svatos[140], M. Swiatlowski[168a], S.P. Swift[2], T. Swirski[177], A. Sydorenko[100], I. Sykora[28a], M. Sykora[142], T. Sykora[142], D. Ta[100], K. Tackmann[46,w], J. Taenzer[161], A. Taffard[171], R. Tafirout[168a], E. Tagiev[123], R.H.M. Taibah[135], R. Takashima[87], K. Takeda[83], T. Takeshita[150], E.P. Takeva[50], Y. Takubo[82], M. Talby[102], A.A. Talyshev[122b,122a], K.C. Tam[63b], N.M. Tamir[161], J. Tanaka[163], R. Tanaka[65], S. Tapia Araya[173], S. Tapprogge[100], A. Tarek Abouelfadl Mohamed[107], S. Tarem[160], K. Tariq[60b], G. Tarna[27b,d], G.F. Tartarelli[69a], P. Tas[142], M. Tasevsky[140], E. Tassi[41b,41a], G. Tateno[163], A. Tavares Delgado[139a], Y. Tayalati[35f], A.J. Taylor[50], G.N. Taylor[105], W. Taylor[168b], H. Teagle[91], A.S. Tee[90], R. Teixeira De Lima[153], P. Teixeira-Dias[94], H. Ten Kate[36], J.J. Teoh[120], K. Terashi[163], J. Terron[99], S. Terzo[14], M. Testa[51], R.J. Teuscher[167,z], N. Themistokleous[50], T. Theveneaux-Pelzer[19], D.W. Thomas[94], J.P. Thomas[21], E.A. Thompson[46], P.D. Thompson[21], E. Thomson[136], E.J. Thorpe[93], V.O. Tikhomirov[111,af], Yu.A. Tikhonov[122b,122a], S. Timoshenko[112], P. Tipton[183], S. Tisserant[102], K. Todome[23b,23a], S. Todorova-Nova[142], S. Todt[48], J. Tojo[88], S. Tokár[28a], K. Tokushuku[82], E. Tolley[127], R. Tombs[32], K.G. Tomiwa[33f], M. Tomoto[82,117], L. Tompkins[153], P. Tornambe[103], E. Torrence[131], H. Torres[48], E. Torró Pastor[174], M. Toscani[30], C. Tosciri[134], J. Toth[102,y], D.R. Tovey[149], A. Traeet[17], C.J. Treado[125], T. Trefzger[177], F. Tresoldi[156], A. Tricoli[29], I.M. Trigger[168a], S. Trincaz-Duvoid[135], D.A. Trischuk[175], W. Trischuk[167], B. Trocmé[58], A. Trofymov[65], C. Troncon[69a], F. Trovato[156], L. Truong[33c], M. Trzebinski[85], A. Trzupek[85], F. Tsai[46], P.V. Tsiareshka[108,ad], A. Tsirigotis[162,u], V. Tsiskaridze[155], E.G. Tskhadadze[159a], M. Tsopoulou[162], I.I. Tsukerman[124], V. Tsulaia[18], S. Tsuno[82], D. Tsybychev[155], Y. Tu[63b], A. Tudorache[27b], V. Tudorache[27b], A.N. Tuna[36], S. Turchikhin[80], D. Turgeman[180], I. Turk Cakir[4b,s], R.J. Turner[21], R. Turra[69a], P.M. Tuts[39], S. Tzamarias[162], E. Tzovara[100], K. Uchida[163], F. Ukegawa[169], G. Unal[36], M. Unal[11], A. Undrus[29], G. Unel[171], F.C. Ungaro[105], Y. Unno[82], K. Uno[163], J. Urban[28b], P. Urquijo[105], G. Usai[8], Z. Uysal[12d], V. Vacek[141], B. Vachon[104], K.O.H. Vadla[133], T. Vafeiadis[36], A. Vaidya[95], C. Valderanis[114], E. Valdes Santurio[45a,45b], M. Valente[168a], S. Valentinetti[23b,23a], A. Valero[174], L. Valéry[46],

R.A. Vallance[21], A. Vallier[36], J.A. Valls Ferrer[174], T.R. Van Daalen[14], P. Van Gemmeren[6], S. Van Stroud[95], I. Van Vulpen[120], M. Vanadia[74a,74b], W. Vandelli[36], M. Vandenbroucke[144], E.R. Vandewall[129], D. Vannicola[73a,73b], R. Vari[73a], E.W. Varnes[7], C. Varni[55b,55a], T. Varol[158], D. Varouchas[65], K.E. Varvell[157], M.E. Vasile[27b], G.A. Vasquez[176], F. Vazeille[38], D. Vazquez Furelos[14], T. Vazquez Schroeder[36], J. Veatch[53], V. Vecchio[101], M.J. Veen[120], L.M. Veloce[167], F. Veloso[139a,139c], S. Veneziano[73a], A. Ventura[68a,68b], A. Verbytskyi[115], V. Vercesi[71a], M. Verducci[72a,72b], C.M. Vergel Infante[79], C. Vergis[24], W. Verkerke[120], A.T. Vermeulen[120], J.C. Vermeulen[120], C. Vernieri[153], P.J. Verschuuren[94], M.C. Vetterli[152,aj], N. Viaux Maira[146d], T. Vickey[149], O.E. Vickey Boeriu[149], G.H.A. Viehhauser[134], L. Vigani[61b], M. Villa[23b,23a], M. Villaplana Perez[174], E.M. Villhauer[50], E. Vilucchi[51], M.G. Vincter[34], G.S. Virdee[21], A. Vishwakarma[50], C. Vittori[23b,23a], I. Vivarelli[156], M. Vogel[182], P. Vokac[141], J. Von Ahnen[46], S.E. von Buddenbrock[33f], E. Von Toerne[24], V. Vorobel[142], K. Vorobev[112], M. Vos[174], J.H. Vossebeld[91], M. Vozak[101], N. Vranjes[16], M. Vranjes Milosavljevic[16], V. Vrba[141,*], M. Vreeswijk[120], N.K. Vu[102], R. Vuillermet[36], I. Vukotic[37], S. Wada[169], P. Wagner[24], W. Wagner[182], J. Wagner-Kuhr[114], S. Wahdan[182], H. Wahlberg[89], R. Wakasa[169], V.M. Walbrecht[115], J. Walder[143], R. Walker[114], S.D. Walker[94], W. Walkowiak[151], V. Wallangen[45a,45b], A.M. Wang[59], A.Z. Wang[181], C. Wang[60a], C. Wang[60c], H. Wang[18], H. Wang[3], J. Wang[63a], P. Wang[42], Q. Wang[128], R.-J. Wang[100], R. Wang[60a], R. Wang[6], S.M. Wang[158], W.T. Wang[60a], W. Wang[15c], W.X. Wang[60a], Y. Wang[60a], Z. Wang[106], C. Wanotayaroj[46], A. Warburton[104], C.P. Ward[32], R.J. Ward[21], N. Warrack[57], A.T. Watson[21], M.F. Watson[21], G. Watts[148], B.M. Waugh[95], A.F. Webb[11], C. Weber[29], M.S. Weber[20], S.A. Weber[34], S.M. Weber[61a], Y. Wei[134], A.R. Weidberg[134], J. Weingarten[47], M. Weirich[100], C. Weiser[52], P.S. Wells[36], T. Wenaus[29], B. Wendland[47], T. Wengler[36], S. Wenig[36], N. Wermes[24], M. Wessels[61a], T.D. Weston[20], K. Whalen[131], A.M. Wharton[90], A.S. White[106], A. White[8], M.J. White[1], D. Whiteson[171], B.W. Whitmore[90], W. Wiedenmann[181], C. Wiel[48], M. Wielers[143], N. Wieseotte[100], C. Wiglesworth[40], L.A.M. Wiik-Fuchs[52], H.G. Wilkens[36], L.J. Wilkins[94], D.M. Williams[39], H.H. Williams[136], S. Williams[32], S. Willocq[103], P.J. Windischhofer[134], I. Wingerter-Seez[5], E. Winkels[156], F. Winklmeier[131], B.T. Winter[52], M. Wittgen[153], M. Wobisch[96], A. Wolf[100], R. Wölker[134], J. Wollrath[52], M.W. Wolter[85], H. Wolters[139a,139c], V.W.S. Wong[175], A.F. Wongel[46], N.L. Woods[145], S.D. Worm[46], B.K. Wosiek[85], K.W. Woźniak[85], K. Wraight[57], S.L. Wu[181], X. Wu[54], Y. Wu[60a], J. Wuerzinger[134], T.R. Wyatt[101], B.M. Wynne[50], S. Xella[40], J. Xiang[63c], X. Xiao[106], X. Xie[60a], I. Xiotidis[156], D. Xu[15a], H. Xu[60a], H. Xu[60a], L. Xu[29], R. Xu[136], T. Xu[144], W. Xu[106], Y. Xu[15b], Z. Xu[60b], Z. Xu[153], B. Yabsley[157], S. Yacoob[33a], D.P. Yallup[95], N. Yamaguchi[88], Y. Yamaguchi[165], A. Yamamoto[82], M. Yamatani[163], T. Yamazaki[163], Y. Yamazaki[83], J. Yan[60c], Z. Yan[25], H.J. Yang[60c,60d], H.T. Yang[18], S. Yang[60a], T. Yang[63c], X. Yang[60a], X. Yang[60b,58], Y. Yang[163], Z. Yang[106,60a], W-M. Yao[18], Y.C. Yap[46], H. Ye[15c], J. Ye[42], S. Ye[29], I. Yeletskikh[80], M.R. Yexley[90], E. Yigitbasi[25], P. Yin[39], K. Yorita[179], K. Yoshihara[79], C.J.S. Young[36], C. Young[153], J. Yu[79], R. Yuan[60b,h], X. Yue[61a], M. Zaazoua[35f], B. Zabinski[85], G. Zacharis[10], E. Zaffaroni[54], J. Zahreddine[135], A.M. Zaitsev[123,ae], T. Zakareishvili[159b], N. Zakharchuk[34], S. Zambito[36], D. Zanzi[36], S.V. Zeißner[47], C. Zeitnitz[182], G. Zemaityte[134], J.C. Zeng[173], O. Zenin[123], T. Ženiš[28a], D. Zerwas[65], M. Zgubič[134], B. Zhang[15c], D.F. Zhang[15b], G. Zhang[15b], J. Zhang[6], K. Zhang[15a], L. Zhang[15c], L. Zhang[60a], M. Zhang[173], R. Zhang[181], S. Zhang[106], X. Zhang[60c], X. Zhang[60b], Y. Zhang[15a,15d], Z. Zhang[63a], Z. Zhang[65], P. Zhao[49], Y. Zhao[145], Z. Zhao[60a], A. Zhemchugov[80], Z. Zheng[106], D. Zhong[173], B. Zhou[106], C. Zhou[181], H. Zhou[7], M. Zhou[155], N. Zhou[60c], Y. Zhou[7], C.G. Zhu[60b], C. Zhu[15a,15d], H.L. Zhu[60a], H. Zhu[15a], J. Zhu[106], Y. Zhu[60a], X. Zhuang[15a], K. Zhukov[111], V. Zhulanov[122b,122a], D. Zieminska[66], N.I. Zimine[80], S. Zimmermann[52,*], Z. Zinonos[115], M. Ziolkowski[151], L. Živković[16], G. Zobernig[181], A. Zoccoli[23b,23a], K. Zoch[53], T.G. Zorbas[149], R. Zou[37], L. Zwalinski[36].

[1]Department of Physics, University of Adelaide, Adelaide; Australia.
[2]Physics Department, SUNY Albany, Albany NY; United States of America.
[3]Department of Physics, University of Alberta, Edmonton AB; Canada.

[4(a)]Department of Physics, Ankara University, Ankara;[(b)]Istanbul Aydin University, Application and Research Center for Advanced Studies, Istanbul;[(c)]Division of Physics, TOBB University of Economics and Technology, Ankara; Turkey.
[5]LAPP, Univ. Savoie Mont Blanc, CNRS/IN2P3, Annecy ; France.
[6]High Energy Physics Division, Argonne National Laboratory, Argonne IL; United States of America.
[7]Department of Physics, University of Arizona, Tucson AZ; United States of America.
[8]Department of Physics, University of Texas at Arlington, Arlington TX; United States of America.
[9]Physics Department, National and Kapodistrian University of Athens, Athens; Greece.
[10]Physics Department, National Technical University of Athens, Zografou; Greece.
[11]Department of Physics, University of Texas at Austin, Austin TX; United States of America.
[12(a)]Bahcesehir University, Faculty of Engineering and Natural Sciences, Istanbul;[(b)]Istanbul Bilgi University, Faculty of Engineering and Natural Sciences, Istanbul;[(c)]Department of Physics, Bogazici University, Istanbul;[(d)]Department of Physics Engineering, Gaziantep University, Gaziantep; Turkey.
[13]Institute of Physics, Azerbaijan Academy of Sciences, Baku; Azerbaijan.
[14]Institut de Física d'Altes Energies (IFAE), Barcelona Institute of Science and Technology, Barcelona; Spain.
[15(a)]Institute of High Energy Physics, Chinese Academy of Sciences, Beijing;[(b)]Physics Department, Tsinghua University, Beijing;[(c)]Department of Physics, Nanjing University, Nanjing;[(d)]University of Chinese Academy of Science (UCAS), Beijing; China.
[16]Institute of Physics, University of Belgrade, Belgrade; Serbia.
[17]Department for Physics and Technology, University of Bergen, Bergen; Norway.
[18]Physics Division, Lawrence Berkeley National Laboratory and University of California, Berkeley CA; United States of America.
[19]Institut für Physik, Humboldt Universität zu Berlin, Berlin; Germany.
[20]Albert Einstein Center for Fundamental Physics and Laboratory for High Energy Physics, University of Bern, Bern; Switzerland.
[21]School of Physics and Astronomy, University of Birmingham, Birmingham; United Kingdom.
[22(a)]Facultad de Ciencias y Centro de Investigaciónes, Universidad Antonio Nariño, Bogotá;[(b)]Departamento de Física, Universidad Nacional de Colombia, Bogotá, Colombia; Colombia.
[23(a)]INFN Bologna and Universita' di Bologna, Dipartimento di Fisica;[(b)]INFN Sezione di Bologna; Italy.
[24]Physikalisches Institut, Universität Bonn, Bonn; Germany.
[25]Department of Physics, Boston University, Boston MA; United States of America.
[26]Department of Physics, Brandeis University, Waltham MA; United States of America.
[27(a)]Transilvania University of Brasov, Brasov;[(b)]Horia Hulubei National Institute of Physics and Nuclear Engineering, Bucharest;[(c)]Department of Physics, Alexandru Ioan Cuza University of Iasi, Iasi;[(d)]National Institute for Research and Development of Isotopic and Molecular Technologies, Physics Department, Cluj-Napoca;[(e)]University Politehnica Bucharest, Bucharest;[(f)]West University in Timisoara, Timisoara; Romania.
[28(a)]Faculty of Mathematics, Physics and Informatics, Comenius University, Bratislava;[(b)]Department of Subnuclear Physics, Institute of Experimental Physics of the Slovak Academy of Sciences, Kosice; Slovak Republic.
[29]Physics Department, Brookhaven National Laboratory, Upton NY; United States of America.
[30]Departamento de Física, Universidad de Buenos Aires, Buenos Aires; Argentina.
[31]California State University, CA; United States of America.
[32]Cavendish Laboratory, University of Cambridge, Cambridge; United Kingdom.
[33(a)]Department of Physics, University of Cape Town, Cape Town;[(b)]iThemba Labs, Western Cape;[(c)]Department of Mechanical Engineering Science, University of Johannesburg,

Johannesburg;[d]National Institute of Physics, University of the Philippines Diliman;[e]University of South Africa, Department of Physics, Pretoria;[f]School of Physics, University of the Witwatersrand, Johannesburg; South Africa.
[34]Department of Physics, Carleton University, Ottawa ON; Canada.
[35(a)]Faculté des Sciences Ain Chock, Réseau Universitaire de Physique des Hautes Energies - Université Hassan II, Casablanca;[b]Faculté des Sciences, Université Ibn-Tofail, Kénitra;[c]Faculté des Sciences Semlalia, Université Cadi Ayyad, LPHEA-Marrakech;[d]Moroccan Foundation for Advanced Science Innovation and Research (MAScIR), Rabat;[e]LPMR, Faculté des Sciences, Université Mohamed Premier, Oujda;[f]Faculté des sciences, Université Mohammed V, Rabat; Morocco.
[36]CERN, Geneva; Switzerland.
[37]Enrico Fermi Institute, University of Chicago, Chicago IL; United States of America.
[38]LPC, Université Clermont Auvergne, CNRS/IN2P3, Clermont-Ferrand; France.
[39]Nevis Laboratory, Columbia University, Irvington NY; United States of America.
[40]Niels Bohr Institute, University of Copenhagen, Copenhagen; Denmark.
[41(a)]Dipartimento di Fisica, Università della Calabria, Rende;[b]INFN Gruppo Collegato di Cosenza, Laboratori Nazionali di Frascati; Italy.
[42]Physics Department, Southern Methodist University, Dallas TX; United States of America.
[43]Physics Department, University of Texas at Dallas, Richardson TX; United States of America.
[44]National Centre for Scientific Research "Demokritos", Agia Paraskevi; Greece.
[45(a)]Department of Physics, Stockholm University;[b]Oskar Klein Centre, Stockholm; Sweden.
[46]Deutsches Elektronen-Synchrotron DESY, Hamburg and Zeuthen; Germany.
[47]Lehrstuhl für Experimentelle Physik IV, Technische Universität Dortmund, Dortmund; Germany.
[48]Institut für Kern- und Teilchenphysik, Technische Universität Dresden, Dresden; Germany.
[49]Department of Physics, Duke University, Durham NC; United States of America.
[50]SUPA - School of Physics and Astronomy, University of Edinburgh, Edinburgh; United Kingdom.
[51]INFN e Laboratori Nazionali di Frascati, Frascati; Italy.
[52]Physikalisches Institut, Albert-Ludwigs-Universität Freiburg, Freiburg; Germany.
[53]II. Physikalisches Institut, Georg-August-Universität Göttingen, Göttingen; Germany.
[54]Département de Physique Nucléaire et Corpusculaire, Université de Genève, Genève; Switzerland.
[55(a)]Dipartimento di Fisica, Università di Genova, Genova;[b]INFN Sezione di Genova; Italy.
[56]II. Physikalisches Institut, Justus-Liebig-Universität Giessen, Giessen; Germany.
[57]SUPA - School of Physics and Astronomy, University of Glasgow, Glasgow; United Kingdom.
[58]LPSC, Université Grenoble Alpes, CNRS/IN2P3, Grenoble INP, Grenoble; France.
[59]Laboratory for Particle Physics and Cosmology, Harvard University, Cambridge MA; United States of America.
[60(a)]Department of Modern Physics and State Key Laboratory of Particle Detection and Electronics, University of Science and Technology of China, Hefei;[b]Institute of Frontier and Interdisciplinary Science and Key Laboratory of Particle Physics and Particle Irradiation (MOE), Shandong University, Qingdao;[c]School of Physics and Astronomy, Shanghai Jiao Tong University, Key Laboratory for Particle Astrophysics and Cosmology (MOE), SKLPPC, Shanghai;[d]Tsung-Dao Lee Institute, Shanghai; China.
[61(a)]Kirchhoff-Institut für Physik, Ruprecht-Karls-Universität Heidelberg, Heidelberg;[b]Physikalisches Institut, Ruprecht-Karls-Universität Heidelberg, Heidelberg; Germany.
[62]Faculty of Applied Information Science, Hiroshima Institute of Technology, Hiroshima; Japan.
[63(a)]Department of Physics, Chinese University of Hong Kong, Shatin, N.T., Hong Kong;[b]Department of Physics, University of Hong Kong, Hong Kong;[c]Department of Physics and Institute for Advanced Study, Hong Kong University of Science and Technology, Clear Water Bay, Kowloon, Hong Kong; China.
[64]Department of Physics, National Tsing Hua University, Hsinchu; Taiwan.

[65]IJCLab, Université Paris-Saclay, CNRS/IN2P3, 91405, Orsay; France.
[66]Department of Physics, Indiana University, Bloomington IN; United States of America.
[67(a)]INFN Gruppo Collegato di Udine, Sezione di Trieste, Udine;[(b)]ICTP, Trieste;[(c)]Dipartimento Politecnico di Ingegneria e Architettura, Università di Udine, Udine; Italy.
[68(a)]INFN Sezione di Lecce;[(b)]Dipartimento di Matematica e Fisica, Università del Salento, Lecce; Italy.
[69(a)]INFN Sezione di Milano;[(b)]Dipartimento di Fisica, Università di Milano, Milano; Italy.
[70(a)]INFN Sezione di Napoli;[(b)]Dipartimento di Fisica, Università di Napoli, Napoli; Italy.
[71(a)]INFN Sezione di Pavia;[(b)]Dipartimento di Fisica, Università di Pavia, Pavia; Italy.
[72(a)]INFN Sezione di Pisa;[(b)]Dipartimento di Fisica E. Fermi, Università di Pisa, Pisa; Italy.
[73(a)]INFN Sezione di Roma;[(b)]Dipartimento di Fisica, Sapienza Università di Roma, Roma; Italy.
[74(a)]INFN Sezione di Roma Tor Vergata;[(b)]Dipartimento di Fisica, Università di Roma Tor Vergata, Roma; Italy.
[75(a)]INFN Sezione di Roma Tre;[(b)]Dipartimento di Matematica e Fisica, Università Roma Tre, Roma; Italy.
[76(a)]INFN-TIFPA;[(b)]Università degli Studi di Trento, Trento; Italy.
[77]Institut für Astro- und Teilchenphysik, Leopold-Franzens-Universität, Innsbruck; Austria.
[78]University of Iowa, Iowa City IA; United States of America.
[79]Department of Physics and Astronomy, Iowa State University, Ames IA; United States of America.
[80]Joint Institute for Nuclear Research, Dubna; Russia.
[81(a)]Departamento de Engenharia Elétrica, Universidade Federal de Juiz de Fora (UFJF), Juiz de Fora;[(b)]Universidade Federal do Rio De Janeiro COPPE/EE/IF, Rio de Janeiro;[(c)]Instituto de Física, Universidade de São Paulo, São Paulo; Brazil.
[82]KEK, High Energy Accelerator Research Organization, Tsukuba; Japan.
[83]Graduate School of Science, Kobe University, Kobe; Japan.
[84(a)]AGH University of Science and Technology, Faculty of Physics and Applied Computer Science, Krakow;[(b)]Marian Smoluchowski Institute of Physics, Jagiellonian University, Krakow; Poland.
[85]Institute of Nuclear Physics Polish Academy of Sciences, Krakow; Poland.
[86]Faculty of Science, Kyoto University, Kyoto; Japan.
[87]Kyoto University of Education, Kyoto; Japan.
[88]Research Center for Advanced Particle Physics and Department of Physics, Kyushu University, Fukuoka ; Japan.
[89]Instituto de Física La Plata, Universidad Nacional de La Plata and CONICET, La Plata; Argentina.
[90]Physics Department, Lancaster University, Lancaster; United Kingdom.
[91]Oliver Lodge Laboratory, University of Liverpool, Liverpool; United Kingdom.
[92]Department of Experimental Particle Physics, Jožef Stefan Institute and Department of Physics, University of Ljubljana, Ljubljana; Slovenia.
[93]School of Physics and Astronomy, Queen Mary University of London, London; United Kingdom.
[94]Department of Physics, Royal Holloway University of London, Egham; United Kingdom.
[95]Department of Physics and Astronomy, University College London, London; United Kingdom.
[96]Louisiana Tech University, Ruston LA; United States of America.
[97]Fysiska institutionen, Lunds universitet, Lund; Sweden.
[98]Centre de Calcul de l'Institut National de Physique Nucléaire et de Physique des Particules (IN2P3), Villeurbanne; France.
[99]Departamento de Física Teorica C-15 and CIAFF, Universidad Autónoma de Madrid, Madrid; Spain.
[100]Institut für Physik, Universität Mainz, Mainz; Germany.
[101]School of Physics and Astronomy, University of Manchester, Manchester; United Kingdom.
[102]CPPM, Aix-Marseille Université, CNRS/IN2P3, Marseille; France.

[103]Department of Physics, University of Massachusetts, Amherst MA; United States of America.
[104]Department of Physics, McGill University, Montreal QC; Canada.
[105]School of Physics, University of Melbourne, Victoria; Australia.
[106]Department of Physics, University of Michigan, Ann Arbor MI; United States of America.
[107]Department of Physics and Astronomy, Michigan State University, East Lansing MI; United States of America.
[108]B.I. Stepanov Institute of Physics, National Academy of Sciences of Belarus, Minsk; Belarus.
[109]Research Institute for Nuclear Problems of Byelorussian State University, Minsk; Belarus.
[110]Group of Particle Physics, University of Montreal, Montreal QC; Canada.
[111]P.N. Lebedev Physical Institute of the Russian Academy of Sciences, Moscow; Russia.
[112]National Research Nuclear University MEPhI, Moscow; Russia.
[113]D.V. Skobeltsyn Institute of Nuclear Physics, M.V. Lomonosov Moscow State University, Moscow; Russia.
[114]Fakultät für Physik, Ludwig-Maximilians-Universität München, München; Germany.
[115]Max-Planck-Institut für Physik (Werner-Heisenberg-Institut), München; Germany.
[116]Nagasaki Institute of Applied Science, Nagasaki; Japan.
[117]Graduate School of Science and Kobayashi-Maskawa Institute, Nagoya University, Nagoya; Japan.
[118]Department of Physics and Astronomy, University of New Mexico, Albuquerque NM; United States of America.
[119]Institute for Mathematics, Astrophysics and Particle Physics, Radboud University/Nikhef, Nijmegen; Netherlands.
[120]Nikhef National Institute for Subatomic Physics and University of Amsterdam, Amsterdam; Netherlands.
[121]Department of Physics, Northern Illinois University, DeKalb IL; United States of America.
[122(a)]Budker Institute of Nuclear Physics and NSU, SB RAS, Novosibirsk;[(b)]Novosibirsk State University Novosibirsk; Russia.
[123]Institute for High Energy Physics of the National Research Centre Kurchatov Institute, Protvino; Russia.
[124]Institute for Theoretical and Experimental Physics named by A.I. Alikhanov of National Research Centre "Kurchatov Institute", Moscow; Russia.
[125]Department of Physics, New York University, New York NY; United States of America.
[126]Ochanomizu University, Otsuka, Bunkyo-ku, Tokyo; Japan.
[127]Ohio State University, Columbus OH; United States of America.
[128]Homer L. Dodge Department of Physics and Astronomy, University of Oklahoma, Norman OK; United States of America.
[129]Department of Physics, Oklahoma State University, Stillwater OK; United States of America.
[130]Palacký University, Joint Laboratory of Optics, Olomouc; Czech Republic.
[131]Institute for Fundamental Science, University of Oregon, Eugene, OR; United States of America.
[132]Graduate School of Science, Osaka University, Osaka; Japan.
[133]Department of Physics, University of Oslo, Oslo; Norway.
[134]Department of Physics, Oxford University, Oxford; United Kingdom.
[135]LPNHE, Sorbonne Université, Université de Paris, CNRS/IN2P3, Paris; France.
[136]Department of Physics, University of Pennsylvania, Philadelphia PA; United States of America.
[137]Konstantinov Nuclear Physics Institute of National Research Centre "Kurchatov Institute", PNPI, St. Petersburg; Russia.
[138]Department of Physics and Astronomy, University of Pittsburgh, Pittsburgh PA; United States of America.
[139(a)]Laboratório de Instrumentação e Física Experimental de Partículas - LIP, Lisboa;[(b)]Departamento de

Física, Faculdade de Ciências, Universidade de Lisboa, Lisboa;[(c)]Departamento de Física, Universidade de Coimbra, Coimbra;[(d)]Centro de Física Nuclear da Universidade de Lisboa, Lisboa;[(e)]Departamento de Física, Universidade do Minho, Braga;[(f)]Departamento de Física Teórica y del Cosmos, Universidad de Granada, Granada (Spain);[(g)]Dep Física and CEFITEC of Faculdade de Ciências e Tecnologia, Universidade Nova de Lisboa, Caparica;[(h)]Instituto Superior Técnico, Universidade de Lisboa, Lisboa; Portugal.
[140]Institute of Physics of the Czech Academy of Sciences, Prague; Czech Republic.
[141]Czech Technical University in Prague, Prague; Czech Republic.
[142]Charles University, Faculty of Mathematics and Physics, Prague; Czech Republic.
[143]Particle Physics Department, Rutherford Appleton Laboratory, Didcot; United Kingdom.
[144]IRFU, CEA, Université Paris-Saclay, Gif-sur-Yvette; France.
[145]Santa Cruz Institute for Particle Physics, University of California Santa Cruz, Santa Cruz CA; United States of America.
[146(a)]Departamento de Física, Pontificia Universidad Católica de Chile, Santiago;[(b)]Universidad Andres Bello, Department of Physics, Santiago;[(c)]Instituto de Alta Investigación, Universidad de Tarapacá, Arica;[(d)]Departamento de Física, Universidad Técnica Federico Santa María, Valparaíso; Chile.
[147]Universidade Federal de São João del Rei (UFSJ), São João del Rei; Brazil.
[148]Department of Physics, University of Washington, Seattle WA; United States of America.
[149]Department of Physics and Astronomy, University of Sheffield, Sheffield; United Kingdom.
[150]Department of Physics, Shinshu University, Nagano; Japan.
[151]Department Physik, Universität Siegen, Siegen; Germany.
[152]Department of Physics, Simon Fraser University, Burnaby BC; Canada.
[153]SLAC National Accelerator Laboratory, Stanford CA; United States of America.
[154]Physics Department, Royal Institute of Technology, Stockholm; Sweden.
[155]Departments of Physics and Astronomy, Stony Brook University, Stony Brook NY; United States of America.
[156]Department of Physics and Astronomy, University of Sussex, Brighton; United Kingdom.
[157]School of Physics, University of Sydney, Sydney; Australia.
[158]Institute of Physics, Academia Sinica, Taipei; Taiwan.
[159(a)]E. Andronikashvili Institute of Physics, Iv. Javakhishvili Tbilisi State University, Tbilisi;[(b)]High Energy Physics Institute, Tbilisi State University, Tbilisi; Georgia.
[160]Department of Physics, Technion, Israel Institute of Technology, Haifa; Israel.
[161]Raymond and Beverly Sackler School of Physics and Astronomy, Tel Aviv University, Tel Aviv; Israel.
[162]Department of Physics, Aristotle University of Thessaloniki, Thessaloniki; Greece.
[163]International Center for Elementary Particle Physics and Department of Physics, University of Tokyo, Tokyo; Japan.
[164]Graduate School of Science and Technology, Tokyo Metropolitan University, Tokyo; Japan.
[165]Department of Physics, Tokyo Institute of Technology, Tokyo; Japan.
[166]Tomsk State University, Tomsk; Russia.
[167]Department of Physics, University of Toronto, Toronto ON; Canada.
[168(a)]TRIUMF, Vancouver BC;[(b)]Department of Physics and Astronomy, York University, Toronto ON; Canada.
[169]Division of Physics and Tomonaga Center for the History of the Universe, Faculty of Pure and Applied Sciences, University of Tsukuba, Tsukuba; Japan.
[170]Department of Physics and Astronomy, Tufts University, Medford MA; United States of America.
[171]Department of Physics and Astronomy, University of California Irvine, Irvine CA; United States of America.

[172]Department of Physics and Astronomy, University of Uppsala, Uppsala; Sweden.
[173]Department of Physics, University of Illinois, Urbana IL; United States of America.
[174]Instituto de Física Corpuscular (IFIC), Centro Mixto Universidad de Valencia - CSIC, Valencia; Spain.
[175]Department of Physics, University of British Columbia, Vancouver BC; Canada.
[176]Department of Physics and Astronomy, University of Victoria, Victoria BC; Canada.
[177]Fakultät für Physik und Astronomie, Julius-Maximilians-Universität Würzburg, Würzburg; Germany.
[178]Department of Physics, University of Warwick, Coventry; United Kingdom.
[179]Waseda University, Tokyo; Japan.
[180]Department of Particle Physics and Astrophysics, Weizmann Institute of Science, Rehovot; Israel.
[181]Department of Physics, University of Wisconsin, Madison WI; United States of America.
[182]Fakultät für Mathematik und Naturwissenschaften, Fachgruppe Physik, Bergische Universität Wuppertal, Wuppertal; Germany.
[183]Department of Physics, Yale University, New Haven CT; United States of America.
[a] Also at Borough of Manhattan Community College, City University of New York, New York NY; United States of America.
[b] Also at Centro Studi e Ricerche Enrico Fermi; Italy.
[c] Also at CERN, Geneva; Switzerland.
[d] Also at CPPM, Aix-Marseille Université, CNRS/IN2P3, Marseille; France.
[e] Also at Département de Physique Nucléaire et Corpusculaire, Université de Genève, Genève; Switzerland.
[f] Also at Departament de Fisica de la Universitat Autonoma de Barcelona, Barcelona; Spain.
[g] Also at Department of Financial and Management Engineering, University of the Aegean, Chios; Greece.
[h] Also at Department of Physics and Astronomy, Michigan State University, East Lansing MI; United States of America.
[i] Also at Department of Physics and Astronomy, University of Louisville, Louisville, KY; United States of America.
[j] Also at Department of Physics, Ben Gurion University of the Negev, Beer Sheva; Israel.
[k] Also at Department of Physics, California State University, East Bay; United States of America.
[l] Also at Department of Physics, California State University, Fresno; United States of America.
[m] Also at Department of Physics, California State University, Sacramento; United States of America.
[n] Also at Department of Physics, King's College London, London; United Kingdom.
[o] Also at Department of Physics, St. Petersburg State Polytechnical University, St. Petersburg; Russia.
[p] Also at Department of Physics, University of Fribourg, Fribourg; Switzerland.
[q] Also at Dipartimento di Matematica, Informatica e Fisica, Università di Udine, Udine; Italy.
[r] Also at Faculty of Physics, M.V. Lomonosov Moscow State University, Moscow; Russia.
[s] Also at Giresun University, Faculty of Engineering, Giresun; Turkey.
[t] Also at Graduate School of Science, Osaka University, Osaka; Japan.
[u] Also at Hellenic Open University, Patras; Greece.
[v] Also at Institucio Catalana de Recerca i Estudis Avancats, ICREA, Barcelona; Spain.
[w] Also at Institut für Experimentalphysik, Universität Hamburg, Hamburg; Germany.
[x] Also at Institute for Nuclear Research and Nuclear Energy (INRNE) of the Bulgarian Academy of Sciences, Sofia; Bulgaria.
[y] Also at Institute for Particle and Nuclear Physics, Wigner Research Centre for Physics, Budapest; Hungary.
[z] Also at Institute of Particle Physics (IPP); Canada.
[aa] Also at Institute of Physics, Azerbaijan Academy of Sciences, Baku; Azerbaijan.
[ab] Also at Instituto de Fisica Teorica, IFT-UAM/CSIC, Madrid; Spain.

[ac] Also at Istanbul University, Dept. of Physics, Istanbul; Turkey.
[ad] Also at Joint Institute for Nuclear Research, Dubna; Russia.
[ae] Also at Moscow Institute of Physics and Technology State University, Dolgoprudny; Russia.
[af] Also at National Research Nuclear University MEPhI, Moscow; Russia.
[ag] Also at Physics Department, An-Najah National University, Nablus; Palestine.
[ah] Also at Physikalisches Institut, Albert-Ludwigs-Universität Freiburg, Freiburg; Germany.
[ai] Also at The City College of New York, New York NY; United States of America.
[aj] Also at TRIUMF, Vancouver BC; Canada.
[ak] Also at Universita di Napoli Parthenope, Napoli; Italy.
[al] Also at University of Chinese Academy of Sciences (UCAS), Beijing; China.
[*] Deceased